Thesis

Quantum Fluctuations and Magnetic Structures of Hexagonal Antiferromagnet: $CsCuCl_3$ in Magnetic Fields

Tetsuro Nikuni

Department of Physics
Tokyo Institute of Technology

December 1995

Acknowledgements

The author would like to express his sincere gratitude to Professor Hiroyuki Shiba for encouraging suggestions and stimulating discussions throughout the course of the present work and also for his careful reading of the manuscript.

The author would like to thank Professor Mitsuhiro Motokawa and Dr. Michinobu Mino for valuable discussions.

The author is grateful to Professor Allan E. Jacobs for stimulating discussions and collaboration on the incommensurate state of $CsCuCl_3$ and also for reading the manuscript.

Abstract

This thesis studies theoretically the effect of quantum fluctuations on a hexagonal antiferromagnet in magnetic field, with application to the material $CsCuCl_3$ and the unexpected behaviors found experimentally in the magnetization process of $CsCuCl_3$. The purpose of the thesis is to show that quantum fluctuations play an important role in determining the ground-state spin structures of $CsCuCl_3$. The effect of quantum fluctuations is investigated by applying various approaches.

First, a theoretical interpretation of the small jump in the magnetization of $CsCuCl_3$, observed for a magnetic field applied parallel to the c-axis, is presented. Quantum fluctuations are taken into account by using spin-wave theory. We propose that a new spin structure is stabilized by quantum fluctuations in the high-field region. The observed magnetization jump is successfully explained as a spin-flop phase transition caused by quantum effects. Our proposal is supported by several experimental results.

Second, the ground-state magnetic structure near the saturation field is investigated by using the exact hard-core-boson representation of $S = 1/2$ spins. The spin-ordering problem near saturation is transformed to an equivalent two-component Bose condensation problem in the low-density limit; then the low-density expansion is applied to determine the ground state. From this study, we explicitly show that the ground-state spin structure of $CsCuCl_3$ near the saturation field is different from the one predicted by the classical theory. This conclusion agrees with that of the $1/S$ expansion.

Finally, we investigate the magnetic structure of $CsCuCl_3$ in a transverse magnetic field. First the classical theory is applied to determine the ground state spin structure. At zero field, $CsCuCl_3$ is known to form a helical spin structure along the c-axis. A transverse field deforms the helical structure and causes a continuous phase transition from the helical (i.e. incommensurate) spin structure to a commensurate state. The classical incommensurate state has several unusual features originating from the classical nontrivial degeneracy; these features should be removed by quan-

tum fluctuations. Therefore the effect of quantum fluctuations is taken into account in a phenomenological manner. We see a large modification in the incommensurate spin structure, which can be attributed to quantum fluctuations.

Contents

Chapter 1

Introduction

The effects of quantum fluctuations on antiferromagnetic spin systems have attracted attention recently. Attention has been paid especially to low-dimensional quantum spin systems where quantum fluctuations are strong enough either to destroy the magnetic ordering or give rise to new phases in the ground state. As a well-known example, one-dimensional Heisenberg antiferromagnets have no long-range order even at zero temperature, because of the strong quantum fluctuations. Thus many researchers are investigating low-dimensional quantum spin systems to find new phases or ground-state phase transitions.

There is, however, a different class of systems which are of importance and interest from the viewpoint of quantum fluctuations. For most magnetic substances the classical (mean-field) theory is a reliable method to determine the ground-state spin structure in the magnetically ordered phase. That is, once magnetic ordering is achieved and a macroscopic magnetic moment appears, the magnetic properties of the system are well understood in terms of the "classical spin" picture. In the classical (mean-field) theory, the spin Hamiltonian is regarded as an energy function of the magnetic moments (or classical spin vectors). The ground-state magnetic structure is determined so as to minimize the classical energy. This approach has succeeded in explaining many experimental results on ionic magnetic materials. It has been therefore believed that quantum fluctuations do not change the nature of the ground state in an essential manner, although they correct the physical quantities to some extent. There are, however, some exceptions to this rule. Namely, in some frustrated spin systems the classical theory predicts infinitely degenerate ground states; the degeneracy is unrelated to the symmetry of the original Hamiltonian (i.e. the degeneracy is nontrivial). In such cases, fluctuations (omitted from

the mean-field approximation) are crucial in determining the most stable state. So far several theoretical models have been suggested to fall into this category [1-9]; the two-dimensional triangular antiferromagnet in a magnetic field [1-3], the fcc antiferromagnet [4], a frustrated square antiferromagnet [5,6], and a triangular antiferromagnet with easy-axis anisotropy [7-9] are examples. In all cases, the classical ground state has a nontrivial continuous degeneracy; that is, the ground state cannot be determined uniquely. Quantum and/or thermal fluctuations remove the degeneracy and select the most stable state. The empirical finding is that quantum and thermal fluctuations select the same spin structure as the stable state. These effects are due to fluctuations, and thus are sometimes called "order from disorder" phenomena. These phenomena have been mostly only of theoretical interest because in most systems the mean-field theory determines the unique ground state. The purpose of this thesis is to study such problems theoretically in connection with a real material. We argue that the hexagonal antiferromagnet $CsCuCl_3$ is a good example to see the physics of quantum fluctuations and the nontrivial degeneracy.

$CsCuCl_3$ is one of the hexagonal ABX_3-type antiferromagnets whose magnetic properties have been investigated extensively. In 1978 Motokawa discovered an anomaly in the magnetization curve of $CsCuCl_3$ [10,11]; the magnetization has a small jump for a magnetic field applied parallel to the c-axis. The classical theory is not a reasonable model for this problem, for it cannot explain the anomaly in the magnetization. Therefore the observed phase transition at H_c has been a mystery for a long time.

Stimulated by Motokawa's discovery of the magnetization anomaly in $CsCuCl_3$, we study theoretically the effects of quantum fluctuations on hexagonal antiferromagnets in magnetic fields. Having $CsCuCl_3$ in mind, we study several realistic situations and see how quantum fluctuations change the ground-state spin structure from the classical state. From this study we show that the unexpected behavior of the magnetization of $CsCuCl_3$ can be understood as a manifestation of the effect of quantum fluctuations on the triangular antiferromagnet in magnetic fields.

In the following sections, we review theoretical and experimental backgrounds for the present study.

1.1 Triangular Antiferromagnet in an External Magnetic Field

There has been considerable interests in the phase transition and low-temperature properties of the triangular antiferromagnet, since it is a typical model with the frustration. Many interesting properties in the ordering process have been found already, which can be attributed to the frustration. In the quantum model, the possibility of a disordered ground state in the $S = 1/2$ system, due to strong zero-point quantum fluctuations, has been an important topic of theoretical study. Apart from these interests, the triangular antiferromagnet shows unique features when an external magnetic field is applied to the system. This section reviews the theoretical developments on the triangular antiferromagnet in an external field.

1.1.1 Classical Theory

The triangular antiferromagnet in an external field is described by the following Hamiltonian:

$$\mathcal{H} = 2J \sum_{\langle ij \rangle} \boldsymbol{S}_i \cdot \boldsymbol{S}_j - \sum_i \boldsymbol{H} \cdot \boldsymbol{S}_i, \tag{1.1}$$

where $J > 0$ is the antiferromagnetic exchange interaction between nearest-neighbor spin pairs; the summation $\langle ij \rangle$ is taken over for all nearest pairs. In the classical theory, the spin $\boldsymbol{S}_i$ is regarded as a classical vector with $|\boldsymbol{S}_i| \equiv S$ and the Hamiltonian $\mathcal{H}$ is regarded as an energy function of the $\boldsymbol{S}_i$. In the classical ground state, spins are divided into 3 sublattices. The ground-state energy can be written in terms of the sublattice moments $\boldsymbol{S}_1, \boldsymbol{S}_2$, and $\boldsymbol{S}_3$ as

$$\frac{E}{N} = 2J(\boldsymbol{S}_1 \cdot \boldsymbol{S}_2 + \boldsymbol{S}_2 \cdot \boldsymbol{S}_3 + \boldsymbol{S}_3 \cdot \boldsymbol{S}_1) - \frac{1}{3}\boldsymbol{H} \cdot (\boldsymbol{S}_1 + \boldsymbol{S}_2 + \boldsymbol{S}_3), \tag{1.2}$$

where N denotes the number of spins. For $H = 0$, the ground state has the well-known 120° structure. It has a trivial continuous degeneracy related to the spherical symmetry of the system and a two-fold discrete degeneracy associated with the choice of sublattices. The external field reduces the symmetry of the Hamiltonian from the spherical symmetry to the rotational symmetry around the magnetic field. However, the ground state of the Hamiltonian (1.1) still has a continuous degeneracy as shown below. The energy expression (1.2) is simplified by using the relation $(\boldsymbol{S}_1 + \boldsymbol{S}_2 +$

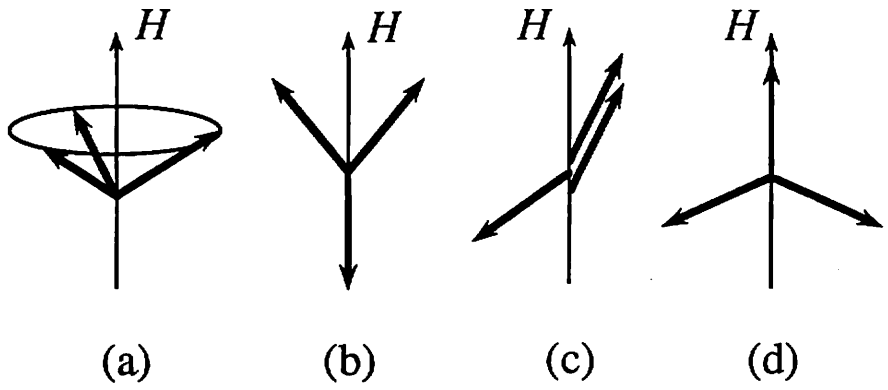

Figure 1.1: Examples of the classical ground state of triangular antiferromagnet in a magnetic field: (a) umbrella-type structure. (b) low-field coplanar structure. (c) high-field coplanar structure. (d) coplanar structure which is the inverse of (b).

$\boldsymbol{S}_3)^2 = 3S^2 + 2(\boldsymbol{S}_1 \cdot \boldsymbol{S}_2 + \boldsymbol{S}_2 \cdot \boldsymbol{S}_3 + \boldsymbol{S}_3 \cdot \boldsymbol{S}_1)$ as

$$\frac{E}{N} = -3JS^2 - \frac{H^2}{36J} + J\left(\boldsymbol{S}_1 + \boldsymbol{S}_2 + \boldsymbol{S}_3 - \frac{\boldsymbol{H}}{6J}\right)^2. \tag{1.3}$$

The minimum of the energy expression (1.3) is clearly obtained by imposing the condition

$$\boldsymbol{S}_1 + \boldsymbol{S}_2 + \boldsymbol{S}_3 = \frac{\boldsymbol{H}}{6J}. \tag{1.4}$$

To determine the directions of $\boldsymbol{S}_1, \boldsymbol{S}_2$ and $\boldsymbol{S}_3$ we need $2 \times 3 = 6$ parameters, but Eq. (1.4) gives only three conditions. Therefore the spin configuration cannot be determined uniquely by the condition (1.4), even if we ignore the degree of freedom with respect to the rotation around the field direction. This type of degeneracy is continuous and does not reflect the symmetry of the original Hamiltonian; thus it is often called a nontrivial continuous degeneracy [2]. Figure 1.1 shows four representative examples of ground-state spin configurations. In addition to these four states, there is an infinite number of spin configurations with the same ground-state energy.

Suppose the system has an easy-plane anisotropy, and that an external field is applied in the plane:

$$\mathcal{H} = 2J \sum_{<ij>} (S_i^x S_j^x + S_i^y S_j^y + \Delta S_i^z S_j^z) - H \sum_i S_i^x, \tag{1.5}$$

where $\Delta < 1$. For zero field, the spins form the 120° structure with the spins in the xy-plane. For nonzero field, the Hamiltonian has no longer the continuous symmetry,

but the ground state of this system is still continuously degenerate, as shown below. It is reasonable to assume that the spins remain in the xy-plane for nonzero field. In this case the spin directions are expressed in terms of the angles from the applied field as

$$\boldsymbol{S}_i = S(\cos\phi_i, \sin\phi_i, 0). \tag{1.6}$$

The energy expression corresponding to Eq. (1.3) for this case is

$$\frac{E}{N} = -3JS^2(1+3h^2) + JS^2[(\cos\phi_1 + \cos\phi_2 + \cos\phi_3 - 3h)^2 + (\sin\phi_1 + \sin\phi_2 + \sin\phi_3)^2], \tag{1.7}$$

where $h = H/18JS$. Thus the condition for the ground state can be expressed as

$$\begin{cases} \cos\phi_1 + \cos\phi_2 + \cos\phi_3 = 3h, \\ \sin\phi_1 + \sin\phi_2 + \sin\phi_3 = 0. \end{cases} \tag{1.8}$$

Here we have three parameters ϕ_1, ϕ_2, ϕ_3; however Eq. (1.8) gives only two conditions, and therefore the ground state is nontrivially degenerate [1]. The umbrella-type spin structure of Fig. 1.1(a) is not a ground state, but the other three structures in Fig. 1.1 still belong to the subset of ground states. We can express the angles ϕ_1 and ϕ_2 in terms of ϕ_3 by

$$\cos\phi_1 = \frac{1}{2}(3h - \cos\phi_3) + t\sin\phi_3, \quad \sin\phi_1 = -\frac{1}{2}\sin\phi_3 + t(3h - \cos\phi_3),$$

$$\cos\phi_2 = \frac{1}{2}(3h - \cos\phi_3) - t\sin\phi_3, \quad \sin\phi_2 = -\frac{1}{2}\sin\phi_3 - t(3h - \cos\phi_3), \tag{1.9}$$

$$t^2 + \frac{1}{4} = (9h^2 - 6h\cos\phi_3 + 1)^{-1}.$$

For $h < 1/3$, all values of ϕ_3 are allowed, and ϕ_1 and ϕ_2 increase monotonically with ϕ_3. For $1/3 < h < 1$, values of the phases ϕ_i near π are forbidden; the precise requirement is

$$\cos\phi_i \geq \frac{3h^2 - 1}{2h}. \tag{1.10}$$

The forbidden region grows with h until the fully aligned state is reached at $h = 1$. Also for $1/3 < h < 1$, ϕ_1 and ϕ_2 are not monotonic functions of ϕ_3.

1.1.2 Thermal Fluctuations

Since the nontrivial degeneracy of the classical ground state does not reflect the symmetry of the system, the degeneracy does not usually persist when we consider perturbations such as thermal fluctuations at finite temperatures or zero-point quantum fluctuations. Kawamura [1] investigated the effect of thermal fluctuations on the antiferromagnetic plane-rotator model on the triangular lattice. He calculated the free energy using the harmonic approximation. The calculation is performed by expanding in the deviations (assumed small) of the spin directions from the equilibrium values; the stable configurations (ϕ_1, ϕ_2, ϕ_3) are given by Eq. (1.9). At finite temperatures, the spins will deviate from the ground-state configurations due to thermal fluctuations. The expansion of the Hamiltonian to second order in the deviations $x_{in}^{(l)} = \phi_{in}^{(l)} - \phi_l$ is

$$\mathcal{H} = E_0 + \mathcal{H}_2, \tag{1.11}$$

where $\mathcal{H}_2$ denotes terms quadratic in $\{x_{in}\}$. Since we are expanding about the equilibrium configuration, the linear term disappears. Introducing the Fourier transformation of x on each sublattice as

$$x_j^{(l)} = \sqrt{\frac{3}{N}} \sum_{\boldsymbol{k}} x_{\boldsymbol{k}}^{(l)} \exp(i\boldsymbol{k} \cdot \boldsymbol{r}_j), \tag{1.12}$$

we can write the quadratic part as

$$\mathcal{H}_2 = \frac{S^2}{2} \sum \boldsymbol{x}_{-\boldsymbol{k}}^T A_{\boldsymbol{k}} \boldsymbol{x}_{\boldsymbol{k}}, \tag{1.13}$$

where the summation runs over the reduced Brillouin zone; the column vector $\boldsymbol{x}$ is defined by

$$\boldsymbol{x}^T = (x^{(1)}, x^{(2)}, x^{(3)}). \tag{1.14}$$

The matrix $A_{\boldsymbol{k}}$ is defined by

$$A_{\boldsymbol{k}} = 6J \begin{pmatrix} 1 & \nu_{\boldsymbol{k}} \cos\phi_{12} & \nu_{\boldsymbol{k}}^* \cos\phi_{13} \\ \nu_{\boldsymbol{k}}^* \cos\phi_{21} & 1 & \nu_{\boldsymbol{k}} \cos\phi_{23} \\ \nu_{\boldsymbol{k}} \cos\phi_{31} & \nu_{\boldsymbol{k}}^* \cos\phi_{31} & 1 \end{pmatrix}, \tag{1.15}$$

where $\phi_{ij} = \phi_i - \phi_j$, and the complex quantity $\nu_{\boldsymbol{k}}$ is defined by

$$\nu_{\boldsymbol{k}} = \frac{1}{3} \left[\exp(ik_x) + \exp\left(i \frac{-k_x + \sqrt{3}k_y}{2} \right) + \exp\left(i \frac{-k_x - \sqrt{3}k_y}{2} \right) \right]. \tag{1.16}$$

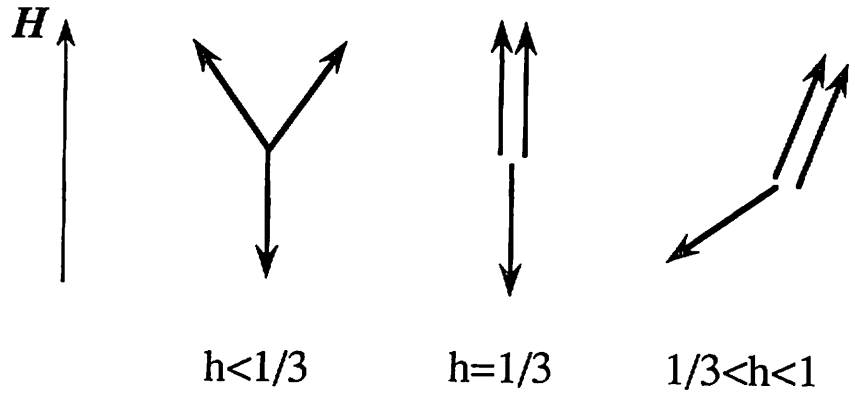

Figure 1.2: Field dependence of equilibrium spin configurations in the low-temperature limit.

Within this approximation, the free energy is found to be

$$F \simeq E_0 + \frac{NT}{2}\ln\frac{\pi S^2}{T} + \frac{T}{2}\sum_{\boldsymbol{k}}\ln(\det A_{\boldsymbol{k}}), \tag{1.17}$$

where the Boltzmann constant is taken to be unity. The determinant of $A_{\boldsymbol{k}}$ is given by

$$\det A_{\boldsymbol{k}} = 1 + (\nu_{\boldsymbol{k}}^3 + \nu_{\boldsymbol{k}}^{*3})\cos\phi_{12}\cos\phi_{23}\cos\phi_{31} - |\nu_{\boldsymbol{k}}|^2(\cos^2\phi_{12} + \cos^2\phi_{23} + \cos^2\phi_{31}). \tag{1.18}$$

Now the problem is to minimize (1.17) under the condition (1.8); solutions are the following:

(I) $0 < h < 1/3$

$$\phi_1 = \pi,\ \phi_2 = \cos^{-1}\frac{1+3h}{2},\ \phi_3 = -\phi_2. \tag{1.19}$$

(II) $1/3 < h < 1$

$$\phi_1 = \cos^{-1}\frac{3h^2-1}{2h},\ \phi_2 = \phi_3 = \cos^{-1}\frac{3h^2+1}{4h}. \tag{1.20}$$

These solutions represent the equilibrium spin configurations in the low-temperature limit. Figure 1.2 shows the resulting spin configurations. The entropy term strongly favors the collinear state, in which spins on two sublattices are parallel and spins on the other sublattice are antiparallel to the external field. Thus one expects that, at finite temperatures, the collinear state might be stabilized over a finite range of magnetic fields due to thermal fluctuations.

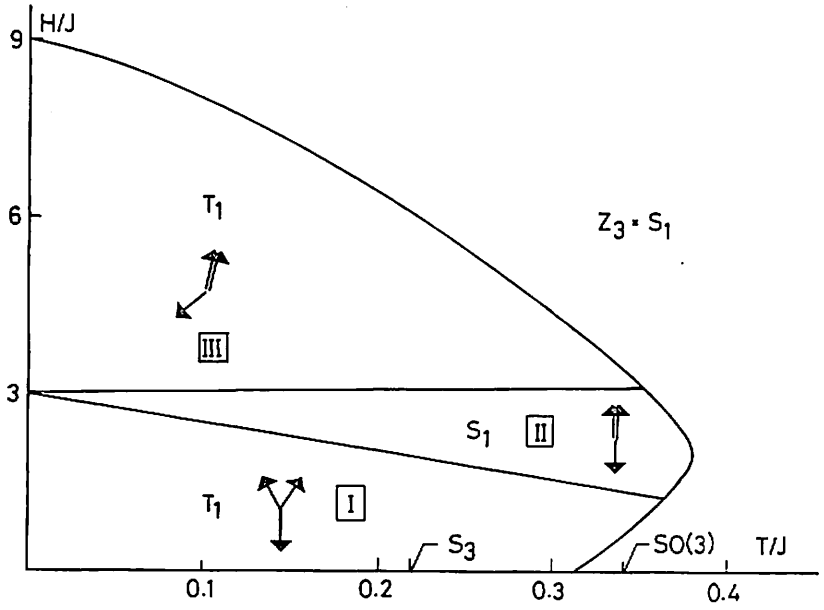

Figure 1.3: Temperature-magnetic field phase diagram of triangular antiferromagnet [2].

The harmonic approximation can be applied also to the Heisenberg antiferromagnet. The detailed calculation is presented in chapter 2, and thus we present here only the conclusion of the harmonic analysis. The entropy term favors the coplanar configuration in which all spins lie in the same plane (which includes the field direction). The dependence of the free energy on the inplane arrangement is exactly the same as in the plane-rotator model. Therefore the stable spin configuration in the low-temperature limit is the same as in the plane-rotator model.

Kawamura and Miyashita performed a Monte Carlo simulation of the Heisenberg antiferromagnet on the triangular lattice in a magnetic field [2]. They found that the spin-reorientation process occurs in the same way as in the plane-rotator model. All spins remain in the common plane (which includes the field direction), and reorientate via the intermediate collinear structure as shown in Fig. 1.2. Figure 1.3 is a schematic H-T phase diagram illustrated by Kawamura and Miyashita [2]. Note that the collinear state persists for a finite range of the field at finite temperatures.

1.1.3 Quantum Fluctuations

Quantum fluctuations are also expected to remove the continuous degeneracy in the classical ground state. This type of problem is often studied by using the spin-wave approach, based on the $1/S$ expansion. In the formulation of the spin-wave theory, the spin operators are transformed to boson operators through the Holstein-Primakoff transformation

$$S^{\zeta} = S - a^{\dagger}a, \;\; S^{\xi} + iS^{\eta} = (2S - a^{\dagger}a)^{1/2}a, \;\; S^{\xi} - iS^{\eta} = a^{\dagger}(2S - a^{\dagger}a)^{1/2}. \qquad (1.21)$$

The local spin coordinate system (ξ, η, ζ) should be chosen so that the ζ axis coincides with the classical spin direction. The $1/S$ correction to the ground-state energy is obtained as the zero-point fluctuation energy of the bosons. In all cases the problem is to find a canonical transformation which diagonalizes the quadratic part of the Hamiltonian (expressed in terms of the boson operators). Using the spin-wave theory, Chubukov and Golosov [3] investigated the magnetic structure of Heisenberg antiferromagnets on the triangular lattice in magnetic fields. The spin-wave calculation is reproduced in chapter 2 and so we do not present here the detailed calculations. They showed that the quantum lowering of the energy in the low-field limit (of order H^2) is lower for the coplanar configurations than for the umbrella-type configuration. All of the coplanar configuration satisfying the condition (1.8) are degenerate to order H^2. The next higher-order term takes the following form:

$$\Delta E/JS = A \cos 3\phi_1 \; h^3. \qquad (1.22)$$

The coefficient A can be calculated by numerical integration; it appears to be positive [12]. This means that the most stable state at low field is the one with $\phi_1 = \pi$, precisely the same as the one selected by thermal fluctuations. Thus they concluded that quantum fluctuations select the same mode of reorientation as do thermal fluctuations, as shown in Fig. 1.2. In fact we can confirm this conclusion by calculating the zero-point energies for various spin configurations for arbitrary H and comparing them. Moreover Chubukov and Golosov claimed that the collinear configuration is stabilized over a finite range of magnetic fields by quantum fluctuations so that the magnetization curve shows a plateau near one third of the saturation field. Figure 1.4 is the behavior of magnetization proposed by Chubukov and Golosov. The existence of the plateau has been suggested also by other authors [13-15].

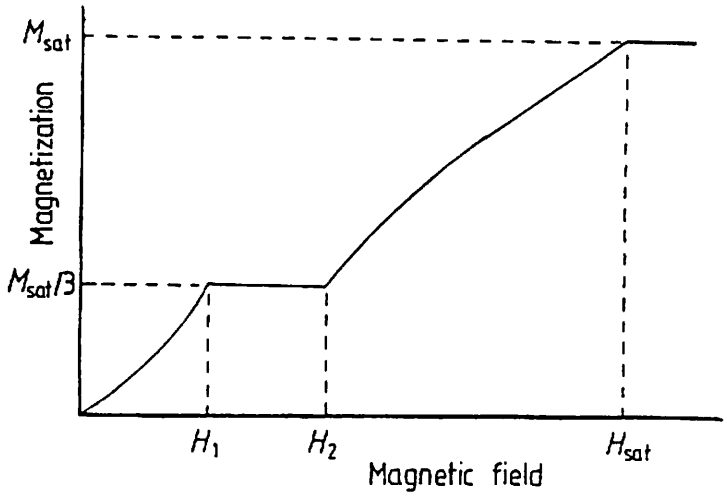

Figure 1.4: Anticipated magnetization curve of the triangular antiferromagnet in a magnetic field according to [3]. The plateau on the magnetization curve results from the stabilization of the collinear phase due to zero-point motion in the finite region of magnetic fields .

Let us consider the three-dimensional hexagonal antiferromagnet but with the ferromagnetic interaction along the c-axis. At least for the ground state within the classical theory, it is reasonable to assume that the spins are aligned uniformly within each chain so that the situation is completely the same as for the two-dimensional triangular antiferromagnet. Therefore the ground state has the nontrivial continuous degeneracy, which is lifted by thermal or quantum fluctuations. Most of the ABX_3 hexagonal antiferromagnets (such as $CsNiCl_3$) have antiferromagnetic intrachain interactions. One of few exceptions, $CsCuCl_3$, is known to be a hexagonal antiferromagnet with ferromagnetic intrachain interactions.

1.2 Experimental Background of $CsCuCl_3$

1.2.1 Basic Features

The magnetic properties of hexagonal ABX_3-type compounds have been widely investigated in the last two decades. In these compounds, magnetic B^{2+} ions form a hexagonal lattice. The exchange interaction between the c-chains is antiferromagnetic and generally weak because of the large separation between B^{2+} ions in the c-plane. Therefore these compounds are often regarded as quasi-one-dimensional

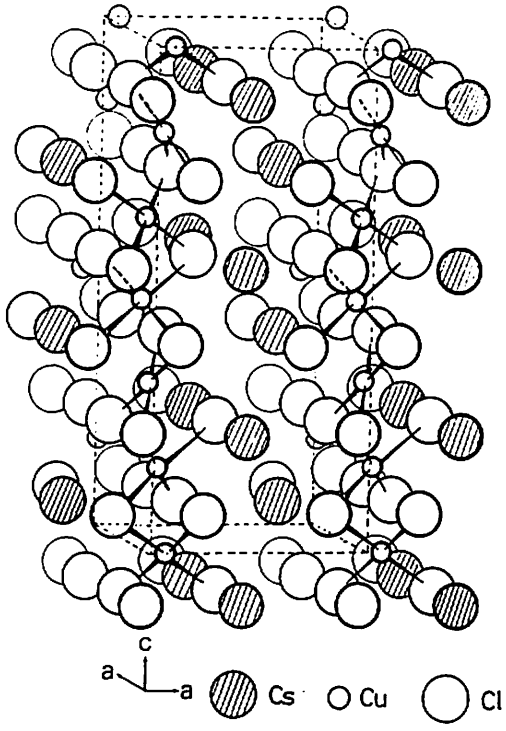

Figure 1.5: Crystal structure of $CsCuCl_3$ [19].

magnets. The frustration of the triangular network in the c-plane produces rich magnetic properties in many ABX_3-type magnetic compounds.

Cesium cupper chloride ($CsCuCl_3$) is a member of ABX_3-type compounds; the magnetic Cu^{2+} ion has $S = 1/2$. Unlike many other ABX_3 compounds such as $CsNiCl_3$, the exchange interaction along the c-axis is ferromagnetic. At high temperatures, the lattice structure of $CsCuCl_3$ is the same as other ABX_3-type compounds such as $CsNiCl_3$. But it undergoes a structural phase transition at 423K leading to a helical atomic displacement along the c-axis. This is attributed to the cooperative Jahn-Teller effect of the Cu^{2+} ions [16]. Figure 1.5 shows the crystal structure of $CsCuCl_3$ at room temperature. In this structure, the six Cu^{2+} ions contained in a unit cell form a helix. The low symmetry of the local structure leads to an antisymmetric Dzyaloshinsky-Moriya (DM) interaction between neighboring spins along the c-chains.

The magnetic properties of $CsCuCl_3$ have been studied by several authors. Tazuke *et al.* measured the paramagnetic susceptibility in order to determine the exchange parameters [17]. The positive Weiss temperature indicates that the dominant ex-

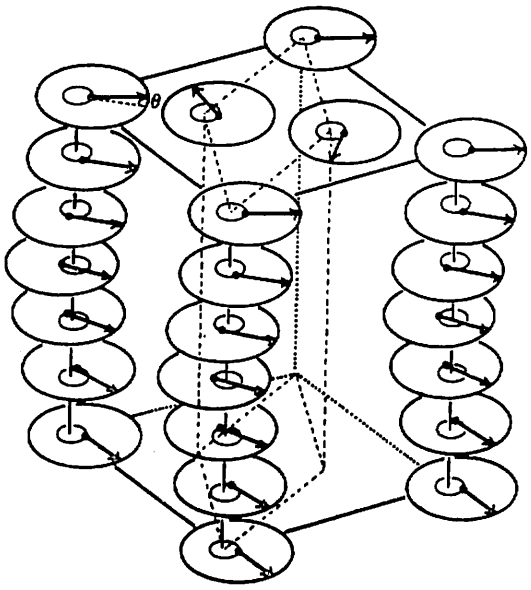

Figure 1.6: Magnetic structure of $CsCuCl_3$ [19]. The spin moments lie in the c-plane and the turning angle θ is 5.1°. The dashed line shows the chemical unit cell.

change interaction is ferromagnetic. The exchange parameters, estimated by comparing the experimental curve with the theoretical one calculated by the high-temperature expansion method, are $J_0 = 24$K and $J_1/J_0 = 0.16$. Hyodo *et al.* estimated J_0 and J_1 from optical measurements [18]; their results are $J_0 = 32$K and $J_1/J_0 = 0.07$. The ratio J_1/J_0 is relatively large compared to other ABX_3-type compounds such as $CsNiCl_3$.

Three-dimensional antiferromagnetic ordering occurs at $T_N = 10.5$K in $CsCuCl_3$. Adachi *et al.* investigated the spin structure of $CsCuCl_3$ in the ordered phase by neutron scattering [19]. As shown in Fig. 1.6, the moments lie in the c-plane (with the 120° structure) and form a helical spin structure with a long period along the c-axis. The turning angle of the spins is about 5.1°; thus the period of the helix is about 71 layers. The helical structure can be explained as a competition between the ferromagnetic intrachain exchange interaction and the DM interaction.

1.2.2 Magnetization Process

In 1978 Motokawa [10] performed a magnetization measurement on $CsCuCl_3$ using pulsed high magnetic fields. He discovered an anomaly in the magnetization process for a field applied parallel to the c-axis. Figure 1.7(a) is a reproduced magnetization

curve [11]. When the external field is applied parallel to the c-axis, the magnetization increases almost linearly but then shows a small jump at $H_c = 12.5$T. Above H_c, the magnetization increases again and saturates at $H_s = 31$T. The magnitude of the magnetization jump at H_c is $0.013\mu_B$; the saturated magnetization value is $1.1\mu_B$. The magnetization measurements were carried out at various temperatures between 1.1K and T_N. The temperature dependence of the transition field H_c and the saturation field H_s are given as a phase diagram in Fig. 1.7(b). H_c and H_s gradually decrease with increasing temperature. The magnitude of the magnetization jump is almost constant below 3K.

Fedoseeva *et al.* also carried out magnetization measurements near T_N in fields up to 8T using a superconducting magnet [20]. As shown in Fig. 1.8, they too found a small jump of magnetization for a magnetic field parallel to the c-axis. Their results are consistent with the phase diagram of Ref. 11 in the vicinity of T_N (see Fig. 1.7(b)).

If we apply the classical (mean-field) theory to reasonable models of $CsCuCl_3$, we expect that spins should simply stand up from the c-plane so as to form the umbrella-like spin structure shown in Fig. 1.1(a), when the field is applied along the c-axis. The umbrella should close with increasing field, and smoothly shrinks into a finally ferromagnetic state. Thus the classical theory based on the simple model Hamiltonian cannot explain the observed magnetization jump, and the anomaly of the magnetization process of $CsCuCl_3$ has been a mystery for a long time. We show in this thesis that this anomaly can be understood in terms of quantum fluctuations.

When an external field is applied perpendicular to the c-axis, the magnetization increases with increasing field but then shows a small plateau at around 12T, as shown in Fig. 1.7(a). After the plateau, the magnetization increases again up to the saturation field. The saturation field for the perpendicular configuration is a little smaller than for the parallel field case. In the zero-field case, spins form the helical structure; on the other hand, they are aligned ferromagnetically above the saturation field. Therefore there must be transitions from the helical structure to ferromagnetically aligned state; in the intermediate-field region, the spins realize complicated structures. Even in mean-field (classical) theory the problem is far from trivial. This problem is discussed in chapter 4.

Although $CsCuCl_3$ is not completely equivalent to the isotropic triangular anti-

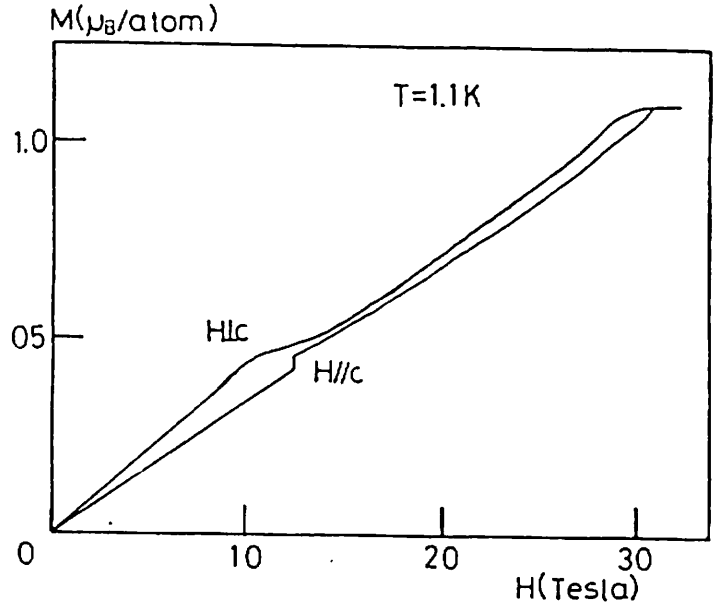

(a)

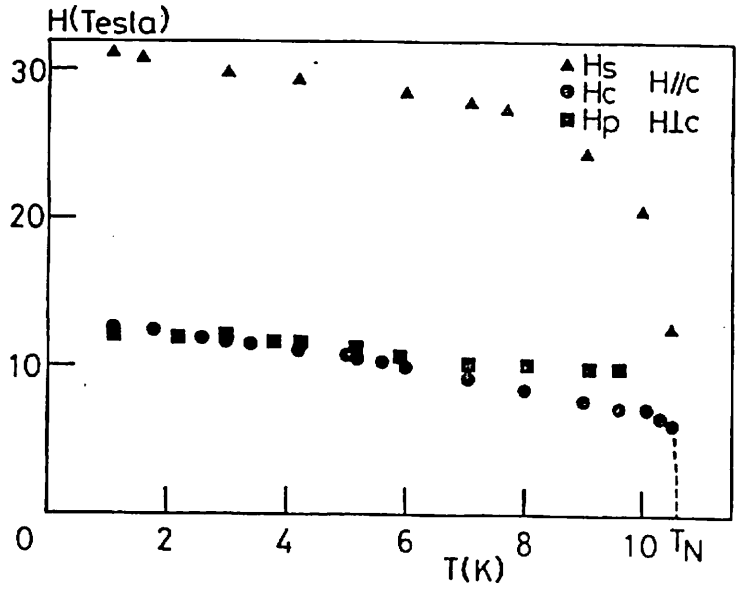

(b)

Figure 1.7: Magnetization experiments on $CsCuCl_3$ [11]. (a) Magnetization curve of $CsCuCl_3$. (b) Temperature dependence of saturation field H_s, transition field H_c for $H||c$ and plateau field H_p for $H \perp c$.

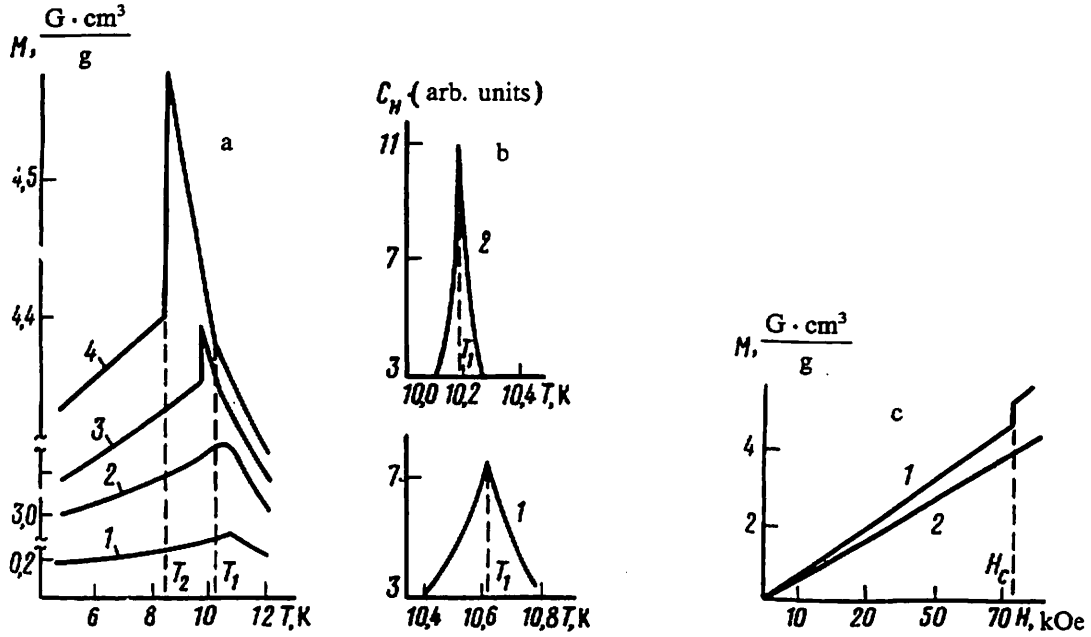

Figure 1.8: The magnetic behavior of $CsCuCl_3$ in a field directed along the c-axis [20]. a: Temperature dependence of the magnetic moment of $CsCuCl_3$ for various fields. 1–3.3kOe; 2–50kOe; 3–60kOe; 4-71.6kOe. b: The magnetic part of the heat capacity as a function of the temperature. 1–At $H = 60$kOe: 2–$H = 71.6$kOe. c: Dependence of the magnetic moment of $CsCuCl_3$ in an external field. 1–At $T = 8.7$K; 2–$T = 4.2$K.

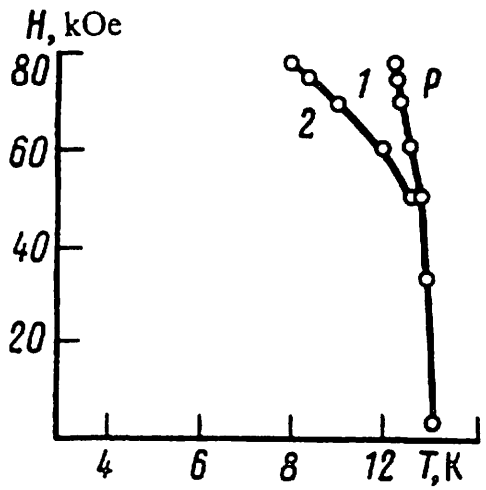

Figure 1.9: The H-T phase diagram of $CsCuCl_3$. P represents the paramagnetic phase [20].

ferromagnet (due to weak anisotropy), the situation is close to what we discussed in section 1.1. We show in this thesis that $CsCuCl_3$ is a good example to explore the physics of quantum fluctuations in the case of nontrivial degeneracy.

1.3 Outline of Thesis

This thesis studies theoretically the effect of quantum fluctuations in hexagonal antiferromagnets in external fields in connection with real materials such as $CsCuCl_3$.

In chapter 2 we present a theoretical interpretation for the jump of the magnetization in $CsCuCl_3$ observed for $H||c$. It is shown that quantum fluctuations are so important that they changes the ground-state spin structure. The observed anomaly in the magnetization is well explained as a spin-flop phase transition caused by quantum fluctuations.

In chapter 3 we study the ground-state spin structure in a strong field just below saturation, using the exact hard-core-boson representation for $S = 1/2$ spins. The magnetic ordering problem near saturation is mapped onto the Bose condensation in a low-density Bose gas. We then apply the low-density expansion to the problem, and determine the ground state spin structure near the saturation field.

In chapter 4 we study the magnetic structure of $CsCuCl_3$ in a transverse magnetic field. First we apply the classical theory and determine the ground-state spin structure. We show that the transverse field deforms the helical spin structure and causes a complicated incommensurate magnetic structure. Next we take into account quantum fluctuations; we see that the classical incommensurate structure is largely modified by quantum fluctuations.

Chapter 5 gives a summary and discussion.

Chapter 2

Quantum Fluctuations and Magnetic Phase Transition in $CsCuCl_3$

This chapter presents a theoretical interpretation of the small magnetization jump in $CsCuCl_3$ for a field applied parallel to the c-axis. The contents were already published in Ref. 21 as "Quantum Fluctuations and Magnetic Structures of $CsCuCl_3$ in High Magnetic Field"; modifications have been made for convenience and for simplicity.

2.1 Introduction

The spin structures in most magnetic substances are well determined by the classical (mean-field) theory. It is generally believed therefore that quantum fluctuations do not change the nature of the ground-state spin ordering in an essential manner. However, there are some exceptions to this rule. It has been known theoretically that frustrated spin systems often show nontrivial continuous degeneracy in their classical ground state. Such a degeneracy is usually removed by thermal and/or quantum fluctuations. Several authors have already recognized such a possibility for some frustrated spin systems [1-9]. The purpose of this chapter is to show that $CsCuCl_3$ in a magnetic field applied parallel to the c-axis is an example of a real system in which the quantum fluctuations are crucial in determining the ground-state spin structure. We show that the unexpected behavior of the magnetization in $CsCuCl_3$ [10,11] is a manifestation of quantum fluctuations.

This chapter is organized as follows. In section 2.2 the classical theory is applied to determine the classical ground-state spin structure. The effect of quantum fluctu-

ations is then examined in section 2.3 by using the spin-wave theory. In section 2.4 we study the effect of thermal fluctuations in the low-temperature limit. Section 2.5 reviews the experimental determination of the magnetic structure in the high-field region. Section 2.6 summarizes this chapter.

2.2 Classical Ground State

Let us write the model Hamiltonian of $CsCuCl_3$ in a magnetic field applied parallel to the c-axis as

$$\mathcal{H} = -2J_0 \sum_{in}[\boldsymbol{S}_{in} \cdot \boldsymbol{S}_{in+1} + \eta(S^x_{in}S^x_{in+1} + S^y_{in}S^y_{in+1})] + 2J_1 \sum_{\langle ij\rangle n} \boldsymbol{S}_{in} \cdot \boldsymbol{S}_{jn} - \sum_{in} \boldsymbol{D}_{nn+1} \cdot (\boldsymbol{S}_{in} \times \boldsymbol{S}_{in+1}) - g\mu_B \sum_{in} \boldsymbol{H} \cdot \boldsymbol{S}_{in}, \tag{2.1}$$

where $\boldsymbol{S}_{in}$ represents a spin operator ($S = 1/2$) located at the i-th site in the n-th c-plane. The summation $\langle ij\rangle$ is taken over all nearest-neighbor pairs in the c-plane. The z-axis is taken parallel to the c-axis. The first and second terms are the intrachain ferromagnetic exchange interaction and the interchain antiferromagnetic exchange interaction, respectively. $\eta(> 0)$ is a weak anisotropic exchange interaction of easy-plane type; the importance of this term for the interpretations of ESR experiment [23] has been pointed out by Tanaka *et al.* [22]. The third term is the DM interaction; the $\boldsymbol{D}_{nn+1}$ vector is assumed to be parallel to the c-axis. The fourth term is the Zeeman energy. The dipole-dipole interaction is considered to be small and is neglected for simplicity.

The DM term can be eliminated by using a new spin coordinate system in which the xy-plane is rotated by an angle q along the z-axis:

$$\begin{cases} S^x_{in} = S^{x'}_{in} \cos nq - S^{y'}_{in} \sin nq, \\ S^y_{in} = S^{x'}_{in} \sin nq + S^{y'}_{in} \cos nq. \end{cases} \tag{2.2}$$

The Hamiltonian is then transformed to

$$\mathcal{H} = -\sum_{in}[2\tilde{J}_0(S^x_{in}S^x_{in+1} + S^y_{in}S^y_{in+1}) + 2J_0 S^z_{in}S^z_{in+1}] + 2J_1 \sum_{<ij>n} \boldsymbol{S}_{in} \cdot \boldsymbol{S}_{jn} - g\mu_B H \sum_{in} S^z_{in}, \tag{2.3}$$

where

$$\tilde{J}_0 = J_0\sqrt{(1+\eta)^2 + \left(\frac{D}{2J_0}\right)^2}, \quad D \equiv |D^z_{nn+1}|. \tag{2.4}$$

The primes ($'$) in Eq. (2.2) are omitted from the Hamiltonian (2.3), for simplicity. The rotation angle q is determined so as to eliminate the asymmetric term: $\tan q = D/2J_0(1+\eta)$. According to the experimental results [22], $\tilde{J}_0$ is estimated to be $\tilde{J}_0 = 1.012J_0$. Note that the antisymmetric interaction has been reduced to a weak anisotropy of easy-plane type.

The classical ground state of the triangular antiferromagnet has the 3-sublattice structure; we label the sublattices by $l = 1, 2, 3$. The ground-state energy is described in terms of the sublattice moments $\boldsymbol{S}_1, \boldsymbol{S}_2, \boldsymbol{S}_3$:

$$\begin{aligned}\frac{E_0}{N} = &-2\tilde{J}_0 S^2 + \frac{2}{3}\Delta J_1[(S_1^z)^2 + (S_2^z)^2 + (S_3^z)^2] \\ &+2J_1(\boldsymbol{S}_1\cdot\boldsymbol{S}_2 + \boldsymbol{S}_2\cdot\boldsymbol{S}_3 + \boldsymbol{S}_3\cdot\boldsymbol{S}_1) - \frac{1}{3}g\mu_{\rm B}H(S_1^z + S_2^z + S_3^z),\end{aligned} \tag{2.5}$$

where N represents the total number of spins. The anisotropy parameter Δ is defined by $\Delta = (\tilde{J}_0 - J_0)/J_1 = 0.07$. At zero field, the classical ground state is the 120° structure with all spins lying in the c-plane. This spin structure is consistent with the result of the neutron scattering experiment [19] shown in Fig. 1.6. To consider the spin structures at finite fields, it is convenient to express $\boldsymbol{S}_l$ in terms of the polar coordinates:

$$\boldsymbol{S}_l = (S\cos\phi_l \sin\theta_l, S\sin\phi_l\sin\theta_l, S\cos\theta_l). \tag{2.6}$$

Then we shall consider the four types of spin configurations in Fig. 2.1; all are possible candidates for the ground state.

[I] umbrella-type configuration

First we calculate the classical energy of the umbrella-type spin structure in Fig. 2.1(a). Within the classical theory, this spin structure is expected to be the ground-state spin structure. In this case we have $\theta_l \equiv \theta$ and $\phi_l = 2\pi(l-1)\pi/3 + \phi_1$. The classical energy E_0 is given by

$$\frac{E_0}{N} = -2\tilde{J}_0 S^2 - 3J_1 S^2 + (2\Delta + 9)J_1 S^2\cos^2\theta - g\mu_{\rm B}SH\cos\theta. \tag{2.7}$$

The angle θ between the moments and the magnetic field is determined by minimizing the above expression, yielding

$$\cos\theta = \frac{g\mu_{\rm B}H}{(18+4\Delta)J_1 S}. \tag{2.8}$$

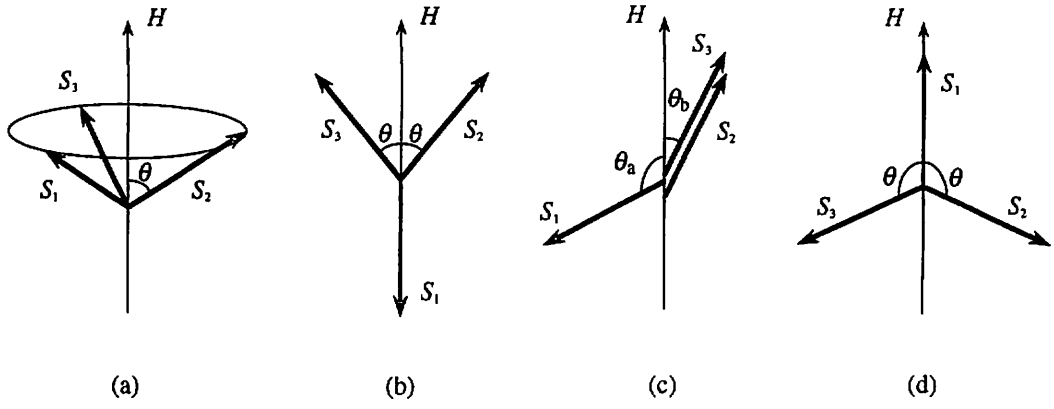

Figure 2.1: Four types of spin configurations of the triangular antiferromagnet in a magnetic field. (a) The umbrella-type configuration. The c-plane components of the spins form the 120° structure. (b) The coplanar configuration for $H < H_s/3$. The spins lie in a plane including the c-axis. (c) The coplanar configuration for $H > H_s/3$. Two of the three spins are oriented along the same direction. (d) The coplanar configuration, which is the inversion of the configuration (b).

The magnetization is given by $M = g\mu_B S\cos\theta$; it increases linearly with the external field and saturates at

$$H_s = (18 + 4\Delta)J_1 S/g\mu_B. \tag{2.9}$$

Substituting (2.8) into (2.7), we have the minimum energy of this configuration as

$$\frac{E_0}{N} = -(2\tilde{J}_0 + 3J_1)S^2 - \frac{1}{2}g\mu_B S H_s h^2, \tag{2.10}$$

where $h = H/H_s$.

[II] coplanar configurations

To describe the coplanar configurations, we put $\phi_1 = \phi_2 = \phi_3 = 0$ and take θ_l between $-\pi$ and π; in this treatment we assume that the spins lie in the xz plane. In the following we consider the three types of coplanar configurations in Fig. 2.1.

(i) $\theta_1 = \pi$ and $\theta_2 = -\theta_3 \equiv \theta$ (Fig. 2.1(b))

The classical energy for this configuration is

$$\frac{E_0}{N} = -2\tilde{J}_0 S^2 + \frac{2}{3}\Delta J_1 S^2(1 + 2\cos^2\theta) + 2J_1 S^2(\cos 2\theta - 2\cos\theta) - \frac{1}{3}g\mu_B S H(2\cos\theta - 1). \tag{2.11}$$

Minimizing (2.11) with respect to θ, we have

$$\cos\theta = \frac{(g\mu_B H/S) + 6J_1}{(12+4\Delta)J_1}. \tag{2.12}$$

The minimum energy for this configuration is obtained by substituting (2.12) into (2.11). Since Δ is small in $CsCuCl_3$, we expand the energy with respect to Δ as

$$\frac{E_0}{N} = -(2\tilde{J}_0 + 3J_1)S^2 - \frac{1}{2}g\mu_B S H_s h^2 + \Delta J_1(1+h)^2 S^2 + O(\Delta^2). \tag{2.13}$$

The third term of the above equation is the energy difference from the umbrella configuration; it is always positive for $\Delta > 0$.

(ii) $\theta_1 = -\theta_a$ and $\theta_2 = \theta_3 = \theta_b$ (Fig. 2.1(c))

The classical energy of this configuration is given by

$$\begin{aligned}\frac{E_0}{N} = &-2\tilde{J}_0 S^2 + \frac{2}{3}\Delta J_1 S^2(\cos^2\theta_a + 2\cos^2\theta_b) \\ &+2J_1 S^2[1 + 2\cos(\theta_a + \theta_b)] - \frac{1}{3}g\mu_B S H(\cos\theta_a + 2\cos\theta_b).\end{aligned} \tag{2.14}$$

From the conditions $\partial E_0/\partial\theta_a = 0$ and $\partial E_0/\partial\theta_b = 0$, the following two equations are obtained:

$$\begin{cases} \Delta\sin 2\theta_a + 6\sin(\theta_a+\theta_b) - (9+2\Delta)h\sin\theta_a = 0, \\ \Delta\sin 2\theta_b + 3\sin(\theta_a+\theta_b) - (9+2\Delta)h\sin\theta_b = 0. \end{cases} \tag{2.15}$$

For $\Delta = 0$, the solutions of these equations are given by Eq. (1.20) on replacing (ϕ_1, ϕ_2) by $(-\theta_a, \theta_b)$. For $\Delta \neq 0$, it is difficult to solve equation (2.15) for the general case. However for small Δ, we can expand $\cos\theta_a$ and $\cos\theta_b$ in Δ:

$$\begin{cases} \cos\theta_a = \dfrac{3}{2}h - \dfrac{1}{2h} + \Delta\dfrac{(1-h^2)(7-3h^2)}{36h^2} + O(\Delta^2), \\ \cos\theta_b = \dfrac{3}{4}h + \dfrac{1}{4h} - \Delta\dfrac{(1-h^2)(2-3h^2)}{36h^2} + O(\Delta^2). \end{cases} \tag{2.16}$$

Substituting (2.16) into (2.14), we obtain the energy of this configuration to first order in Δ as

$$\frac{E_0}{N} = -(2\tilde{J}_0 + 3J_1)S^2 - \frac{1}{2}g\mu_B S H_s h^2 + \Delta J_1 S^2\frac{(1-h^2)^2}{4h^2} + O(\Delta^2). \tag{2.17}$$

Since the anisotropy is of easy-plane type ($\Delta > 0$), this spin structure has higher energy than the umbrella-type structure.

(iii) $\theta_1 = \pi, \theta_2 = -\theta_3 \equiv \theta$ (Fig. 2.1(d))

The classical energy for this configuration is

$$\frac{E_0}{N} = -2\tilde{J}_0 S^2 + \frac{2}{3}\Delta J_1 S^2(1 + 2\cos^2\theta) + 2J_1 S^2(\cos 2\theta + 2\cos\theta) - \frac{1}{3}g\mu_B SH(2\cos\theta + 1). \tag{2.18}$$

The angle θ, determined by minimizing the energy, is found from

$$\cos\theta = \frac{(g\mu_B H/S) - 6J_1}{(12 + 4\Delta)J_1}. \tag{2.19}$$

The minimum energy for this configuration is obtained by substituting (2.19) into (2.18) as

$$\frac{E_0}{N} = -(2\tilde{J}_0 + 3J_1)S^2 - \frac{1}{2}g\mu_B SH_s h^2 + \Delta J_1(1-h)^2 S^2 + O(\Delta^2). \tag{2.20}$$

Although this energy is lower than that of the configuration (b) or (c), it is still higher than the energy of the umbrella-type.

We have thus shown that the three coplanar configurations (b), (c) and (d) have higher classical energy than the umbrella-type configuration (a). The higher energy is due to the small easy-plane anisotropy Δ. Actually for $\Delta = 0$, all configurations shown above satisfy the relation

$$\boldsymbol{S}_1 + \boldsymbol{S}_2 + \boldsymbol{S}_3 = \frac{g\mu_B H}{6J_1}, \tag{2.21}$$

and they all belong to the class of continuously degenerate ground states [2]. The small easy-plane anisotropy Δ removes the degeneracy and selects the umbrella-type configuration as the ground state. Note that the energy difference between coplanar and umbrella-type solutions, which is proportional to Δ for small Δ, is very small. Therefore, as shown in the next section, the classical energy difference can be overcome by quantum fluctuations.

2.3 Quantum Fluctuations

In this section we take into account the effect of quantum fluctuations by using the spin-wave theory; this allows us to give the first correction to the classical ground-state energy in the $1/S$ expansion. We evaluate the zero-point energy for the four

spin configurations for $\Delta = 0$, and see how quantum fluctuations lift the classical degeneracy.

[I] umbrella-type configuration

We take a local spin coordinate system ξ, η, ζ in which the ζ-axis coincides with the classical spin direction. The transformation in each sublattice is expressed in terms of the polar coordinate of the classical direction:

$$\begin{cases} S_{in}^{x} = -S_{in}^{\xi}\sin\phi_i - S_{in}^{\eta}\cos\theta\cos\phi_i + S_{in}^{\zeta}\sin\theta\cos\phi_i, \\ S_{in}^{y} = S_{in}^{\xi}\cos\phi - S_{in}^{\eta}\cos\theta\sin\phi_i + S_{in}^{\zeta}\sin\theta\sin\phi_i, \\ S_{in}^{z} = S_{in}^{\eta}\sin\theta + S_{in}^{\zeta}\cos\theta, \end{cases} \tag{2.22}$$

where the classical values θ and ϕ_i are given above. After the transformation (2.22), the spin Hamiltonian is written as

$$\begin{aligned} \mathcal{H} = & -2J_0\sum_{in}(S_{in}^{\xi}S_{in+1}^{\xi} + S_{in}^{\eta}S_{in+1}^{\eta} + S_{in}^{\zeta}S_{in+1}^{\zeta}) \\ & +2J_1\sum_{<ij>n}\Big[-\frac{1}{2}S_{in}^{\xi}S_{jn}^{\xi} + \Big(1-\frac{3}{2}\cos^2\theta\Big)S_{in}^{\eta}S_{jn}^{\eta} - \frac{1}{2}(1-3\cos^2\theta)S_{in}^{\zeta}S_{jn}^{\zeta} \\ & +\frac{3}{2}\sin\theta\cos\theta(S_{in}^{\eta}S_{jn}^{\zeta} + S_{in}^{\zeta}S_{jn}^{\eta}) + \sin(\phi_i-\phi_j)(S_{in}^{\zeta}S_{jn}^{\xi}\sin\theta + S_{in}^{\xi}S_{jn}^{\eta}\cos\theta)\Big] \\ & -g\mu_B H\sum_{in}(S_{in}^{\eta}\sin\theta + S_{in}^{\zeta}\cos\theta). \end{aligned} \tag{2.23}$$

We then introduce the Holstein-Primakoff boson operators a_{in} defined by

$$S_{in}^{\zeta} = S - a_{in}^{\dagger}a_{in}, \quad S_{in}^{\xi} = \frac{\sqrt{2S}}{2}(a_{in}^{\dagger} + a_{in}), \quad S_{in}^{\eta} = i\frac{\sqrt{2S}}{2}(a_{in}^{\dagger} - a_{in}). \tag{2.24}$$

Substituting the boson operators into the Hamiltonian and neglecting terms higher than second order in these operators (according to the spirit of the $1/S$ expansion), we obtain a quadratic spin-wave Hamiltonian:

$$\begin{aligned} \mathcal{H}_{\rm SW} = & E_0 + S\sum_{in}[(4J_0+6J_1)a_{in}^{\dagger}a_{in} + 2J_0(a_{in+1}^{\dagger}a_{in} + a_{in}^{\dagger}a_{in+1})] \\ & +2J_1S\sum_{<ij>n}\Big\{-\frac{3}{4}(1-h^2)(a_{in}a_{jn} + a_{in}^{\dagger}a_{jn}^{\dagger}) \\ & +\Big[\frac{1}{4}(1-3h^2) + i\frac{\sqrt{3}}{2}h\Big](a_{in}^{\dagger}a_{jn} + a_{jn}^{\dagger}a_{in})\Big\}. \end{aligned} \tag{2.25}$$

The Fourier transforms of the boson operators are defined by

$$a_{in} = \sqrt{\frac{1}{N}}\sum_{\boldsymbol{k}} a_{\boldsymbol{k}}\exp(i\boldsymbol{k}\cdot\boldsymbol{r}_{in}); \tag{2.26}$$

the summation over the wavevector $\boldsymbol{k}$ is performed over the whole Brillouin zone. The spin-wave Hamiltonian is then written in the following form:

$$\begin{aligned}\mathcal{H}_{\rm SW} &= E_0 - (2J_0 + 3J_1)SN \\ &\quad + \frac{S}{2}\sum_{\boldsymbol{k}}[(A_{\boldsymbol{k}}(a^\dagger_{\boldsymbol{k}}a_{\boldsymbol{k}} + a_{-\boldsymbol{k}}a^\dagger_{-\boldsymbol{k}}) - B_{\boldsymbol{k}}(a_{\boldsymbol{k}}a_{-\boldsymbol{k}} + a^\dagger_{\boldsymbol{k}}a^\dagger_{-\boldsymbol{k}}) \\ &\quad - C_{\boldsymbol{k}}(a^\dagger_{\boldsymbol{k}}a_{\boldsymbol{k}} - a_{-\boldsymbol{k}}a^\dagger_{-\boldsymbol{k}})],\end{aligned} \tag{2.27}$$

where

$$A_{\boldsymbol{k}} = 4J_0(1-\cos k_z) + 3J_1[2 + (1-3h^2)\gamma_{\boldsymbol{k}}], \tag{2.28}$$

$$B_{\boldsymbol{k}} = 9J_1(1-h^2)\gamma_{\boldsymbol{k}}, \quad C_{\boldsymbol{k}} = 6\sqrt{3}J_1 h\lambda_{\boldsymbol{k}}, \tag{2.29}$$

$$\gamma_{\boldsymbol{k}} = \frac{1}{3}\left(\cos k_x + \cos\frac{k_x + \sqrt{3}k_y}{2} + \cos\frac{k_x - \sqrt{3}k_y}{2}\right), \tag{2.30}$$

$$\lambda_{\boldsymbol{k}} = \frac{1}{3}\left(\sin k_x - \sin\frac{k_x + \sqrt{3}k_y}{2} - \sin\frac{k_x - \sqrt{3}k_y}{2}\right). \tag{2.31}$$

The spin-wave Hamiltonian $\mathcal{H}_{\rm SW}$ is diagonalized by the Bogoliubov transformation

$$a_{\boldsymbol{k}} = u_{\boldsymbol{k}}\alpha_{\boldsymbol{k}} + v_{\boldsymbol{k}}\alpha^\dagger_{-\boldsymbol{k}}, \quad a^\dagger_{-\boldsymbol{k}} = v_{\boldsymbol{k}}\alpha_{\boldsymbol{k}} + u_{\boldsymbol{k}}\alpha^\dagger_{-\boldsymbol{k}}, \tag{2.32}$$

where

$$u_{\boldsymbol{k}} = \sqrt{\frac{1}{2}\left(\frac{A_{\boldsymbol{k}}}{\sqrt{A^2_{\boldsymbol{k}} - B^2_{\boldsymbol{k}}}} + 1\right)}, \quad v_{\boldsymbol{k}} = \mathrm{sgn}(\gamma_{\boldsymbol{k}})\sqrt{\frac{1}{2}\left(\frac{A_{\boldsymbol{k}}}{\sqrt{A^2_{\boldsymbol{k}} - B^2_{\boldsymbol{k}}}} - 1\right)}. \tag{2.33}$$

Then we obtain

$$\mathcal{H}_{\rm SW} = E_0 - (2J_0 + 3J_1)SN + S\sum_{\boldsymbol{k}}\omega_{\boldsymbol{k}}\left(\alpha^\dagger_{\boldsymbol{k}}\alpha_{\boldsymbol{k}} + \frac{1}{2}\right). \tag{2.34}$$

The spin-wave frequency $\omega_{\boldsymbol{k}}$ is given by

$$\begin{aligned}\omega_{\boldsymbol{k}} &= \sqrt{A^2_{\boldsymbol{k}} - B^2_{\boldsymbol{k}}} - C_{\boldsymbol{k}} \\ &= \sqrt{[4J_0(1-\cos k_z) + 6J_1(1-\gamma_{\boldsymbol{k}})]\{4J_0(1-\cos k_z) + 6J_1[1 + (2-3h^2)\gamma_{\boldsymbol{k}}]\}} \\ &\quad - 6\sqrt{3}J_1 h\lambda_{\boldsymbol{k}}.\end{aligned} \tag{2.35}$$

Then the leading quantum correction to the ground-state energy is given in the expected form:

$$\Delta E_{\rm SW} = -(2J_0 + 3J_1)SN + \frac{S}{2}\sum_{\boldsymbol{k}}\omega_{\boldsymbol{k}}. \tag{2.36}$$

In the reduced Brillouin zone scheme, $\Delta E_{\rm SW}$ can also be expressed as

$$\Delta E_{\rm SW} = -(2J_0 + 3J_1)SN + \frac{S}{2}\sum_{\boldsymbol{k}}{}'[\omega_1(\boldsymbol{k}) + \omega_2(\boldsymbol{k}) + \omega_3(\boldsymbol{k})]. \tag{2.37}$$

The three spin-wave branches are defined by $\omega_1(\boldsymbol{k}) = \omega_{\boldsymbol{k}}$, $\omega_2(\boldsymbol{k}) = \omega_{\boldsymbol{k}+\boldsymbol{Q}}$, and $\omega_3(\boldsymbol{k}) = \omega_{\boldsymbol{k}-\boldsymbol{Q}}$, where $\boldsymbol{Q} = (4\pi/3, 0, 0)$. The "prime" symbol on the sum $\sum$ indicates that the summation is performed over the reduced Brillouin zone.

[II] coplanar configurations

For the coplanar configurations, we use the following coordinate system:

$$\begin{cases} S_{in}^{x} = S_{in}^{\xi}\cos\theta_i + S_{in}^{\zeta}\sin\theta_i, \\ S_{in}^{y} = S_{in}^{\eta}, \\ S_{in}^{z} = -S_{in}^{\xi}\sin\theta_i + S_{in}^{\zeta}\cos\theta_i. \end{cases} \tag{2.38}$$

With the new coordinate system, the Hamiltonian becomes

$$\begin{aligned} \mathcal{H} = & -2J_0\sum_{in}(S_{in}^{\xi}S_{in+1}^{\xi} + S_{in}^{\eta}S_{in+1}^{\eta} + S_{in}^{\zeta}S_{in+1}^{\zeta}) \\ & +2J_1\sum_{<ij>n}[S_{in}^{\xi}S_{jn}^{\xi}\cos(\theta_i - \theta_j) + S_{in}^{\eta}S_{jn}^{\eta} + S_{in}^{\zeta}S_{jn}^{\zeta}\cos(\theta_i - \theta_j) \\ & +(S_{in}^{\zeta}S_{jn}^{\xi} - S_{in}^{\xi}S_{jn}^{\zeta})\sin(\theta_i - \theta_j)] \\ & -g\mu_{\rm B}H\sum_{in}(-S_{in}^{\xi}\sin\theta_i + S_{in}^{\zeta}\cos\theta_i). \end{aligned} \tag{2.39}$$

Substituting (2.24) in (2.39), we obtain a quadratic spin-wave Hamiltonian:

$$\begin{aligned} \mathcal{H}_{\rm SW} = & E_0 + S\sum_{in}[(4J_0 + 6J_1)a_{in}^{\dagger}a_{in} - 2J_0(a_{in}^{\dagger}a_{in+1} + a_{in+1}^{\dagger}a_{in})] \\ & +J_1S\sum_{<ij>n}\{[\cos(\theta_i - \theta_j) + 1](a_{in}^{\dagger}a_{jn} + a_{jn}^{\dagger}a_{in}) \\ & +[\cos(\theta_i - \theta_j) - 1](a_{in}a_{jn} + a_{jn}^{\dagger}a_{in}^{\dagger})\}. \end{aligned} \tag{2.40}$$

Fourier transformation for the boson operators is now defined on each sublattice (labeled by $l = 1, 2, 3$) as

$$a_{in} = \sqrt{\frac{3}{N}}\sum_{\boldsymbol{k}}{}'a_l(\boldsymbol{k})\exp(i\boldsymbol{k}\cdot\boldsymbol{r}_{in}). \tag{2.41}$$

Then the spin-wave Hamiltonian in the momentum space representation is expressed in the following matrix form:

$$\mathcal{H}_{\rm SW} = E_0 - (2J_0 + 3J_1)NS + \frac{S}{2}\sum_{\boldsymbol{k}}{}'\left[(\mathcal{A}_{\boldsymbol{k}}^{\dagger}, \mathcal{A}_{-\boldsymbol{k}})\begin{pmatrix} E_{\boldsymbol{k}} & F_{\boldsymbol{k}} \\ F_{\boldsymbol{k}} & E_{\boldsymbol{k}} \end{pmatrix}\begin{pmatrix} \mathcal{A}_{\boldsymbol{k}} \\ \mathcal{A}_{-\boldsymbol{k}}^{\dagger} \end{pmatrix}\right], \tag{2.42}$$

where $\mathcal{A}_{\boldsymbol{k}}$ is a three-component vector with $\mathcal{A}_{\boldsymbol{k}} = (a_1(\boldsymbol{k}), a_2(\boldsymbol{k}), a_3(\boldsymbol{k}))$, and $E_{\boldsymbol{k}}$ and $F_{\boldsymbol{k}}$ are 3×3 matrices. The matrix elements of E and F are defined by

$$\begin{cases} E_{11} = E_{22} = E_{33} = 4J_0(1 - \cos k_z) + 6J_1, \\ E_{12} = E_{21}^* = 3J_1[\cos(\theta_1 - \theta_2) + 1]\nu_{\boldsymbol{k}}, \\ E_{23} = E_{32}^* = 3J_1[\cos(\theta_2 - \theta_3) + 1]\nu_{\boldsymbol{k}}, \\ E_{31} = E_{13}^* = 3J_1[\cos(\theta_3 - \theta_1) + 1]\nu_{\boldsymbol{k}}, \end{cases} \tag{2.43}$$

$$\begin{cases} F_{11} = F_{22} = F_{33} = 0, \\ F_{12} = F_{21}^* = 3J_1[\cos(\theta_1 - \theta_2) - 1]\nu_{\boldsymbol{k}}, \\ F_{23} = F_{32}^* = 3J_1[\cos(\theta_2 - \theta_3) - 1]\nu_{\boldsymbol{k}}, \\ F_{31} = F_{13}^* = 3J_1[\cos(\theta_3 - \theta_1) - 1]\nu_{\boldsymbol{k}}, \end{cases} \tag{2.44}$$

where the complex quantity $\nu_{\boldsymbol{k}}$ is defined by

$$\nu_{\boldsymbol{k}} = \frac{1}{3}\left[\exp(ik_x) + \exp\left(i\frac{-k_x + \sqrt{3}k_y}{2}\right) + \exp\left(i\frac{-k_x - \sqrt{3}k_y}{2}\right)\right]. \tag{2.45}$$

Now the problem is to find the spin-wave Hamiltonian $\mathcal{H}_{\mathrm{SW}}$ in diagonal form:

$$\mathcal{H}_{\mathrm{SW}} = E_0 - (2J_0 + 3J_1)NS + \frac{S}{2}\sum_{l}\sum_{\boldsymbol{k}}{}'\omega_l(\boldsymbol{k})[\alpha_l^\dagger(\boldsymbol{k})\alpha_l(\boldsymbol{k}) + \alpha_l(-\boldsymbol{k})\alpha_l^\dagger(-\boldsymbol{k})], \tag{2.46}$$

where $a_l(\boldsymbol{k})$ and $\alpha_l(\boldsymbol{k})$ are connected through the generalized Bogoliubov transformation:

$$\begin{cases} a_l(\boldsymbol{k}) = \sum_{l'}[u_l^{(l')}(\boldsymbol{k})\alpha_{l'}(\boldsymbol{k}) + v_l^{(l')}(\boldsymbol{k})\alpha_{l'}^\dagger(-\boldsymbol{k})], \\ a_l^\dagger(-\boldsymbol{k}) = \sum_{l'}[u_l^{(l')}(\boldsymbol{k})\alpha_{l'}^\dagger(-\boldsymbol{k}) + v_l^{(l')}(\boldsymbol{k})\alpha_{l'}(\boldsymbol{k})]. \end{cases} \tag{2.47}$$

The coefficients u and v are determined from the following Bogoliubov equation:

$$\begin{cases} (E + F)(u^{(l)} + v^{(l)}) = \omega_l(u^{(l)} - v^{(l)}), \\ (E - F)(u^{(l)} - v^{(l)}) = \omega_l(u^{(l)} + v^{(l)}), \end{cases} \tag{2.48}$$

where u and v are three-component vectors

$$u^T = (u_1, u_2, u_3), \; v^T = (v_1, v_2, v_3). \tag{2.49}$$

The spin wave frequency $\omega_l(\boldsymbol{k})$ is given by the solution of

$$\det[(E - F)(E + F) - \omega^2] = 0. \tag{2.50}$$

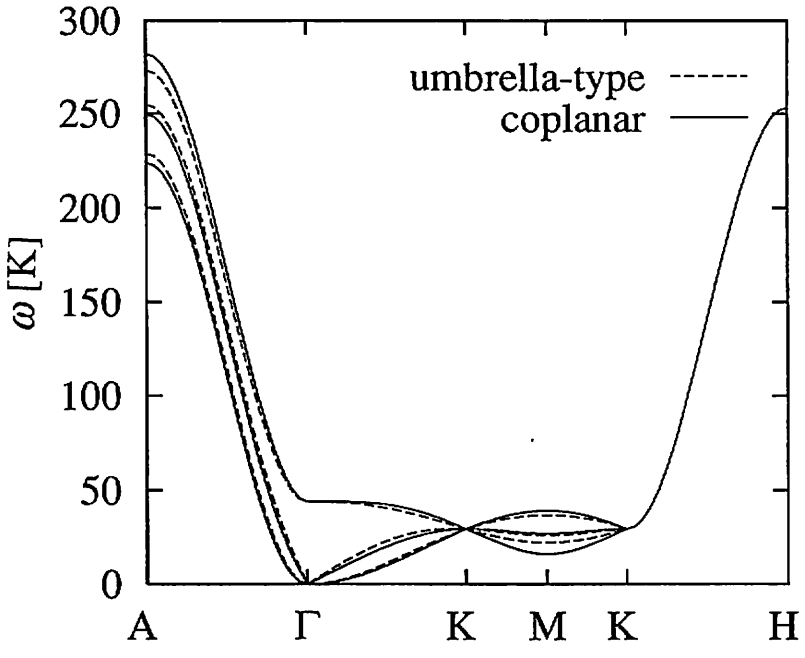

Figure 2.2: Calculated spin-wave spectrum at $h = 0.5$ for the umbrella-type configuration (a) and the coplanar configuration (c).

The 1/S quantum correction to the classical ground state energy is then given in the same form as Eq. (2.37).

Although it is difficult to write spin-wave frequencies $\omega_l(\boldsymbol{k})$ of the coplanar states in an explicit form for arbitrary wavevector $\boldsymbol{k}$ and for arbitrary h, the frequencies can be determined by solving (2.50) numerically. Figure 2.2 compares the spin-wave frequencies for the umbrella-type configuration of Fig. 2.1(a) and the coplanar configuration of Fig. 2.1(c). Here h is taken as 0.5; as evident from the figure, the lowest branch for the coplanar configuration is always lower than that for the umbrella-type configuration. This is the reason why quantum fluctuations stabilize the coplanar configuration more.

Using these spin-wave frequencies, we have evaluated the quantum correction for the four spin configurations in Fig. 2.1. We have used the following values for the parameters: $J_0 = 28$K, $J_1 = 4.9$K. These values are very close to what Tanaka *et al.* [22] used to interpret ESR data [23], and they are consistent with other previous experiments [17,18]. Figure 2.3 shows the results; quantum fluctuations appear to favor the coplanar configurations (b) for $h < 1/3$, and (c) for $h > 1/3$. As we can see in various theoretical models [3-6], quantum fluctuations stabilize most the collinear

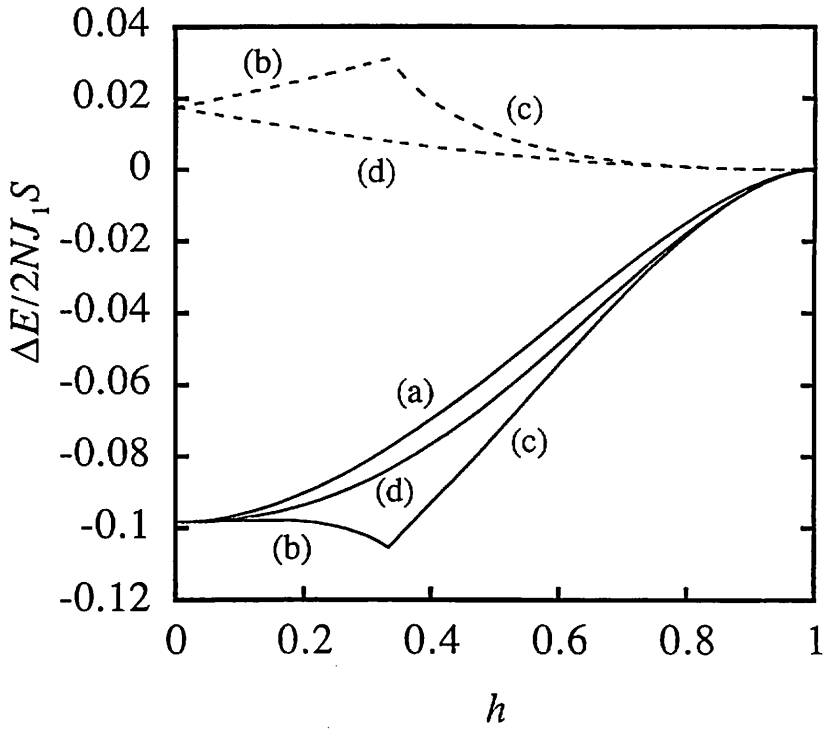

Figure 2.3: The $1/S$ correction to the ground-state energy for the four spin configurations in Fig. 2.1 as a function of the magnetic field. The intrachain coupling J_0 and interchain coupling J_1 are chosen as $J_0 = 28$K and $J_1 = 4.9$K. Δ is assumed to be 0. The broken line denotes the classical difference of the energy measured from the umbrella-type configuration, which is calculated with $\Delta = 0.07$.

spin configuration.

The broken line in Fig 2.3 shows the classical contribution from the anisotropy, which is calculated by taking $\Delta = 0.07$. Note that the quantum contribution favoring the coplanar configuration is in contrast with the classical contribution of Δ. Therefore, in the presence of the easy-plane anisotropy, there is a competition between the quantum contribution and the classical energy difference. In such cases the most stable spin structure must be determined by taking into account the anisotropy together with quantum fluctuations. The crudest approximation is to evaluate the total energy by simply adding the classical energy (linear in Δ) and the quantum correction (proportional to 1/S). Since Δ is small in $CsCuCl_3$, we take $\Delta = 0$ in evaluating the quantum contribution. Figure 2.4 shows the total ground-state energy, measured from the classical energy for the umbrella-type configuration. For $h < h_c = 0.36$, the energy of the umbrella-like configuration is clearly lower than that of the coplanar-type configurations. However, the coplanar configuration (c) has the lowest energy

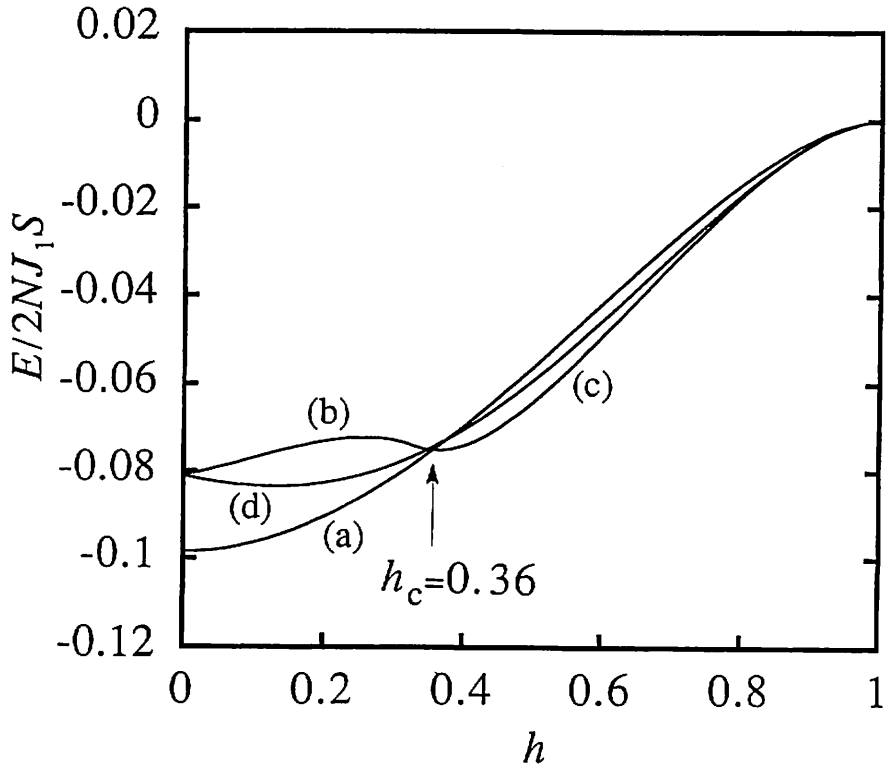

Figure 2.4: The total ground-state energy for the four spin configurations, which is the sum of the Δ-linear classical energy and the $1/S$ quantum correction shown in Fig. 2.1. Here E is measured from the classical energy for the umbrella-type configuration.

for $h > h_c$. Thus we expect the spin structure to change at h_c from the umbrella-type one in Fig. 2.1(a) to the coplanar structure in Fig. 2.1(c). This value of h_c is in reasonable agreement with the experimental result, $h_c = 0.4$ [10,11]. The magnitude of the magnetization jump at H_c is estimated in the classical approximation as

$$\Delta M = M_0 \Delta \frac{(1-h^4)}{36h^3}, \tag{2.51}$$

where $M_0 = g\mu_B S$ is the saturation magnetization. Substituting $h_c = 0.36$ and $\Delta = 0.07$ into (2.51), we obtain $\Delta M = 0.041 M_0$, which should be compared with the experimental value $\Delta M = 0.012 M_0$ [10,11]. At present we do not know whether this discrepancy is serious or not.

2.4 Thermal Fluctuations

At finite temperatures, thermal fluctuations also contribute to the breaking of the continuous degeneracy for $\Delta = 0$. This section discusses the effect of thermal fluctuations on the three-dimensional hexagonal antiferromagnet in a magnetic field at low temperatures. As noted in section 1.2, thermal fluctuations favor the coplanar configuration in the two-dimensional triangular antiferromagnet. The same physics can be expected to appear in three-dimensional systems such as $CsCuCl_3$. As done in evaluating the quantum contribution in section 2.2, we examine the effect of thermal fluctuations for $\Delta = 0$.

First we examine the effect of classical thermal fluctuations in the low-temperature limit by using the harmonic approximation. In this analysis, it is convenient to express the spin direction in terms of the azimuthal angle ϕ_{in} and the polar angle θ_{in}. The ground-state configuration is determined by minimizing the energy function $\mathcal{H}(\{\phi_{in}, \theta_{in}\})$. At finite temperatures, the spins deviate from their equilibrium configurations $\{\bar{\phi}_{in}, \bar{\theta}_{in}\}$ as $\{\phi_{in} = \bar{\phi}_{in} + x_{in},\ \theta_{in} = \bar{\theta}_{in} + y_{in}\}$. In the low-temperature limit, the Hamiltonian can be expanded in powers of $\{x_{in}, y_{in}\}$ to second order:

$$\mathcal{H} = E_0 + \mathcal{H}_2, \tag{2.52}$$

where $\mathcal{H}_2$ denotes the terms quadratic in $\{x_{in}, y_{in}\}$. The linear term disappears because we are expanding about the equilibrium configuration. Within this approximation, the free energy is calculated as

$$F = -T \ln \int \prod_{in} d\phi_{in} d\theta_{in} \sin\theta_{in} \exp\left(-\frac{\mathcal{H}}{T}\right),$$

$$= E_0 - T \ln \int \prod_{in} dx_{in} dy_{in} \sin\theta_{in} \exp\left(-\frac{\mathcal{H}_2}{T}\right). \tag{2.53}$$

Here the Boltzmann constant is taken to be unity. Since $\mathcal{H}_2$ is quadratic in x_{in} and y_{in}, it is possible to carry out the integration in (2.53). Let us now evaluate the free energy (2.53) for the umbrella configuration and coplanar configurations.

[I] umbrella-type configuration

The quadratic term in the expansion of the Hamiltonian is

$$\begin{aligned}\mathcal{H}_2 = S^2 \sum_{in} [(2J_0 + 3J_1)(x_{in}^2 + \tilde{y}_{in}^2) - 2J_0(x_{in}x_{in+1} + \tilde{y}_{in}\tilde{y}_{in+1}] \\ + J_1 S^2 \sum_{<ij>n} [(2 - 3h^2)x_{in}x_{jn} - \tilde{y}_{in}\tilde{y}_{jn} + \sqrt{3}h(x_{in}\tilde{y}_{jn} - \tilde{y}_{in}x_{jn}),\end{aligned} \tag{2.54}$$

where $\tilde{y}_{in} = y_{in}\sin\theta$. With the Fourier transformations

$$x_{in} = \sqrt{\frac{1}{N}} \sum_{\boldsymbol{k}} x_{\boldsymbol{k}} \exp(i\boldsymbol{k}\cdot\boldsymbol{r}_{in}),\ \tilde{y}_{in} = \sqrt{\frac{1}{N}} \sum_{\boldsymbol{k}} \tilde{y}_{\boldsymbol{k}} \exp(i\boldsymbol{k}\cdot\boldsymbol{r}_{in}), \tag{2.55}$$

of $x_{\boldsymbol{k}}$ and $\tilde{y}_{\boldsymbol{k}}$, we find

$$\mathcal{H}_2 = \frac{S^2}{2} \sum_{\boldsymbol{k}} [(A_{\boldsymbol{k}} + B_{\boldsymbol{k}})x_{-\boldsymbol{k}}x_{\boldsymbol{k}} + (A_{\boldsymbol{k}} - B_{\boldsymbol{k}})\tilde{y}_{-\boldsymbol{k}}\tilde{y}_{\boldsymbol{k}} + C_{\boldsymbol{k}}(\tilde{y}_{-\boldsymbol{k}}x_{\boldsymbol{k}} - x_{-\boldsymbol{k}}\tilde{y}_{\boldsymbol{k}})], \tag{2.56}$$

where $A_{\boldsymbol{k}}$, $B_{\boldsymbol{k}}$ and $C_{\boldsymbol{k}}$ are defined by Eqs. (2.28) and (2.29). Substituting the quadratic Hamiltonian (2.56) into (2.53), we obtain the free energy of the umbrella-type configuration as

$$\begin{aligned}F &= E_0 - T \ln \int \prod_{\boldsymbol{k}} dx_{\boldsymbol{k}} d\tilde{y}_{\boldsymbol{k}} \exp(-\frac{\mathcal{H}_2}{T}) \\ &= E_0 + NT \ln \frac{\pi}{T} + \frac{T}{2} \sum_{\boldsymbol{k}} \ln\det \frac{S^2}{2} \begin{pmatrix} A_{\boldsymbol{k}} + B_{\boldsymbol{k}} & C_{\boldsymbol{k}} \\ C_{\boldsymbol{k}} & A_{\boldsymbol{k}} - B_{\boldsymbol{k}} \end{pmatrix} \\ &= E_0 + NT \ln \frac{\pi S^2}{2T} + T \sum_{\boldsymbol{k}} \ln \omega_{\boldsymbol{k}}.\end{aligned} \tag{2.57}$$

We have used the relation $A_{\boldsymbol{k}}^2 - B_{\boldsymbol{k}}^2 - C_{\boldsymbol{k}}^2 = \omega_{\boldsymbol{k}}\omega_{-\boldsymbol{k}}$ in the derivation of (2.57).

[II] coplanar configurations

Next we apply the harmonic approximation to the coplanar configurations. The quadratic Hamiltonian for this case is given by

$$\begin{aligned}\mathcal{H}_2 = S^2 \sum_{in} [(2J_0 + 3J_1)(\tilde{x}_{in}^2 + y_{in}^2) - 2J_0(\tilde{x}_{in}\tilde{x}_{in+1} + y_{in}y_{in+1})] \\ + 3J_1 S^2 \sum_{<ij>n} [\tilde{x}_{in}\tilde{x}_{jn} + \cos(\theta_i - \theta_j)y_{in}y_{jn}],\end{aligned} \tag{2.58}$$

where $\tilde{x}_{in} = x_{in} \sin\theta_{in}$. We introduce the Fourier transformations of $\tilde{x}$ and y defined on each sublattice as

$$\tilde{x}_{in} = \sqrt{\frac{3}{N}} \sum_{\boldsymbol{k}}{}' \tilde{x}_{\boldsymbol{k}}^{(l)} \exp(i\boldsymbol{k} \cdot \boldsymbol{r}_{in}), \; y_{in} = \sqrt{\frac{3}{N}} \sum_{\boldsymbol{k}}{}' y_{\boldsymbol{k}}^{(l)} \exp(i\boldsymbol{k} \cdot \boldsymbol{r}_{in}). \tag{2.59}$$

Using $\tilde{x_{\boldsymbol{k}}}$ and $y_{\boldsymbol{k}}$ we have the following Hamiltonian in matrix form:

$$\mathcal{H} = \frac{S^2}{2} \sum_{\boldsymbol{k}}{}' [\tilde{\boldsymbol{x}}_{-\boldsymbol{k}}^T (E_{\boldsymbol{k}} - F_{\boldsymbol{k}}) \tilde{\boldsymbol{x}}_{\boldsymbol{k}} + \boldsymbol{y}_{-\boldsymbol{k}}^T (E_{\boldsymbol{k}} + F_{\boldsymbol{k}}) \boldsymbol{y}_{\boldsymbol{k}}], \tag{2.60}$$

where $\tilde{\boldsymbol{x}}$ and $\boldsymbol{y}$ are three-component vectors

$$\tilde{\boldsymbol{x}}^T = (\tilde{x}^{(1)}, \tilde{x}^{(2)}, \tilde{x}^{(3)}), \; \boldsymbol{y}^T = (y^{(1)}, y^{(2)}, y^{(3)}). \tag{2.61}$$

The matrix elements of E and F are defined by Eqs. (2.43) and (2.44). The free energy of the coplanar configurations in the harmonic approximation is then given by

$$F = E_0 + NT \ln \frac{\pi S^2}{2T} + \frac{T}{2} \sum_{\boldsymbol{k}}{}' [\ln \det(E_{\boldsymbol{k}} - F_{\boldsymbol{k}}) + \ln \det(E_{\boldsymbol{k}} + F_{\boldsymbol{k}})]. \tag{2.62}$$

Using the relation $\det(E - F)(E + F) = \omega_1^2 \omega_2^2 \omega_3^2$, we can express the free energy in the same form as for the umbrella-type configuration:

$$F = E_0 + NT \ln \frac{\pi S^2}{2T} + \frac{T}{2} \sum_{l} \sum_{\boldsymbol{k}}{}' \ln \omega_l(\boldsymbol{k}). \tag{2.63}$$

Actually the product of the squared eigenfrequencies can be obtained without solving the equation (2.50). Since the matrix $E - F$ is independent of the inplane spin arrangement, the dependence of the free energy on the spin configuration stems from $\det(E + F)$. One can easily see that the matrix $E + F$ coincides with Eq. (1.15) for $J_0 = 0$. Therefore the inplane-arrangement dependence of the free energy in the Heisenberg model is the same as in the plane-rotator (or XY) model. Thus we conclude that the most stable state among the many coplanar structure is that of Fig. 2.1(b) for $h < 1/3$ and that of (c) for $h > 1/3$.

Figure 2.5 is a plot of the spin-configuration-dependent factor in the free energy $\sum_{\boldsymbol{k},l} \ln \omega_l(\boldsymbol{k})$ as a function of the reduced magnetic field h. As evident from the figure, the entropy term favors the coplanar configuration more than the umbrella-type configuration. The free energy for the coplanar configuration has a sharp minimum at $h = 1/3$. The difference in the free energy between the lowest coplanar configuration

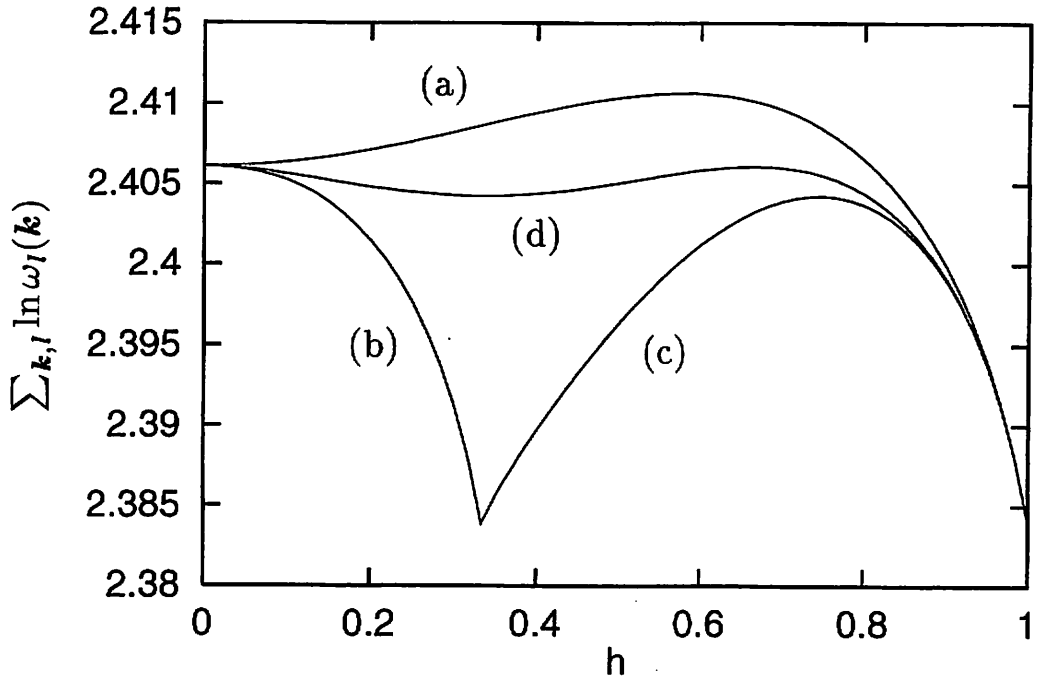

Figure 2.5: Plot of $\sum_{k,l} \ln \omega_l(k)$ for the four spin configurations as a function of the magnetic field.

and the umbrella-type configuration is at most about $0.012T$ (at $h = 1/3$); at low temperatures, it is much smaller than the difference in $\Delta E_{\rm SW}$ at the same field (estimated as about 0.14K).

Next we consider thermal fluctuations together with quantum fluctuations. The free energy is calculated from the following formula:

$$F = E_0 + \Delta E_{\rm SW} + T \sum_l \sum_{\boldsymbol{k}} \ln \left\{ 1 - \exp \left[-\frac{S\omega_l(\boldsymbol{k})}{T} \right] \right\}. \tag{2.64}$$

Figure 2.6 shows the resulting free energy for various temperatures. We see that the coplanar structure (b) or (c) is stabilized most by thermal fluctuations.

We have explicitly shown that thermal fluctuations at finite temperatures favor the same spin configurations as do the quantum fluctuations at $T = 0$. The collinear spin structure is particularly favored by thermal fluctuations. Therefore we expect the critical field H_c to decrease with increasing temperature; this is qualitatively consistent with the experimental phase diagram [11].

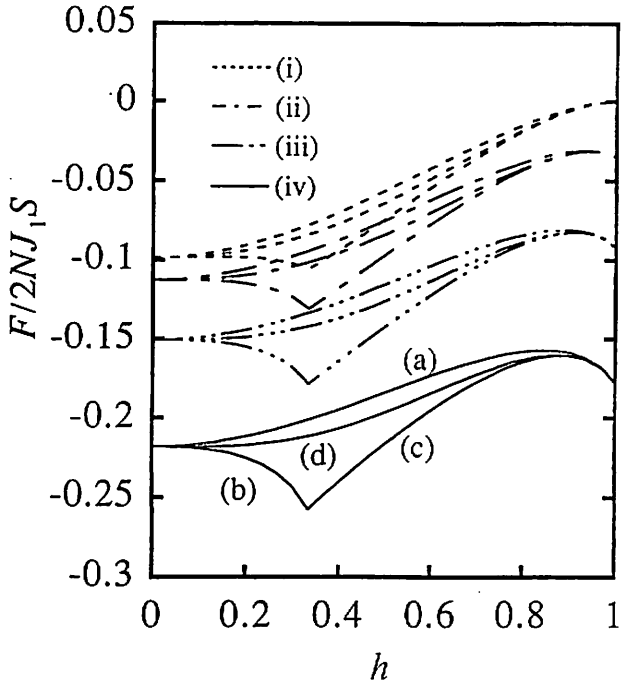

Figure 2.6: The free energy for the four spin configurations relative to the classical ground-state energy; (i) $T/2J_1S = 0$, (ii) $T/2J_1S = 1.0$, (iii) $T/2J_1S = 1.5$, (iv) $T/2J_1S = 2.0$.

2.5 Neutron-Scattering Experiment

An experimental check of our proposal has been carried out by Professor Motokawa's group, which uses the neutron scattering with a combination of pulsed neutrons and pulsed magnetic fields [24,25]. They observed the intensities of the magnetic reflections (1/3,1/3,δ) and (1/3,1/3,0) at fields from zero up to 14T. Measurements were done at 7K; at this temperature, the phase-transition field H_c is 10T. Figure 2.7 shows the field dependence of the reflection intensities [24].

First we examine the result for the (1/3,1/3,δ) reflection (Fig. 2.7(a)); the 3-sublattice structure of the c-plane magnetic component contributes to this reflection. Due to the helical modulation along the c-axis, the reflection point shifts to the c^*-axis in the reciprocal lattice by $\delta = 0.085$. In magnetic fields up to 14T, δ remains constant; this experimental result is consistent with that the antisymmetric exchange interaction causes the helical modulation along the c-axis. As shown in Fig. 2.7(a), the intensity decreases with increasing field, below the transition field H_c This is due to the decrease of the perpendicular component of the moments with increasing

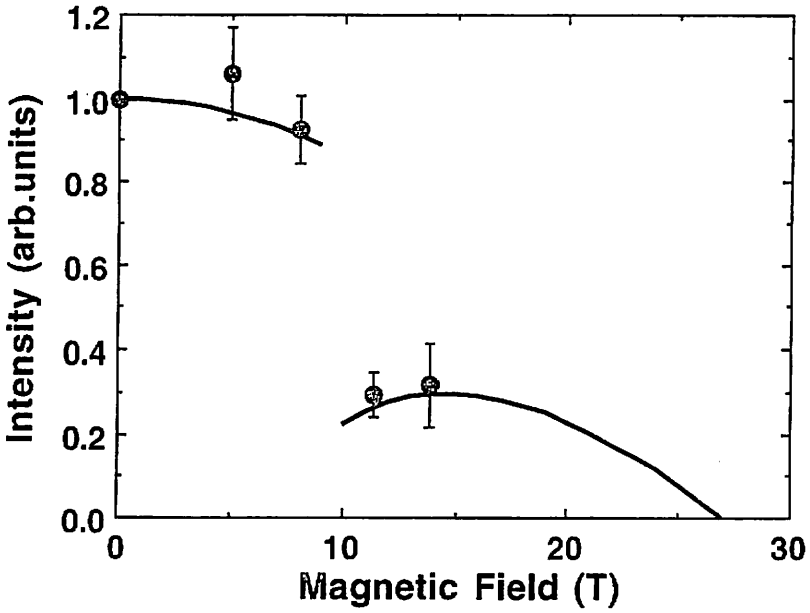

(a)

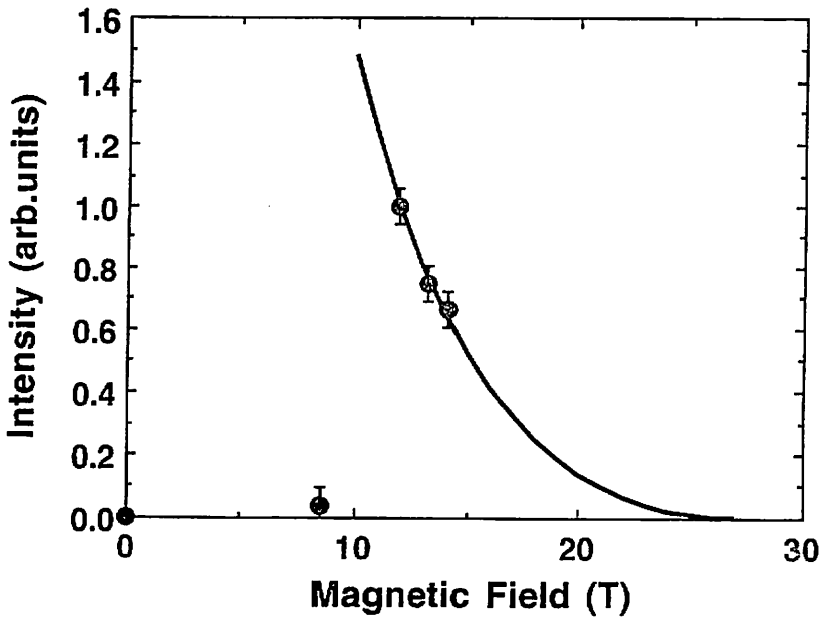

(b)

Figure 2.7: The magnetic-field dependences of the reflection intensities observed in the neutron-scattering experiment [24]: (a) (1/3,1/3,0.085) reflection and (b) (1/3,1/3,0) reflection. The solid lines are the calculation from the model.

field. The reflection intensity shows an abrupt decrease at H_c, which means an abrupt decrease of the perpendicular moment. The solid line in the figure is the intensity calculated assuming the coplanar structure in Fig. 2.1(c). We find very good agreement between experiment and the calculation.

Second we look at the result for the (1/3,1/3,0) reflection. The umbrella structure has no contribution at this reflection because of the helical modulation along the c-axis. However in the high-field coplanar structure which we propose, the c-component of the magnetic moment has a 3-lattice period in the c-plane and so it contributes to the (1/3,1/3,0) reflection. The solid line is a model calculation for the intensity; it is in good agreement with the experimental result.

These results are consistent with the proposed phase transition. Schotte *et al.* also performed a neutron-scattering experiment near T_N, and obtained results consistent with our proposed coplanar spin structure [26]. Ohta *et al.* performed submillimeter wave ESR measurement of $CsCuCl_3$ using pulsed magnetic fields up to 16T [27,28]. An abrupt change of the ESR mode was observed at the magnetic field which corresponds to the field where the magnetization jump occurs. Chiba *et al.* performed a ^{133}Cs NMR experiment on $CsCuCl_3$ [29,30]. They observed a discontinuity in the spectrum at the transition field H_c. The spectra above and below the transition field are compatible with our proposed spin structures.

2.6 Summary

We have shown that the small jump in the magnetization of $CsCuCl_3$ for a magnetic field applied parallel to the c-axis is likely to be due to a quantum-fluctuation-induced phase transition. The abrupt change of the magnetization is explained as a spin-flop transition from the umbrella-type configuration to the coplanar configuration; the transition is caused by quantum fluctuations. In fields lower than H_c, the umbrella-type structure is stabilized by the easy-plane anisotropy, while in fields higher than H_c, the coplanar configuration is stabilized by quantum fluctuations. There is then a competition between the easy-plane anisotropy (which favors the umbrella-type configuration) and quantum fluctuations (which favors the coplanar configuration). In most materials, the anisotropy energy dominates the quantum effect. However, the Cu^{2+} ion in $CsCuCl_3$ has $S = 1/2$ and the anisotropy appears to be very weak;

therefore quantum fluctuations can overcome the anisotropy in this material. At finite temperatures, thermal fluctuations favor more the coplanar configuration. The results of the neutron-scattering experiment up to 14T are consistent with the proposed phase transition [24,25]. The phase transition at H_c has also been observed clearly by ESR [27,28] and NMR [29,30].

Let us comment on a different theoretical interpretation for the anomaly in the magnetization. Fedoseeva *et al.* [20,31] suggested that the transition at H_c is caused by the dipole-dipole interaction which leads to an incommensurate magnetic structure with a long-wavelength modulation. However, as shown in Ref. 32, the dipole-dipole interaction can cause an incommensurate state only near the Néel temperature. It seems, therefore, that their theory cannot explain the transition at low temperatures.

Although the present study has been supported by experiments, there is left an important problem from the theoretical point of view. In the present study, we took $\Delta = 0$ in the calculation of the quantum contribution and used the classical energy difference for the contribution of Δ. In other words, we retained terms only to lowest order in both Δ and $1/S$. This is because the spin-wave calculation together in the presence of the easy-plane anisotropy can be applied only to the umbrella-type spin structure (which is the classically stable structure for $\Delta > 0$). A more improved treatment, taking into account the quantum effect for $\Delta > 0$, is presented in the next chapter.

Chapter 3

Ground-State Spin Structure in Strong Magnetic Field

This chapter investigates the ground-state spin structure in the high-field region (near saturation) by using a mapping onto the low-density Bose gas. The contents were published in Ref. 33 as "Hexagonal Antiferromagnets in Strong Magnetic Field: Mapping onto Bose Condensation of Low-Density Bose Gas."

3.1 Introduction

Spin-wave theory is usually a useful method to include quantum fluctuations in the theory of ordered spin systems; explicitly, one finds the $1/S$ quantum correction to physical quantities such as the ground-state energy and the sublattice magnetization. However standard spin-wave theory has a difficulty in solving a problem such as $CsCuCl_3$ in a magnetic field applied parallel to the c-axis. We have shown in the previous chapter that the classical ground state of $CsCuCl_3$ in $H||c$ is the umbrella-type spin structure; this is because of the small easy-plane anisotropy (with coefficient Δ). On the other hand, if $\Delta = 0$, the coplanar structure is selected by quantum fluctuations. In order to determine the ground-state spin structure in the quantum theory for $\Delta > 0$, we have to take into account these two opposing effects, quantum fluctuations and the anisotropy, simultaneously. However spin-wave theory for $\Delta > 0$ can be applied only to the umbrella-type structure. Other types of spin structure are unstable classically, and thus cannot be treated by the standard procedure of the $1/S$ expansion. For this reason, we have taken $\Delta = 0$ in the spin-wave calculation in chapter 2.

In this chapter we apply a complementary approach which can avoid the difficulty mentioned above. This approach is based on the exact hard-core-boson representation of $S = 1/2$ spins. We focus our attention on the case of strong magnetic field slightly below the saturation field. The spin-ordering problem near saturation is mapped onto an equivalent Bose-condensation problem in the low-density limit [36-38]. Then the low-density expansion for interacting bosons [39] is applied to determine the ground-state spin structure. In contrast to the $1/S$ expansion, this approach has the following advantages:

(1) We do not need to assume particular spin structures; instead we can directly find the most stable state.
(2) The difference of the magnetic field from the saturation field provides a small expansion parameter for the theory, so we can include the quantum effect in the calculation completely.

From this study we determine the ground state spin structure near the saturation field.

This chapter is arranged as follows. In section 3.2 we introduce the transformation from the spin operators to the bosons and derive an equivalent Bose Hamiltonian. In section 3.3 the low-density expansion is applied to determine the ground-state spin structure. A calculation for $CsCuCl_3$ is performed by using reasonable values of the parameters. In section 4, the present approach is extended to the case of arbitrary spin S. Section 5 summarizes the results of this chapter.

3.2 Bose-Gas Representation for the Spin Hamiltonian

In this chapter we consider the following general form of the Hamiltonian which describes a hexagonal antiferromagnet in a magnetic field:

$$\begin{aligned}\mathcal{H} = & -2\sum_{\langle ij\rangle}[J_0^{\perp}(S_i^x S_j^x + S_i^y S_j^y) + J_0^{\parallel} S_i^z S_j^z] \\ & +2\sum_{\langle ij\rangle}[J_1^{\perp}(S_i^x S_j^x + S_i^y S_j^y) + J_1^{\parallel} S_i^z S_j^z] \\ & -H\sum_i S_i^z,\end{aligned} \tag{3.1}$$

where S_i^x, S_i^y and S_i^z represent the components of the spin operator (with $S = 1/2$) at the site i. The summations $\langle ij \rangle$ in the first and second terms are taken over all nearest neighbor pairs in the chain and in the c-plane, respectively. The interchain interaction is assumed to be antiferromagnetic: $J_1^\perp > 0, J_1^\parallel > 0$. We assume that $J_0^\perp$ is positive, having the case of ferromagnetic chains such as $CsCuCl_3$ in mind. The case of antiferromagnetic chains can be also treated within this model by rotating the xy component of the spins along the c-chain so that $J_0^\perp$ is positive. In this case the S^z part of the intrachain interaction is transformed as $J_0^\parallel \to -J_0^\parallel$.

We represent the spin operators (with $S = 1/2$) by Bose operators using the following transformation:

$$S_i^z = \frac{1}{2} - a_i^\dagger a_i, \;\; S_i^+ = (1 - a_i^\dagger a_i) a_i, \;\; S_i^- = a_i^\dagger (1 - a_i^\dagger a_i). \tag{3.2}$$

The state with $S_i^z = 1/2$ or $S_i^z = -1/2$ corresponds to $n_i = 0$ or 1 at the site i, where n_i is the particle number. It is easy to confirm that the transformation is valid for $S = 1/2$ spins within the subspace where $n_i = 0$ or 1. Substituting (3.2) into the Hamiltonian (3.1), we obtain a Bose-gas Hamiltonian with nearest-neighbor hopping and nearest-neighbor interaction. Since the matrix element of $(1 - a_i^\dagger a_i) a_i$ is equal to the matrix element of a_i within the subspace $n_i = 0, 1$, we can neglect the factor $1 - a_i^\dagger a_i$ in the substitution within this subspace. In the momentum-space representation, the boson Hamiltonian is written in a standard form:

$$\mathcal{H} = \sum_{\boldsymbol{k}} (\varepsilon_{\boldsymbol{k}} - \mu) a_{\boldsymbol{k}}^\dagger a_{\boldsymbol{k}} + \frac{1}{2N} \sum_{\boldsymbol{k}, \boldsymbol{k}', \boldsymbol{q}} V_{\boldsymbol{q}} a_{\boldsymbol{k}+\boldsymbol{q}}^\dagger a_{\boldsymbol{k}'-\boldsymbol{q}}^\dagger a_{\boldsymbol{k}'} a_{\boldsymbol{k}}, \tag{3.3}$$

where N is number of lattice sites and

$$\varepsilon_{\boldsymbol{k}} = 2J_0^\perp (1 - \cos k_z) + 3J_1^\perp (1 + 2\gamma_{\boldsymbol{k}}), \tag{3.4}$$

$$\gamma_{\boldsymbol{k}} = \frac{1}{3} \left(\cos k_x + \cos \frac{k_x + \sqrt{3} k_y}{2} + \cos \frac{k_x - \sqrt{3} k_y}{2} \right), \tag{3.5}$$

$$\mu = H_c - H, \quad H_c = 2(J_0^\perp - J_0^\parallel) + 3J_1^\perp + 6J_1^\parallel, \tag{3.6}$$

$$V_{\boldsymbol{q}} = V_{\boldsymbol{q}}^\parallel + U \equiv -4J_0^\parallel \cos q_z + 12 J_1^\parallel \gamma_{\boldsymbol{q}} + U. \tag{3.7}$$

We have introduced the hard-core interaction U in order to satisfy the constraint $n_i = 0$ or 1 ; we must take the limit $U \to \infty$. A remarkable feature of this boson system is that the minima of the single-particle energy $\varepsilon_{\boldsymbol{k}}$ are located at the two states

$\boldsymbol{k} = \pm\boldsymbol{Q}$ where $\boldsymbol{Q} = (4\pi/3, 0, 0)$: $\varepsilon_{\pm\boldsymbol{Q}} = 0$. Since no reciprocal lattice vector of the triangular lattice connects $\boldsymbol{Q}$ and $-\boldsymbol{Q}$, they should be considered as independent. If $\mu < 0$, the ground state is the vacuum of Bose particles. This means that the spins are completely aligned along the field direction when $H > H_c$. Here we are interested in the case of a small positive μ ($(H_c - H)/H_c \ll 1$), which corresponds to the low-density limit. In conventional (three-dimensional) Bose systems, it is well known that the Bose condensation occurs at low temperatures; a macroscopic number of particles occupy the lowest single-particle level. On the other hand, our model has two lowest states $\boldsymbol{k} = \pm\boldsymbol{Q}$; thus we expect two-component Bose condensation to occur at low temperatures. This is equivalent to spin ordering with the 3-sublattice structure. The ground state has to be determined by minimizing the interaction energy of the condensate particles. To discuss this type of problem, Beliaev [39] applied the quantum-field-theoretical method to conventional systems in the low-density limit. We extend his method to the two-component Bose condensation.

To treat the Bose condensation by the standard diagrammatical technique, we introduce the following (complex) order parameters:

$$\langle a_{\boldsymbol{Q}} \rangle = \sqrt{N}\psi_{\boldsymbol{Q}}, \quad \langle a_{-\boldsymbol{Q}} \rangle = \sqrt{N}\psi_{-\boldsymbol{Q}}. \tag{3.8}$$

The existence of the order parameters (3.8) is equivalent to the long-range order of the xy component of the spins. Then the following shift transformation

$$a_{\boldsymbol{Q}} \to a_{\boldsymbol{Q}} + \sqrt{N}\psi_{\boldsymbol{Q}}, \quad a_{-\boldsymbol{Q}} \to a_{-\boldsymbol{Q}} + \sqrt{N}\psi_{-\boldsymbol{Q}}, \tag{3.9}$$

is substituted into (3.3). The resulting Hamiltonian is

$$\mathcal{H} = E_0 + \mathcal{H}_1 + \mathcal{H}_2 + \mathcal{H}_3 + \mathcal{H}_4, \tag{3.10}$$

where

$$E_0 = N[-\mu(|\psi_{\boldsymbol{Q}}|^2 + |\psi_{-\boldsymbol{Q}}|^2) + \frac{1}{2}V_0(|\psi_{\boldsymbol{Q}}|^4 + |\psi_{-\boldsymbol{Q}}|^4) + (V_0 + V_{\boldsymbol{Q}})|\psi_{\boldsymbol{Q}}|^2|\psi_{-\boldsymbol{Q}}|^2], \tag{3.11}$$

$$\begin{aligned} \mathcal{H}_1 = \sqrt{N}\{&[-\mu + V_0|\psi_{\boldsymbol{Q}}|^2 + (V_0 + V_{\boldsymbol{Q}})|\psi_{-\boldsymbol{Q}}|^2]\psi^*_{\boldsymbol{Q}} a_{\boldsymbol{Q}} \\ &+[-\mu + V_0|\psi_{-\boldsymbol{Q}}|^2 + (V_0 + V_{\boldsymbol{Q}})|\psi_{\boldsymbol{Q}}|^2]\psi^*_{-\boldsymbol{Q}} a_{-\boldsymbol{Q}} \\ &+(\psi^{*2}_{\boldsymbol{Q}}\psi_{-\boldsymbol{Q}} + \psi^{*2}_{-\boldsymbol{Q}}\psi_{\boldsymbol{Q}})V_{\boldsymbol{Q}} a_0 + \text{H.c.}\}, \end{aligned} \tag{3.12}$$

$$\mathcal{H}_2 = \sum_{\boldsymbol{k}}\{[\varepsilon_{\boldsymbol{k}} - \mu + (V_0 + V_{\boldsymbol{k}-\boldsymbol{Q}})|\psi_{\boldsymbol{Q}}|^2 + (V_0 + V_{\boldsymbol{k}+\boldsymbol{Q}})|\psi_{-\boldsymbol{Q}}|^2]a_{\boldsymbol{k}}^\dagger a_{\boldsymbol{k}}$$
$$+(V_{\boldsymbol{Q}} + V_{\boldsymbol{k}-\boldsymbol{Q}})(\psi_{\boldsymbol{Q}}^*\psi_{-\boldsymbol{Q}}a_{\boldsymbol{k}+\boldsymbol{Q}}^\dagger a_{\boldsymbol{k}} + \psi_{-\boldsymbol{Q}}^*\psi_{\boldsymbol{Q}}a_{\boldsymbol{k}}^\dagger a_{\boldsymbol{k}+\boldsymbol{Q}})$$
$$+\frac{1}{2}(V_{\boldsymbol{k}+\boldsymbol{Q}} + V_{\boldsymbol{k}-\boldsymbol{Q}})(\psi_{\boldsymbol{Q}}^*\psi_{-\boldsymbol{Q}}^* a_{\boldsymbol{k}}a_{-\boldsymbol{k}} + \psi_{\boldsymbol{Q}}\psi_{-\boldsymbol{Q}}a_{\boldsymbol{k}}a_{-\boldsymbol{k}})$$
$$+\frac{1}{2}V_{\boldsymbol{k}-\boldsymbol{Q}}(\psi_{\boldsymbol{Q}}^{*2}a_{\boldsymbol{k}}a_{-\boldsymbol{k}-\boldsymbol{Q}} + \psi_{\boldsymbol{Q}}^2 a_{\boldsymbol{k}}^\dagger a_{-\boldsymbol{k}-\boldsymbol{Q}}^\dagger)$$
$$+\frac{1}{2}V_{\boldsymbol{k}+\boldsymbol{Q}}(\psi_{-\boldsymbol{Q}}^{*2}a_{\boldsymbol{k}}a_{-\boldsymbol{k}+\boldsymbol{Q}} + \psi_{-\boldsymbol{Q}}^2 a_{\boldsymbol{k}}^\dagger a_{-\boldsymbol{k}+\boldsymbol{Q}}^\dagger)\}, \tag{3.13}$$

$$\mathcal{H}_3 = \frac{1}{\sqrt{N}}\sum_{\boldsymbol{k},\boldsymbol{k}'}[V_{\boldsymbol{k}-\boldsymbol{Q}}(\psi_{\boldsymbol{Q}}^* a_{\boldsymbol{k}+\boldsymbol{k}'-\boldsymbol{Q}}^\dagger a_{\boldsymbol{k}}a_{\boldsymbol{k}'} + \psi_{\boldsymbol{Q}}a_{\boldsymbol{k}}^\dagger a_{\boldsymbol{k}'}^\dagger a_{\boldsymbol{k}+\boldsymbol{k}'-\boldsymbol{Q}})$$
$$+V_{\boldsymbol{k}+\boldsymbol{Q}}(\psi_{-\boldsymbol{Q}}^* a_{\boldsymbol{k}+\boldsymbol{k}'+\boldsymbol{Q}}^\dagger a_{\boldsymbol{k}}a_{\boldsymbol{k}'} + \psi_{-\boldsymbol{Q}}a_{\boldsymbol{k}}^\dagger a_{\boldsymbol{k}'}^\dagger a_{\boldsymbol{k}+\boldsymbol{k}'+\boldsymbol{Q}})], \tag{3.14}$$

$$\mathcal{H}_4 = \frac{1}{2N}\sum_{\boldsymbol{k},\boldsymbol{k}',\boldsymbol{q}} V_{\boldsymbol{q}}a_{\boldsymbol{k}+\boldsymbol{q}}^\dagger a_{\boldsymbol{k}'-\boldsymbol{q}}^\dagger a_{\boldsymbol{k}'}a_{\boldsymbol{k}}. \tag{3.15}$$

The quadratic term $\sum_{\boldsymbol{k}}(\varepsilon_{\boldsymbol{k}} - \mu)a_{\boldsymbol{k}}^\dagger a_{\boldsymbol{k}}$ is the free Hamiltonian of the theory; the vacuum of the $a_{\boldsymbol{k}}$ is the noninteracting ground state. Let us define the $T = 0$ Green function as

$$G(\boldsymbol{k},\omega) = -i\int_{-\infty}^{\infty} dt e^{i\omega t}\langle T[a_{\boldsymbol{k}}(t)a_{\boldsymbol{k}}^\dagger]\rangle, \tag{3.16}$$

where

$$a_{\boldsymbol{k}}(t) = e^{i\mathcal{H}t}a_{\boldsymbol{k}}e^{-i\mathcal{H}t}, \tag{3.17}$$

and T means taking the time-ordered product. The noninteracting Green function is given by

$$G^{(0)}(\boldsymbol{k},\omega) = (\omega - \varepsilon_{\boldsymbol{k}} + \mu + i\eta)^{-1}. \tag{3.18}$$

Then we can apply the same diagrammatical technique as in conventional interacting boson systems [39-41].

3.3 Low-Density Expansion

In this section we determine the ground state of the Hamiltonian (3.3) in the low density limit and calculate the ground-state energy $E = \langle\mathcal{H}\rangle$. The amplitudes of the Bose condensates $|\psi_{\boldsymbol{Q}}|$ and $|\psi_{-\boldsymbol{Q}}|$ are expected to be small in the low-density limit. Thus we expand the ground-state energy in terms of the order parameters:

$$\frac{E}{N} = -\mu(|\psi_{\boldsymbol{Q}}|^2 + |\psi_{-\boldsymbol{Q}}|^2) + \frac{1}{2}\Gamma_1(|\psi_{\boldsymbol{Q}}|^4 + |\psi_{-\boldsymbol{Q}}|^4) + \Gamma_2|\psi_{\boldsymbol{Q}}|^2|\psi_{-\boldsymbol{Q}}|^2, \tag{3.19}$$

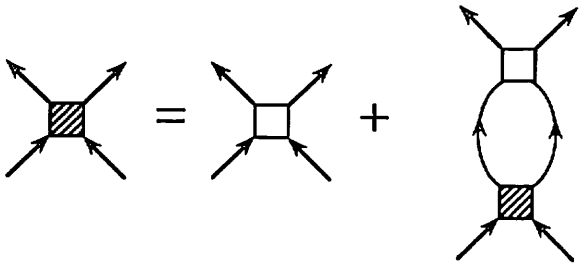

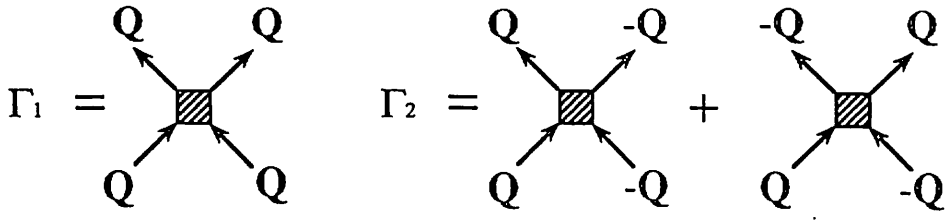

Figure 3.1: Diagrams for Γ_1 and Γ_2. The solid line represents the unperturbed Green function $G^{(0)}(\boldsymbol{k},\omega)$ and the open square represents the bare interaction $V_{\boldsymbol{q}}$.

where Γ_1 and Γ_2 are given by the ladder diagrams shown in Fig. 3.1. We can interpret Γ_1 and Γ_2 as effective potentials between two particles in the same state and in different states, respectively. Since we are concerned with the small-μ limit, we take $\mu = 0$ in the zeroth-order Green function in the diagram. Integrating over the intermediate frequency and setting the total frequency to zero, we obtain the integral equation for the effective potential as

$$\Gamma(\boldsymbol{q};\boldsymbol{k},\boldsymbol{k}') = V_{\boldsymbol{q}} - \frac{1}{N}\sum_{\boldsymbol{q}'}\frac{V_{\boldsymbol{q}-\boldsymbol{q}'}}{\varepsilon_{\boldsymbol{k}+\boldsymbol{q}'}+\varepsilon_{\boldsymbol{k}'-\boldsymbol{q}'}}\Gamma(\boldsymbol{q}';\boldsymbol{k},\boldsymbol{k}'). \tag{3.20}$$

Γ_1 and Γ_2 are related to $\Gamma(\boldsymbol{q};\boldsymbol{k},\boldsymbol{k}')$ via

$$\Gamma_1 = \Gamma(0;\boldsymbol{Q},\boldsymbol{Q}), \quad \Gamma_2 = \Gamma(0;\boldsymbol{Q},-\boldsymbol{Q}) + \Gamma(\boldsymbol{Q};\boldsymbol{Q},-\boldsymbol{Q}). \tag{3.21}$$

The ground state is determined by minimizing the energy (3.19). We find the following two types of ground state depending on the parameters Γ_1 and Γ_2:

(1) $\Gamma_1 < \Gamma_2$

$$|\psi_{\boldsymbol{Q}}|^2 = \frac{\mu}{\Gamma_1}, \ \psi_{-\boldsymbol{Q}} = 0 \text{ (or vice versa)}, \quad \frac{E}{N} = -\frac{\mu^2}{\Gamma_1}; \tag{3.22}$$

(2) $\Gamma_1 > \Gamma_2$

$$|\psi_{-\boldsymbol{Q}}|^2 = |\psi_{\boldsymbol{Q}}|^2 = \frac{\mu}{\Gamma_1+\Gamma_2}, \quad \frac{E}{N} = -\frac{\mu^2}{\Gamma_1+\Gamma_2}. \tag{3.23}$$

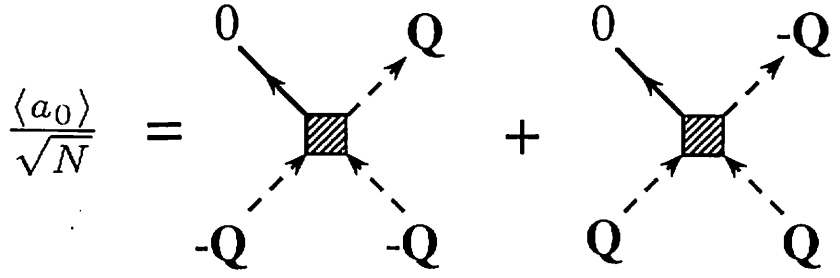

Figure 3.2: Diagrams for $\langle a_0 \rangle$. The incoming broken lines represent the condensate states $\psi_{\boldsymbol{Q}}$ and $\psi_{-\boldsymbol{Q}}$. The outgoing broken lines represent $\psi^*_{\boldsymbol{Q}}$ and $\psi^*_{-\boldsymbol{Q}}$.

The condition that the energy be a minimum is equivalent to the self-consistency equation $\langle a_{\boldsymbol{Q}} \rangle = \langle a_{-\boldsymbol{Q}} \rangle = 0$. However $\langle a_0 \rangle$ can have a nonzero value because the state $\boldsymbol{k} = 0$ is connected to $\pm\boldsymbol{Q}$ through $\mathcal{H}_1$. Figure 3.2 shows the diagrams for $\langle a_0 \rangle$; the analytical expression is

$$\frac{\langle a_0 \rangle}{\sqrt{N}} = -\frac{\Gamma_0}{\varepsilon_0}(\psi^*_{-\boldsymbol{Q}}\psi^2_{\boldsymbol{Q}} + \psi^*_{\boldsymbol{Q}}\psi^2_{-\boldsymbol{Q}}), \tag{3.24}$$

where $\Gamma_0 = \Gamma(\boldsymbol{Q}; \boldsymbol{Q}, \boldsymbol{Q})$ and $\varepsilon_0 = 9J_1^{\perp}$.

The spin structure corresponding to case (1) is expressed by the following:

$$\begin{aligned} \langle S_i^x \rangle &= \sqrt{\frac{H_c - H}{\Gamma_1}} \cos(\boldsymbol{Q} \cdot \boldsymbol{r}_i + \alpha), \\ \langle S_i^y \rangle &= \pm\sqrt{\frac{H_c - H}{\Gamma_1}} \sin(\boldsymbol{Q} \cdot \boldsymbol{r}_i + \alpha), \\ \langle S_i^z \rangle &= \frac{1}{2} - \frac{H_c - H}{\Gamma_1}, \end{aligned} \tag{3.25}$$

where α is an arbitrary phase. The quantity $\boldsymbol{Q} \cdot \boldsymbol{r}_i$ takes the values $0, 2\pi/3, 4\pi/3$ on the three sublattices of the triangular lattice. This is the umbrella-type spin structure shown in Fig. 3.3(a); the xy components of the spins form the 120° structure.

The spin structure corresponding to case (2) is

$$\begin{aligned} \langle S_i^x \rangle &= 2\sqrt{\frac{H_c - H}{\Gamma_1 + \Gamma_2}} \cos\left(\boldsymbol{Q} \cdot \boldsymbol{r}_i + \frac{\phi}{2}\right) \cos\frac{\theta}{2}, \\ \langle S_i^y \rangle &= 2\sqrt{\frac{H_c - H}{\Gamma_1 + \Gamma_2}} \cos\left(\boldsymbol{Q} \cdot \boldsymbol{r}_i + \frac{\phi}{2}\right) \sin\frac{\theta}{2}, \\ \langle S_i^z \rangle &= \frac{1}{2} - 4\left(\frac{H_c - H}{\Gamma_1 + \Gamma_2}\right) \cos^2\left(\boldsymbol{Q} \cdot \boldsymbol{r}_i + \frac{\phi}{2}\right), \end{aligned} \tag{3.26}$$

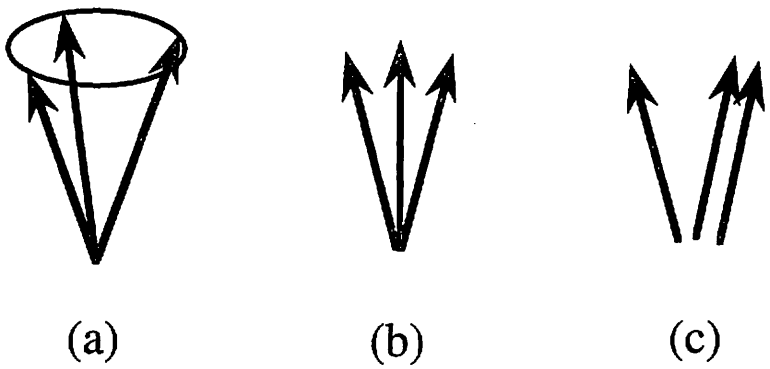

Figure 3.3: Three candidates for the ground state spin structure in the high field region. (a) the umbrella type structure: The c-plane components of the spins form the 120° structure. (b) a coplanar structure: One of the three spins is aligned along the field direction. (c) a coplanar structure. Two of the three spins are aligned along the same direction.

where $\psi_{\boldsymbol{Q}} = \psi e^{i\alpha_1}$, $\psi_{-\boldsymbol{Q}} = \psi e^{i\alpha_2}$, $\phi = \alpha_1 - \alpha_2$, and $\theta = \alpha_1 + \alpha_2$. In this case the transverse magnetization component $\langle S_i^x \rangle$ and $\langle S_i^y \rangle$ have an additional uniform component coming from $\langle a_0 \rangle$:

$$\begin{aligned} \langle S^x \rangle &= -\frac{2}{9J_0^\perp}\Gamma_0 \left(\frac{H_c - H}{\Gamma_1 + \Gamma_2}\right)^{3/2} \cos\frac{3\phi}{2}\cos\frac{\theta}{2}, \\ \langle S^y \rangle &= -\frac{2}{9J_0^\perp}\Gamma_0 \left(\frac{H_c - H}{\Gamma_1 + \Gamma_2}\right)^{3/2} \cos\frac{3\phi}{2}\sin\frac{\theta}{2}. \end{aligned} \tag{3.27}$$

The uniform component is of order $(H_c - H)^{3/2}$ and small. One can directly see from the integral equation (3.20) that Γ_0 vanishes for the isotropic exchange interaction. There is thus no uniform component in isotropic systems, as expected physically. The state expressed by (3.26) (and (3.27)) is a coplanar structure in which all spins lie in the same plane (which includes the z-axis). The total phase θ determines the plane while the relative phase ϕ determines the inplane spin arrangement. As shown in Eq. (3.19), the energy expression to fourth order in $\psi_{\boldsymbol{Q}}$ and $\psi_{-\boldsymbol{Q}}$ is degenerate with respect to the relative phase ϕ. This degeneracy is lifted by taking into account higher-order terms (which depend on ϕ):

$$\frac{E_\phi}{N} = \Gamma_3(\psi_{\boldsymbol{Q}}^{*3}\psi_{-\boldsymbol{Q}}^3 + \psi_{-\boldsymbol{Q}}^{*3}\psi_{\boldsymbol{Q}}^3) = 2\Gamma_3\psi^6\cos 3\phi, \tag{3.28}$$

where Γ_3 is expressed by the diagrams shown in Fig. 3.4. The phase ϕ is determined according to the sign of Γ_3:

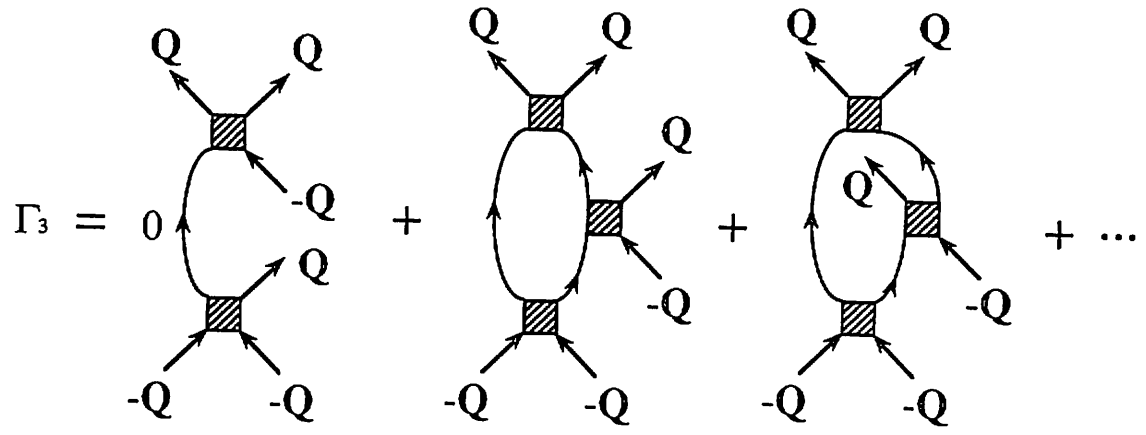

Figure 3.4: Diagrams for Γ_3.

(i) $\Gamma_3 > 0$: $\phi = \pi/3,\ \pi,\ 5\pi/3$ (see Fig. 3.3(b)),

(ii) $\Gamma_3 < 0$: $\phi = 0,\ 2\pi/3,\ 4\pi/3$ (see Fig. 3.3(c)).

The three-fold degeneracy is connected with interchanges among the 3 sublattices. One can see from (3.28) that the spin structure in Fig. 3.3(b) has no transverse component in the uniform magnetization, while the structure in 3.3(c) has a finite transverse magnetization.

In chapter 2 we examined three candidates, shown in Fig. 3.3 , for the ground-state spin structures in the high-field region, and compared their energies. We have shown here that these are the only possible candidates for the ground state as far as the high-field region slightly below the saturation field is concerned. The ground state is selected from among the three structures depending on the three quantities Γ_1, Γ_2 and Γ_3.

Let us now calculate Γ_1 and Γ_2 by solving the integral equation (3.20). In the limit $U \to \infty$, the equation (3.20) can be reduced to the following form:

$$\Gamma(q) = V_q^{\parallel} + \langle\Gamma\rangle - \frac{1}{N}\sum_{q'} \frac{V_{q-q'}^{\parallel}}{\varepsilon_{k+q'} + \varepsilon_{k'-q'}}\Gamma(q'),$$

$$\frac{1}{N}\sum_{q} \frac{\Gamma(q)}{\varepsilon_{k+q} + \varepsilon_{k'-q}} = 1. \tag{3.29}$$

The variables k and k' are omitted in the above expressions for simplicity. Let us solve equation (3.29) for the two cases: (1) $k_1 = k_2 = Q$ and (2) $k_1 = -k_2 = Q$.

(1) $k_1 = k_2 = Q$

We use the following *Ansatz* for the solution of Eq. (3.29):

$$\Gamma(\boldsymbol{q}) = \langle\Gamma\rangle - 4J_0^{\parallel}A_1\cos q_z + 12J_1^{\parallel}A_2\gamma_{\boldsymbol{q}}. \tag{3.30}$$

Substitution of the expression (3.30) into Eq. (3.29) gives the following equation for $\langle\Gamma\rangle$, A_1, and A_2:

$$\begin{pmatrix} \tau_0 & -4J_0^{\parallel}\tau_1 & 12J_1^{\parallel}\tau_2 \\ \tau_1 & -4J_0^{\parallel}\tau_3 + 1 & 12J_1^{\parallel}\tau_4 \\ \tau_2 & -4J_0^{\parallel}\tau_4 & 12J_1^{\parallel}\tau_5 + 1 \end{pmatrix} \begin{pmatrix} \langle\Gamma\rangle \\ A_1 \\ A_2 \end{pmatrix} = \begin{pmatrix} 1 \\ 1 \\ 1 \end{pmatrix}, \tag{3.31}$$

where

$$\begin{aligned} \tau_0 &= \frac{1}{N}\sum_{\boldsymbol{q}} \frac{1}{\varepsilon_{\boldsymbol{k}+\boldsymbol{q}} + \varepsilon_{\boldsymbol{k}'-\boldsymbol{q}}}, & \tau_1 &= \frac{1}{N}\sum_{\boldsymbol{q}} \frac{\cos q_z}{\varepsilon_{\boldsymbol{k}+\boldsymbol{q}} + \varepsilon_{\boldsymbol{k}'-\boldsymbol{q}}}, \\ \tau_2 &= \frac{1}{N}\sum_{\boldsymbol{q}} \frac{\gamma_{\boldsymbol{q}}}{\varepsilon_{\boldsymbol{k}+\boldsymbol{q}} + \varepsilon_{\boldsymbol{k}'-\boldsymbol{q}}}, & \tau_3 &= \frac{1}{N}\sum_{\boldsymbol{q}} \frac{\cos^2 q_z}{\varepsilon_{\boldsymbol{k}+\boldsymbol{q}} + \varepsilon_{\boldsymbol{k}'-\boldsymbol{q}}}, \\ \tau_4 &= \frac{1}{N}\sum_{\boldsymbol{q}} \frac{\gamma_{\boldsymbol{q}}\cos q_z}{\varepsilon_{\boldsymbol{k}+\boldsymbol{q}} + \varepsilon_{\boldsymbol{k}'-\boldsymbol{q}}}, & \tau_5 &= \frac{1}{N}\sum_{\boldsymbol{q}} \frac{\gamma_{\boldsymbol{q}}^2}{\varepsilon_{\boldsymbol{k}+\boldsymbol{q}} + \varepsilon_{\boldsymbol{k}-\boldsymbol{q}}}. \end{aligned} \tag{3.32}$$

Setting $\boldsymbol{k} = 0$ in Eq. (3.30), we obtain

$$\Gamma_1 = \langle\Gamma\rangle - 4J_0A_1 + 12J_1A_2. \tag{3.33}$$

(2) $\boldsymbol{k}_1 = -\boldsymbol{k}_2 = \boldsymbol{Q}$

We use the following *Ansatz*:

$$\Gamma(\boldsymbol{q}-\boldsymbol{Q}) + \Gamma(-\boldsymbol{q}-\boldsymbol{Q}) = 2\left(\langle\Gamma\rangle - 4J_0^{\parallel}A_1'\cos q_z + 12J_1^{\parallel}A_2'\gamma_{\boldsymbol{q}}\right). \tag{3.34}$$

Substituting (3.34) into (3.29), we obtain the equations for $\langle\Gamma\rangle$, A_1', and A_2':

$$\begin{pmatrix} \tau_0 & -4J_0^{\parallel}\tau_1 & 12J_1^{\parallel}\tau_2 \\ \tau_1 & -4J_0^{\parallel}\tau_3 + 1 & 12J_1^{\parallel}\tau_4 \\ \tau_2 & -4J_0^{\parallel}\tau_4 & 12J_1^{\parallel}\tau_5 + 1 \end{pmatrix} \begin{pmatrix} \langle\Gamma\rangle \\ A_1' \\ A_2' \end{pmatrix} = \begin{pmatrix} 1 \\ 1 \\ -1/2 \end{pmatrix}. \tag{3.35}$$

Setting $\boldsymbol{q} = \boldsymbol{Q}$ in Eq. (3.34), we obtain

$$\Gamma_2 = 2\langle\Gamma\rangle - 8J_0^{\parallel}A_1' - 12J_1^{\parallel}A_2'. \tag{3.36}$$

Since the solutions of equations (3.31) and (3.35) cannot be written in simple form, we show the numerical results for several cases in the following.

Figure 3.5 shows the calculated Γ_1 and Γ_2 for the XY model ($J_0^{\parallel} = J_1^{\parallel} = 0$) as a function of $J_0^{\perp}/J_1^{\perp}$. In this case the solution of the integral equation (3.29) is simply

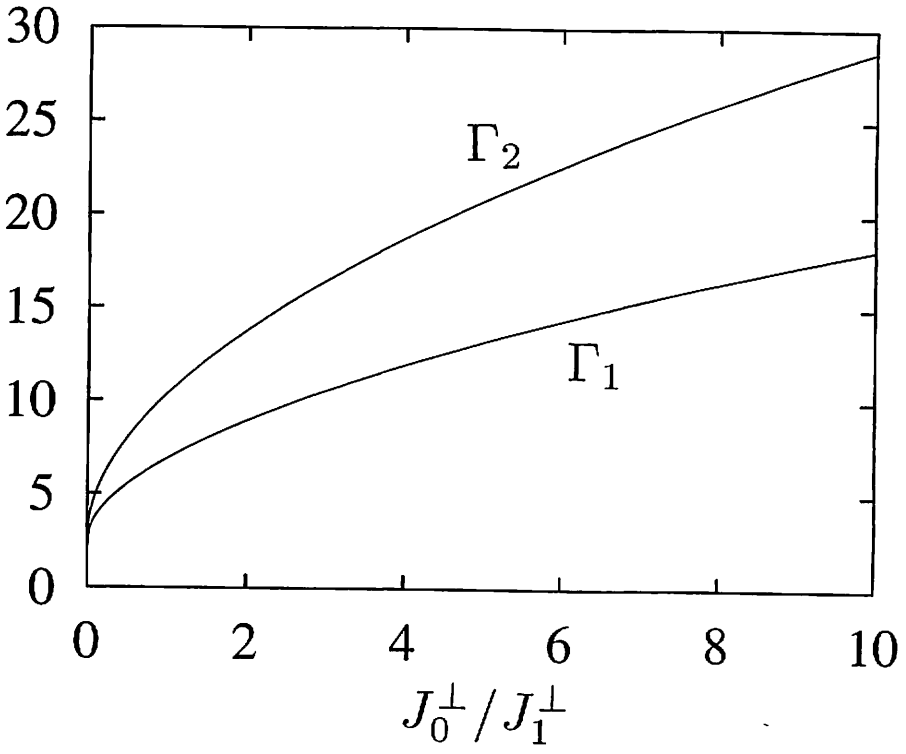

Figure 3.5: Γ_1 and Γ_2 calculated for the XY model. $J_1^\perp$ is taken to be 1.

given by $\Gamma(q) \equiv \langle\Gamma\rangle = 1/\tau_0$. We see that Γ_1 is always smaller than Γ_2 so that the ground-state spin structure of the XY model near saturation is the umbrella-type structure (Fig. 3.3(a)), as is expected from the classical spin theory.

Figure 3.6 shows the results for the isotropic case $J_0^\perp = J_0^\parallel = J_0$, $J_1^\perp = J_1^\parallel = J_1$. The classical ground state is nontrivially degenerate for this case. We see that Γ_1 is always larger than Γ_2 so that the ground-state spin structure is the coplanar structure in Fig. 3.3(b) or (c). This result is consistent with the conclusion drawn from the $1/S$ expansion [3,21].

Figures 3.7 shows the results for the case of antiferromagnetic c-chains calculated by taking $J_1^\perp = J_1^\parallel = J_1$, $J_0^\perp = -J_0^\parallel = J_0$. We see that $\Gamma_1 < \Gamma_2$ in almost all of the region so that the ground-state spin structure is the umbrella type (Fig. 3.3(a)); this is in agreement with the classical theory. However, as shown in Fig. 3.7(b), Γ_2 is larger than Γ_1 for small J_0. In this region quantum fluctuations are strong enough to stabilize the coplanar structure.

In all cases above, Γ_1 and Γ_2 vanish logarithmically in the limit $J_0 \to 0$. This is in fact usual in two-dimensional systems, implying that the ground-state energy

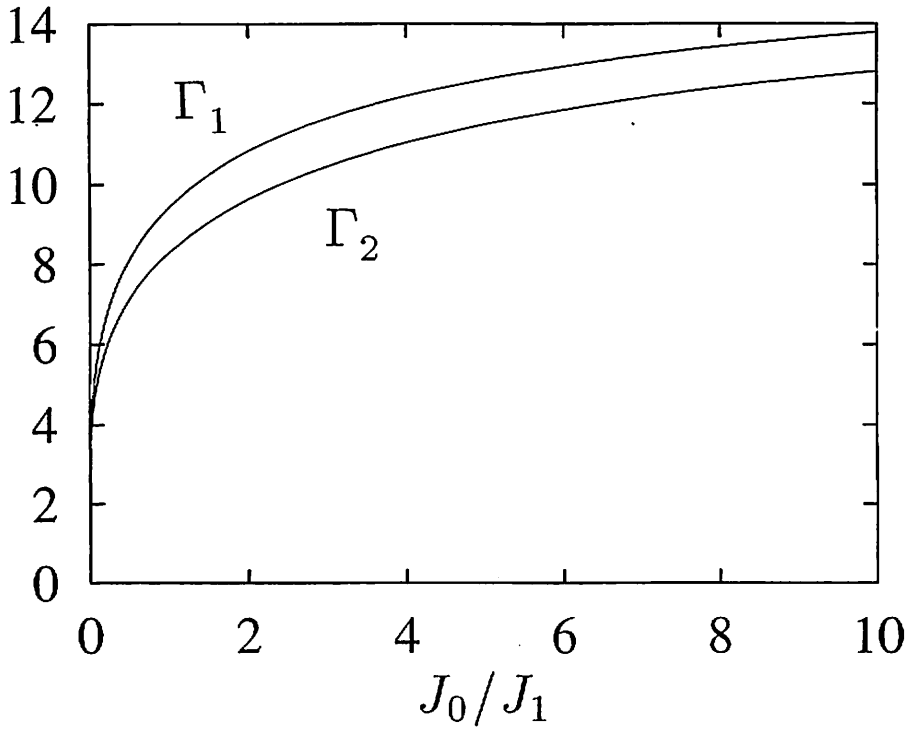

Figure 3.6: Γ_1 and Γ_2 calculated for the isotropic case: $J_0^{\perp} = J_0^{\parallel} = J_0$, $J_1^{\perp} = J_1^{\parallel} = J_1$. J_1 is taken to be 1.

cannot be expressed as an analytic expansion in $H_c - H$ near the saturation field.

We calculated Γ_1 and Γ_2 using the following reasonable values for the parameters for $CsCuCl_3$: $J_0^{\perp} = 28$K, $J_1^{\perp} = J_1^{\parallel} = 4.9$K, while changing the ratio $J_0^{\parallel}/J_0^{\perp}$. The above parameters are the same as used by Tanaka *et al.* [22] to interpret ESR data [23]. Figure 3.8 shows the result: we find that $\Gamma_1 > \Gamma_2$ if $J_0^{\parallel}/J_0^{\perp}$ is larger than about 0.9. (Γ_1 and Γ_2 become negative for large $J_0^{\parallel}$, suggesting that the non-collinear spin structures are unstable for this parameter region; actually we can see even in the classical spin theory that the non-collinear structures are unstable for enough large $J_0^{\parallel}$.) According to the experimental results [22], the anisotropy in $CsCuCl_3$ is estimated as $J_0^{\parallel}/J_0^{\perp} = 0.99$. Therefore the ground-state spin structure is the coplanar structure of Fig. 3.3(b) or (c). In order to determine which structure has the lower energy, we have to calculate Γ_3. However it is a very difficult task to evaluate Γ_3 since infinitely many diagrams appear in the calculation; we have not yet succeeded in solving this problem. But we have shown that the ground-state spin structure of $CsCuCl_3$ for $H||c$, near saturation, is the coplanar structure. This result is consistent with the result (in chapter 2) based on the $1/S$ expansion [21]. In zero

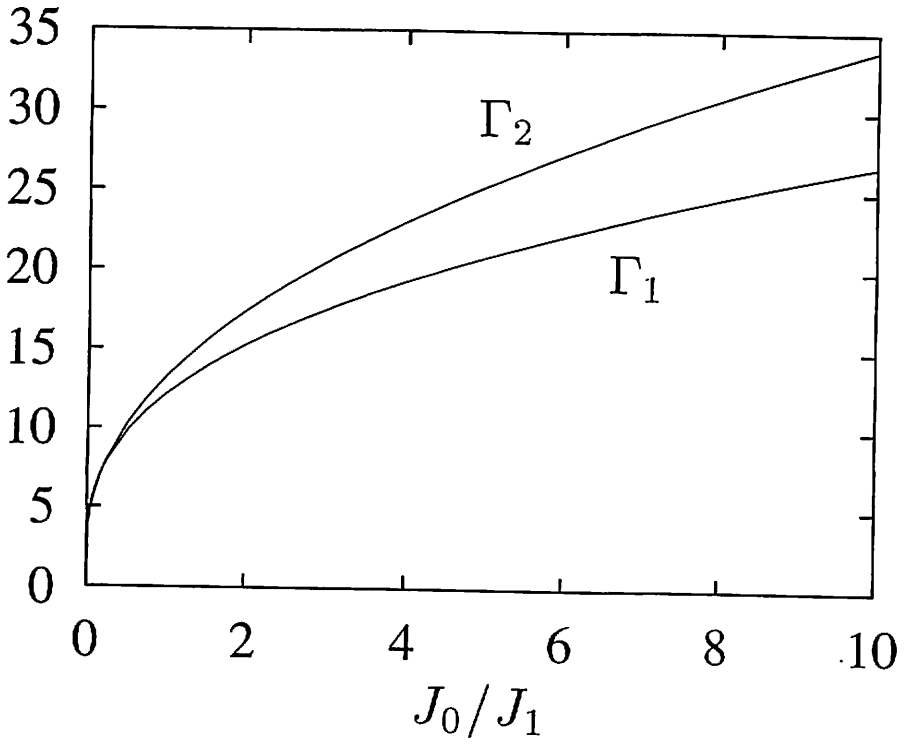

(a)

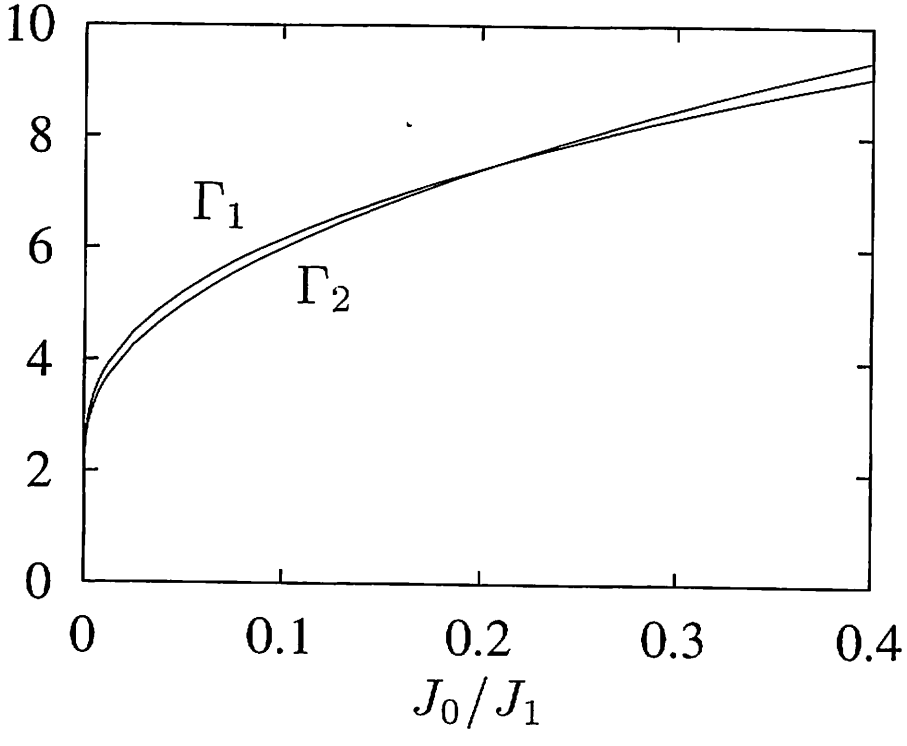

(b)

Figure 3.7: Γ_1 and Γ_2 for the case of antiferromagnetic chain: $J_0^{\perp} = -J_0^{||} = J_0$, $J_1^{\perp} = J_1^{||} = J_1$. J_1 is taken to be 1. Part (b) shows the behavior at small J_0.

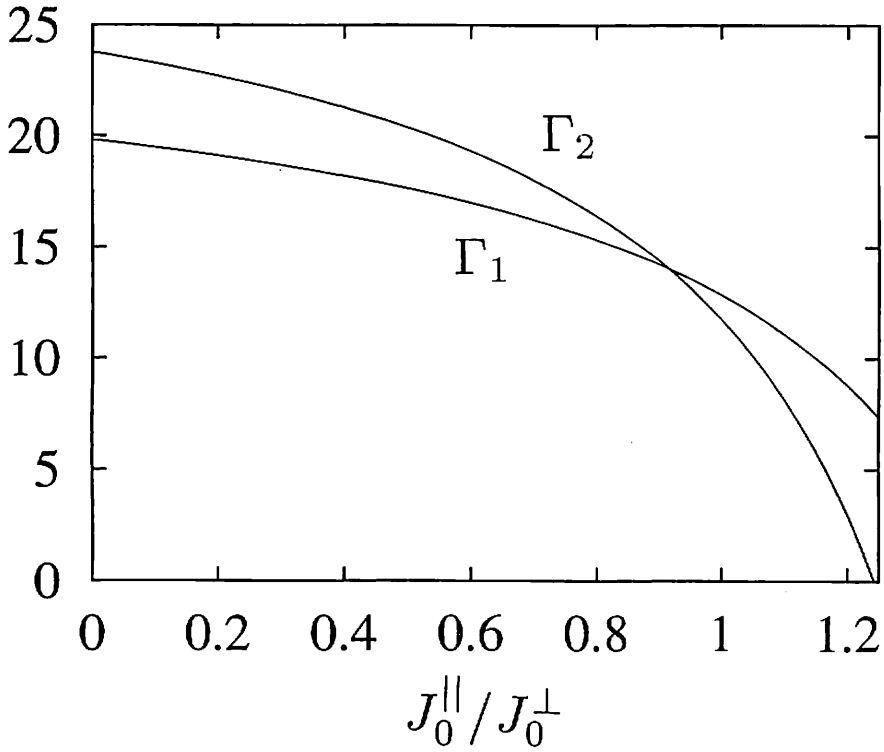

Figure 3.8: Γ_1 and Γ_2 calculated for the parameters chosen as $J_0^{\perp} = 28\text{K}, J_1^{\perp} = J_1^{\parallel} = 4.9\text{K}$. Γ_1 and Γ_2 are scaled by the interchain coupling $J_1^{\perp}$.

field, the neutron-scattering data show that the spins lie in the c-plane, taking the 120° structure. The zero-field spin structure should be continuously connected to the umbrella-type structure in Fig. 3.3(a), but not to the coplanar structure. Therefore the spin structure must change at an intermediate magnetic field. Experimentally, the phase transition of $CsCuCl_3$ in a magnetic field has been detected with various methods [24-30]. Motokawa and his coworkers determined the magnetic structure in the high-field region [24,25]. According to the experimental results, the high-field magnetic structure agrees with that in Fig. 3.3(c). A recent experiment in the temperature region close to the Néel temperature also supports their conclusion [26]. However we cannot say at this stage which spin structure [Fig. 3.3(b) or (c)] has the lower energy within the framework of the present study.

3.4 The Case of Arbitrary Spin S

In this section we extend the method to the case of arbitrary spin S. The spin operators with arbitrary S can be transformed to boson operators via Holstein-

Primakoff, Dyson-Maleev, or other transformations. Using these transformations, we can derive an equivalent lattice-boson Hamiltonian for arbitrary S in a form similar to Eq. (3.3). Then we can calculate the ground state energy in the same manner as in the previous section. The choice of the transformation from spin operators to boson operators is only a matter of convenience; the final results should not depend on the method of transformation, if terms to the same order are summed completely. For the present calculation the Dyson-Maleev transformation

$$S_i^z = S - a_i^\dagger a_i,\ S_i^+ = \sqrt{2S}a_i,\ S_i^- = \sqrt{2S}a_i^\dagger\left(1 - \frac{a_i^\dagger a_i}{2S}\right), \tag{3.37}$$

is the most convenient. Substituting the transformation (3.37) into the spin Hamiltonian (3.1), we obtain the boson Hamiltonian

$$\mathcal{H} = \sum_{\boldsymbol{k}}(2S\varepsilon_{\boldsymbol{k}} - \mu)a_{\boldsymbol{k}}^\dagger a_{\boldsymbol{k}} + \frac{1}{2N}\sum_{\boldsymbol{k},\boldsymbol{k}',\boldsymbol{q}}\left[V_{\boldsymbol{q}}^{\parallel} - \frac{1}{2}(V_{\boldsymbol{k}}^{\perp} + V_{\boldsymbol{k}'}^{\perp})\right]a_{\boldsymbol{k}+\boldsymbol{q}}^\dagger a_{\boldsymbol{k}'-\boldsymbol{q}}^\dagger a_{\boldsymbol{k}}a_{\boldsymbol{k}'}, \tag{3.38}$$

where

$$V_{\boldsymbol{k}}^{\perp} = -4J_0^{\perp}\cos k_z + 12J_1^{\perp}\gamma_{\boldsymbol{k}}, \tag{3.39}$$

and the saturation field for arbitrary S is defined by

$$H_c = [4(J_0^{\perp} - J_0^{\parallel}) + 6J_1^{\perp} + 12J_1^{\parallel}]S. \tag{3.40}$$

The same procedure developed in the previous sections can be used if we make the replacements $\varepsilon_{\boldsymbol{k}} \to 2S\varepsilon_{\boldsymbol{k}}$ and $V_{\boldsymbol{q}} \to V_{\boldsymbol{q}}^{\parallel} - (V_{\boldsymbol{k}}^{\perp} + V_{\boldsymbol{k}'}^{\perp})/2$. Here we must be careful about the fact that the interaction part of the Hamiltonian is not Hermitian. We introduce the order parameters in the same way in Eq. (3.8) and express the energy in the form Eq. (3.19). And then we have the three candidates in Fig. 3.3 for the ground-state spin structure. The ground state is selected among the three structures according to the three quantities Γ_1, Γ_2 and Γ_3. The integral equation of the effective potential for this case is given by

$$\Gamma(\boldsymbol{q}) = V_{\boldsymbol{q}}^{\parallel} + \langle\Gamma\rangle - \frac{1}{2SN}\sum_{\boldsymbol{q}'}\frac{V_{\boldsymbol{q}-\boldsymbol{q}'}^{\parallel}}{\varepsilon_{\boldsymbol{k}+\boldsymbol{q}'} + \varepsilon_{\boldsymbol{k}'-\boldsymbol{q}'}}\Gamma(\boldsymbol{q}'),$$

$$\frac{V_{\boldsymbol{Q}}^{\perp}}{2SN}\sum_{\boldsymbol{q}}\frac{\Gamma(\boldsymbol{q})}{\varepsilon_{\boldsymbol{k}+\boldsymbol{q}} + \varepsilon_{\boldsymbol{k}'-\boldsymbol{q}}} = \frac{1}{2}(V_{\boldsymbol{k}}^{\perp} + V_{\boldsymbol{k}'}^{\perp}) + \left(1 - \frac{1}{2S}\right)\langle\Gamma\rangle. \tag{3.41}$$

One can find the solution of the equation (3.41) in the same form as Eq. (3.30) or Eq. (3.34). The equations corresponding to Eqs.(3.31) and (3.35) are

$$\frac{1}{2S}\begin{pmatrix} (1-2S)/V_{\boldsymbol{Q}}^{\perp}+\tau_0 & -4J_0^{\parallel}\tau_1 & 12J_1^{\parallel}\tau_2 \\ \tau_1 & -4J_0^{\parallel}\tau_3+2S & 12J_1^{\parallel}\tau_4 \\ \tau_2 & -4J_0^{\parallel}\tau_4 & 12J_1^{\parallel}\tau_5+2S \end{pmatrix}\begin{pmatrix} \langle\Gamma\rangle \\ A_1 \\ A_2 \end{pmatrix}=\begin{pmatrix} 1 \\ 1 \\ 1 \end{pmatrix}, \quad (3.42)$$

$$\frac{1}{2S}\begin{pmatrix} (1-2S)/V_{\boldsymbol{Q}}^{\perp}+\tau_0 & -4J_0^{\parallel}\tau_1 & 12J_1^{\parallel}\tau_2 \\ \tau_1 & -4J_0^{\parallel}\tau_3+2S & 12J_1^{\parallel}\tau_4 \\ \tau_2 & -4J_0^{\parallel}\tau_4 & 12J_1^{\parallel}\tau_5+2S \end{pmatrix}\begin{pmatrix} \langle\Gamma\rangle \\ A_1' \\ A_2' \end{pmatrix}=\begin{pmatrix} 1 \\ 1 \\ -1/2 \end{pmatrix}, \quad (3.43)$$

respectively. It is easy to confirm that Eqs.(3.42) and (3.43) coincide with Eqs.(3.31) and (3.35) for $S=1/2$, respectively. The ground-state spin structure near saturation for arbitrary spin S could be determined by solving the equations (3.42) and (3.43). The results for arbitrary S are qualitatively the same as for $S=1/2$.

Here we consider the large-S limit to see the connection between the classical and the quantum theories. We expand Γ_1, Γ_2 and Γ_3 in terms of $1/S$ as

$$\Gamma_1=\Gamma_1^{(0)}+\frac{1}{S}\Gamma_1^{(1)}+\frac{1}{S^2}\Gamma_1^{(2)}+\cdots, \quad (3.44)$$

$$\Gamma_2=\Gamma_2^{(0)}+\frac{1}{S}\Gamma_2^{(1)}+\frac{1}{S^2}\Gamma_2^{(2)}+\cdots, \quad (3.45)$$

$$\Gamma_3=\frac{1}{S}\Gamma_3^{(1)}+\frac{1}{S^2}\Gamma_3^{(2)}+\frac{1}{S^3}\Gamma_3^{(3)}+\cdots. \quad (3.46)$$

For the Hamiltonian (3.38), the expansion in $1/S$ is equivalent to the expansion in the interaction. The leading term in the $1/S$ expansion is equivalent to the classical spin theory. $\Gamma_1^{(0)}$ and $\Gamma_2^{(0)}$ are given by the bare interaction, and $\Gamma_3^{(1)}$ is given by the lowest-order perturbation:

$$\Gamma_1^{(0)}=V_0^{\parallel}-V_{\boldsymbol{Q}}^{\perp}=4(J_0^{\perp}-J_0^{\parallel})+6J_1^{\perp}+12J_1^{\parallel}, \quad (3.47)$$

$$\Gamma_2^{(0)}=V_0^{\parallel}-V_{\boldsymbol{Q}}^{\perp}+V_{\boldsymbol{Q}}^{\parallel}-V_{\boldsymbol{Q}}^{\perp}=\Gamma_1^{(0)}+\Delta J, \quad (3.48)$$

$$\Gamma_3^{(1)}=\frac{1}{2}\Delta J\left(1-\frac{\Delta J}{18J_1^{\perp}}\right), \quad (3.49)$$

where $\Delta J=4(J_0^{\perp}-J_0^{\parallel})+6(J_1^{\perp}-J_1^{\parallel})$. If $\Delta J>0$, the classical ground state is of the umbrella type of Fig. 3.3(a), while the ground state is the coplanar one in Fig. 3.3(c) for $\Delta J<0$. For $\Delta J=0$, the ground state has the continuous degeneracy characterized by the condition

$$|\psi_{\boldsymbol{Q}}|^2+|\psi_{-\boldsymbol{Q}}|^2=\mu/18J_1^{\perp}, \quad (3.50)$$

which is equivalent to (1.4). Quantum fluctuations should be important, if the anisotropy is sufficiently small. Hence we consider the quantum corrections to Γ_1, Γ_2 and Γ_3 for the isotropic case. The next-order corrections in $1/S$ are given by the next-order calculations in the perturbation theory. Figure 3.9 shows the $1/S$ quantum correction to Γ_1 and Γ_2. This calculation should be equivalent to expanding the spin wave calculation in chapter 2 in terms of $1-h$ to the leading order. We see that $\Gamma_1^{(1)} > \Gamma_2^{(1)}$ so that the $1/S$ correction favors the coplanar structure, as is expected. Quantum corrections show a logarithmical divergence at small J_0, suggesting that the convergence of the $1/S$ expansion is not good for small J_0. It seems that the quantum corrections approach zero in the large J_0 limit. Actually we can expand solutions of equations (3.42) and (3.43) in terms of $(J_1/J_0)^{1/2}$ for large J_0 as follows:

$$\Gamma_1 = 18J_1 \left\{ 1 - 0.9654 \left(\frac{1}{2S}\right) \left(\frac{J_1}{J_0}\right)^{1/2} + 0.9090 \left(\frac{1}{2S}\right)^2 \left(\frac{J_1}{J_0}\right) + \left[0.1182 \left(\frac{1}{2S}\right) - 0.8766 \left(\frac{1}{2S}\right)^3 \right] \left(\frac{J_1}{J_0}\right)^{3/2} + \cdots \right\}, \tag{3.51}$$

$$\Gamma_2 = 18J_1 \left\{ 1 - 1.2680 \left(\frac{1}{2S}\right) \left(\frac{J_1}{J_0}\right)^{1/2} + 1.48347 \left(\frac{1}{2S}\right)^2 \left(\frac{J_1}{J_0}\right) + \left[0.3802 \left(\frac{1}{2S}\right) - 1.857 \left(\frac{1}{2S}\right)^3 \right] \left(\frac{J_1}{J_0}\right)^{3/2} + \cdots \right\}, \tag{3.52}$$

where the coefficients have been evaluated by numerical integrations. Note that higher-order terms in J_1/J_0 contain higher-order terms in $1/S$. The quantum corrections to Γ_1 and Γ_2 vanish in the limit $J_0/J_1 \to \infty$. This fact can be understood in the following way: if the intrachain ferromagnetic interaction is very strong, each chain behaves as one spin with large S. Thus in the large J_0 limit, the system can be regarded effectively as a large-S system. We thus conclude that the $1/S$ expansion is valid even for $S = 1/2$ if J_0 is not so small, at least for the isotropic system.

Figure 3.10 shows the quantum correction to Γ_3 to order $1/S^2$. We see that $\Gamma_3^{(2)} < 0$ and thus the ground-state spin structure for the large-S limit is Fig. 3.3(c), in agreement with the result of the spin-wave calculation [21]. The next-order correction term has opposite sign compared to the first-order correction, but is small compared with the $1/S$ term for large J_0. Up to order $1/S^2$, the convergence of the $1/S$ expansion for Γ_3 does not seem to be good for not so large J_0. However, as in the calculation of Γ_1 and Γ_2, we expect the result of the large-S expansion to be

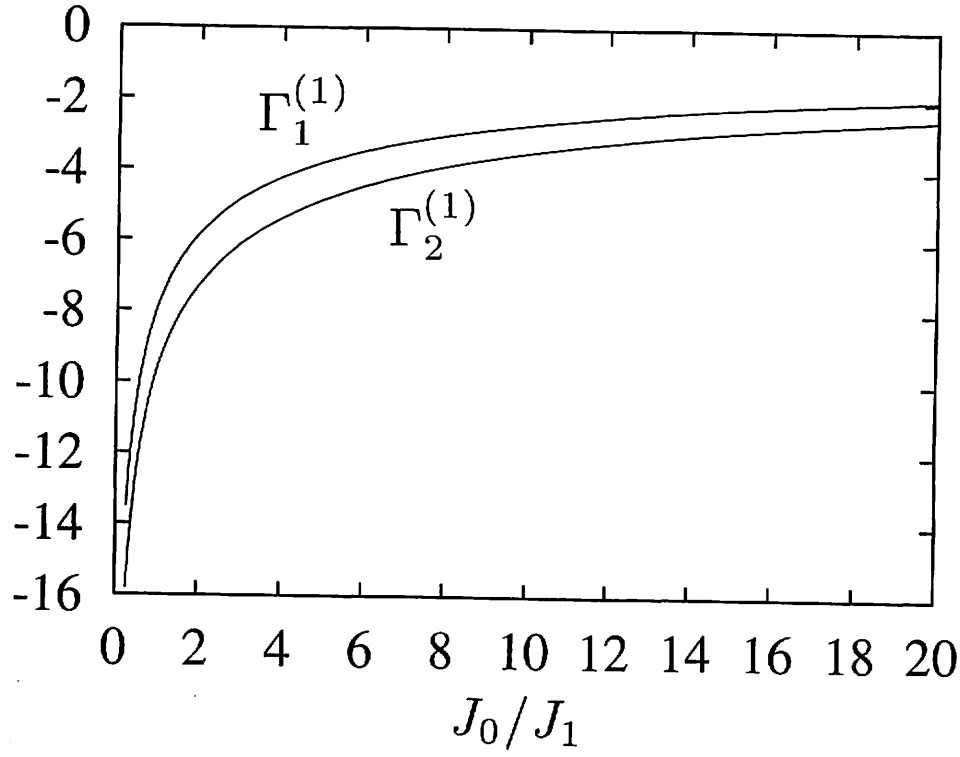

Figure 3.9: The quantum correction to Γ_1 and Γ_2.

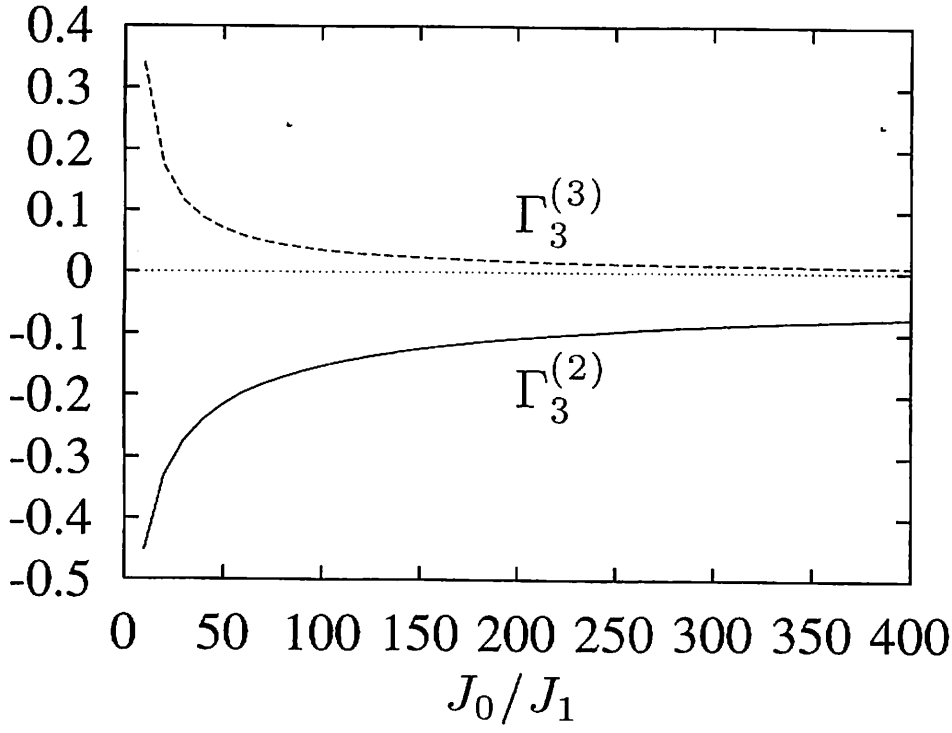

Figure 3.10: The quantum correction to Γ_3. The solid line represents $\Gamma_3^{(2)}$ and the broken line represents $\Gamma_3^{(3)}$.

Chapter 4

Incommensurate State of $CsCuCl_3$ in Transverse Magnetic Field

4.1 Introduction

In the previous chapters we studied the effect of quantum fluctuations when the magnetic field is applied parallel to the c-axis. We showed explicitly that the quantum fluctuations can make the ground-state spin structure different from the classically stable state. The phase transition of $CsCuCl_3$ in a magnetic field applied parallel to the c-axis was successfully explained as a quantum-fluctuation-induced phase transition, which leads to a new spin structure for $H > H_c$. Results of neutron-scattering experiments in the high-field region appear to be consistent with the proposed spin structure. In view of these developments, it is important to study next the effect of a transverse magnetic field on $CsCuCl_3$. This case is more complicated, since the magnetic field breaks the axial symmetry of the system. The purpose of this chapter is to determine the spin structure of $CsCuCl_3$ in transverse field (perpendicular to the c-axis), and also to see the effect of quantum fluctuations.

For the perpendicular field case, the observed magnetization curve shows a small plateau around 12T as shown in Fig. 1.7. According to theoretical studies of the triangular antiferromagnet in an external magnetic field, thermal and/or quantum fluctuations strongly favor the collinear configuration [2,3]. It has been predicted theoretically that the magnetization curve shows a plateau (corresponding to the collinear configuration) at one third of the saturation magnetization [3]. Thus one may suspect that the observed plateau corresponds to the theoretically predicted one for the triangular antiferromagnet. In the case of $CsCuCl_3$, however, the situation

is much more complicated even at the classical (mean-field) level, due to the helical spin structure caused by the DM interaction. We therefore first examine the ground state at the classical (*i.e.* mean-field) level [42,43].

Nagamiya *et al.* first investigated the effect of a transverse magnetic field on the helical spin structure, for the case when this structure is caused by a competition between symmetric exchange interactions [44]. When an external field is applied in the plane of the spin rotation, a small magnetic field induces a uniform magnetic moment by polarizing the helical structure. At a certain field H_c the system undergoes a first-order transition into a so-called fan structure; this consists of alternative right- and left-handed helices. If the field is increased further, the fan shrinks gradually. At the saturation field H_s, the system undergoes a smooth transition to a ferromagnetic state.

On the other hand, if the helical spin structure is caused by the anti-symmetric DM interaction, left-handed and right-handed helices are not degenerate so that the fan state is not stable [45]. If the interchain interaction is ferromagnetic, there is a smooth transition from helical structure to the completely aligned ferromagnetic state. In $CsCuCl_3$, the problem is much more complicated, because there are 3 sublattices antiferromagnetically coupled with each other. The solution of this problem is far from trivial, as shown later. The classical theory predicts a continuous phase transition from the helical (i.e. incommensurate) state to the commensurate, incompletely aligned state. The commensurate state has a nontrivial degeneracy, which should be lifted by quantum (and thermal) fluctuations. The classical theory has unusual features which are due to the existence of the nontrivial degeneracy in the commensurate state. Therefore we take into account the effect of quantum fluctuations to the incommensurate state in a phenomenological manner. We see a large modification from the classical incommensurate state by quantum fluctuations.

This chapter is arranged as follows. In section 4.2 the classical theory is applied to determine the ground-state spin structure. The effect of quantum fluctuations is then examined in section 4.3, which is followed by a summary in section 4.4.

4.2 Classical Theory of the Ground-State Spin Structure

$CsCuCl_3$ in a transverse magnetic field is described by the following Hamiltonian:

$$\mathcal{H} = -2J_0 \sum_{in} \boldsymbol{S}_{in} \cdot \boldsymbol{S}_{in+1} + 2J_1 \sum_{\langle ij \rangle n} \boldsymbol{S}_{in} \cdot \boldsymbol{S}_{jn} - \sum_{in} \boldsymbol{D} \cdot (\boldsymbol{S}_{in} \times \boldsymbol{S}_{in+1}) - g\mu_B H \sum_{in} S^x_{in}. \quad (4.1)$$

We neglect the anisotropic exchange interaction and the dipole-dipole interaction for simplicity. According to the experimental data [15,16,20], the coupling constants are given by $J_0 = 28$K, $J_1 = 4.9$K and $D = 5$K. If the classical theory is applied to Eq. (4.1), $\mathcal{H}$ is regarded as an energy function whose minimum has to be determined. Without the interplane (J_0 and D) terms, Eq. (4.1) describes a classical triangular antiferromagnet in an in-plane magnetic field; the ground state of this system is known to have three sublattices. We assume that this structure is maintained for nonzero field, and also that the spins remain in the a-b plane. This is a reasonable assumption for $CsCuCl_3$, since the DM term is most effective for spins lying in the a-b plane and the anisotropic exchange term [omitted from (4.1)] is of easy-plane type [22]. Then the structure in the n-th plane can be described by the angles ϕ_{jn} (j=1,2,3) between the spins and the field:

$$\boldsymbol{S}_{jn} = S(\cos\phi_{jn}, \sin\phi_{jn}, 0). \quad (4.2)$$

The structure in the c direction is determined by the interplane terms. Since D is small compared to J_0, the variation in the c direction is slow. Therefore we treat the interplane terms in the continuum approximation, to lowest order. Then the average energy per spin $\mathcal{E} = \mathcal{H}/LN_{ab}$ (L: length of the sample in the c direction, N_{ab}: number of spins in each a-b plane) is given by

$$\mathcal{E} = -2J_0S^2 + \frac{1}{L}\int_0^L dz \sum_{j=1}^{3} \left[\frac{J_0S^2}{3}\left(\frac{d\phi_j}{dz}\right)^2 - \frac{DS^2}{3}\frac{d\phi_j}{dz} + 2J_1S^2\cos(\phi_{j+1} - \phi_j) - \frac{g\mu_B HS}{3}\cos\phi_j \right]. \quad (4.3)$$

The structure is described by the three functions $\phi_j(z)$, where z is the coordinate in the c direction. The lowest-energy state can be obtained by solving the Euler-Lagrange equations for the angles $\phi_j(z)$:

$$-\frac{2J_0S^2}{3}\frac{d^2\phi_j}{dz^2} + 2J_1S^2[\sin(\phi_{j-1} - \phi_j) + \sin(\phi_{j+1} - \phi_j)] + \frac{g\mu_B HS}{3}\sin\phi_j = 0\ . \quad (4.4)$$

Notice that the DM term does not appear in this differential equation.

At this point we wish to mention that if J_1 is *negative* (that is, if the interchain coupling is *ferromagnetic*), it is much simpler to determine the ground state; in fact Moriya and Miyadai [45] discussed such a case in the low field limit. In this case the phases are uniform in each plane ($\phi_1 = \phi_2 = \phi_3$) so that the system (4.3) is equivalent to the Frank-van der Merwe model and the other incommensurate systems [46]. Thus the incommensurate-commensurate transition in the case of ferromagnetic interchain belongs to the usual class of the incommensurate systems, as discussed in Appendix B.

The above model allows both commensurate and incommensurate structures, favored at high and low fields respectively. In the commensurate structures, each layer is in the same state, and the phases ϕ_j are independent of z. Incommensurate structures are periodic in z, with wavenumber q; the period $Z = 2\pi/q$, which has to be determined to minimize $\mathcal{E}$, is not a rational multiple of the a-b plane spacing. Clearly the above continuum model (4.3) predicts an incommensurate structure at small fields and a completely aligned structure at very high fields; the latter is a commensurate structure with all spins parallel to the field ($\phi_j(z) = 0$ for all z), and is obtained at fields greater than the saturation field $H_s = 18JS/g\mu_B$.

4.2.1 Modification of Helical Spin Structure in a Weak Field

For zero field, Eq. (4.4) gives immediately an incommensurate structure, which is simply a helical spin structure:

$$\phi_1(z) = qz, \quad \phi_2(z) = \phi_1(z) - 2\pi/3, \quad \phi_3(z) = \phi_1(z) + 2\pi/3. \tag{4.5}$$

Minimization of the energy leads to $q = q_0 = D/(2J_0)$. Since the actual value of q is $q_0 = \arctan(D/2J_0)$ [19], and since $D = 0.089 \times 2J_0$ is small in $CsCuCl_3$ (giving a period of about 70 layers), the continuum approximation is expected to be valid. For nonzero field, Eq. (4.5) does not satisfy the Euler-Lagrange equation (4.4), since the last term in Eq. (4.4) produces a modulation of ϕ_j. As far as the weak-field region is concerned, the modulation is small so that it can be taken into account by

$$\begin{aligned} \phi_1(z) &= qz + a_1 \sin(qz), \\ \phi_2(z) &= \phi_1(z - Z/3), \end{aligned} \tag{4.6}$$

$$\phi_3(z) = \phi_1(z + Z/3),$$

where $Z = 2\pi/q$. The amplitude a_1 of the modulation is obtained by substituting (4.6) into (4.3) and keeping the first-order correction in H; the result is

$$a_1 = -\frac{2h}{1 + \frac{2J_0}{9J_1}q^2}; \tag{4.7}$$

here q is not the same as the zero-field value q_0, but is obtained by minimizing the energy. Substituting (4.6) and (4.7) into (4.3) and minimizing $\mathcal{E}$ with respect to q, we obtain

$$\frac{q}{q_0} = \left[1 + \frac{1}{2}\left(\frac{2h}{1 + \frac{2J_0}{9J_1}q_0^2}\right)^2\right]^{-1}. \tag{4.8}$$

We see that q decreases with increasing magnetic field. In fact, neutron-scattering experiments on $CsCuCl_3$[24-26] have detected a decrease of q due to the magnetic field, which is consistent with this result. The magnetization in the low-field limit is given by

$$M = g\mu_B Sh\left(\frac{1}{1 + \frac{2J_0}{9J_1}q^2}\right), \tag{4.9}$$

showing that the magnetization at low fields is slightly suppressed by the helical structure.

One could extend this treatment to higher field by generalizing (4.6) to

$$\begin{aligned} \phi_1(z) &= qz + \sum_{\ell=1}^{\infty} a_\ell \sin(\ell q z), \\ \phi_2(z) &= \phi_1(z - Z/3), \\ \phi_3(z) &= \phi_1(z + Z/3), \end{aligned} \tag{4.10}$$

where $\{a_\ell\}$ and q are determined by minimizing $\mathcal{E}$. This method, which is often used to study incommensurate structures, is certainly applicable to the present problem, but we present a different approach, which is equivalent to the above, but better suited to discuss the incommensurate-commensurate transition at high fields.

4.2.2 Incommensurate-Commensurate Transition

Let us discuss in a more general way incommensurate states of (4.4) and the transition to the commensurate state. First we note that, from Eq. (4.4), commensurate

structures corresponding to $\phi_j(z)$=independent of z are determined from the condition (1.8). Therefore the most stable commensurate states are degenerate as given by (1.9). The energy of these commensurate states is given by

$$\mathcal{E}_{\rm comm} = -2J_0S^2 - 3J_1S^2(1+3h^2). \tag{4.11}$$

These commensurate energies should be compared with the energy of incommensurate structures.

Now the problem is to determine the incommensurate state from the Euler-Lagrange equations (4.4). The incommensurate state is given by numerical solutions of the equations. This problem allows many kinds of solutions according to the boundary conditions. Among many solutions, the optimal incommensurate structure is obtained when each of the three phases ϕ_j changes by 2π over a period $\phi_j(z+Z) = \phi_j(z) + 2\pi$. Solutions for each field are optimized with respect to the wavenumber q.

Figure 4.1 shows the optimal wavenumber q as a function of the magnetic field calculated by using the parameters for $CsCuCl_3$. The result for weak fields is consistent with (4.8). The wavenumber decreases monotonically with increasing field and vanishes at the transition field $h_c \approx 0.473$. Above h_c the commensurate state, incompletely aligned, is stable up to the saturation field. Figure 4.1(b) shows that the wavenumber q vanishes linearly as the transition is approached. This linear behavior near the transition is the most important feature in the incommensurate state of $CsCuCl_3$. It is markedly different from what is standard in the incommensurate systems such as the Frank-van der Merwe model. As discussed in Appendix B, the wavenumber vanishes as the inverse of a logarithm near the transition, in conventional models. The unusual behavior of the wavenumber of q in our model can be traced back to the nontrivial degeneracy in the commensurate state, as discussed later.

Figure 4.2 shows the average energy density of the incommensurate state (evaluated at the optimal wavenumber) measured from the commensurate state: $\Delta\mathcal{E} = \mathcal{E} - \mathcal{E}_{\rm comm}$. Part (b) of the figure shows that the energy vanishes quadratically, so that the transition at $h \approx 0.473$ to the incompletely aligned commensurate structure is second-order.

Figure 4.3 shows the solutions (optimized with respect to the wavenumber q) of the Euler-Lagrange equation at various fields. The phases are plotted as a function

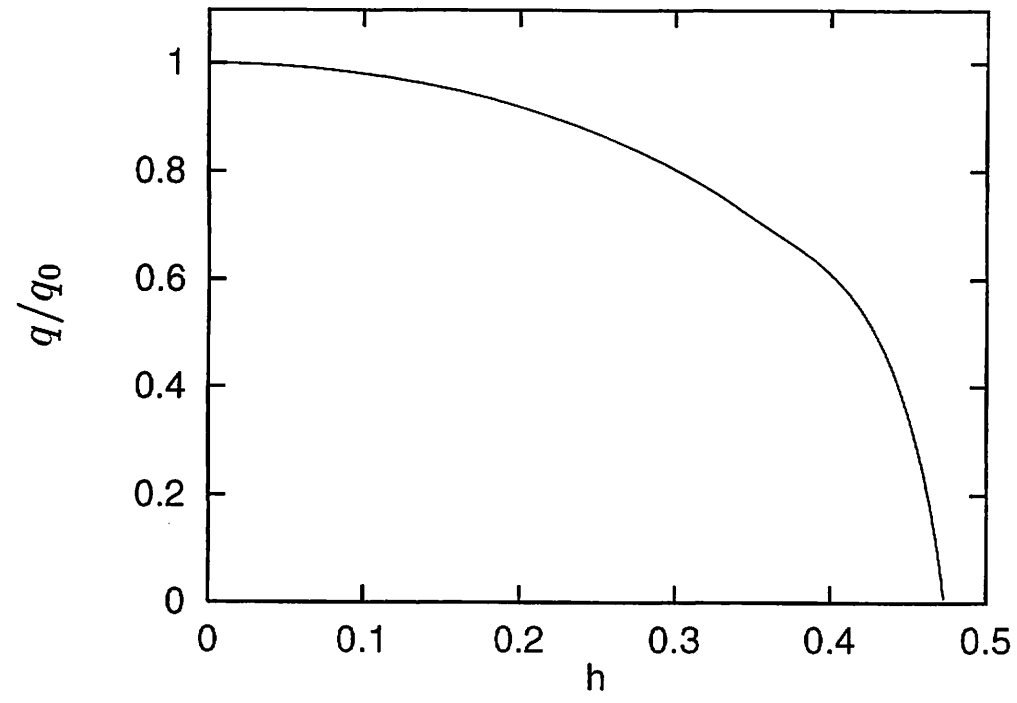

(a)

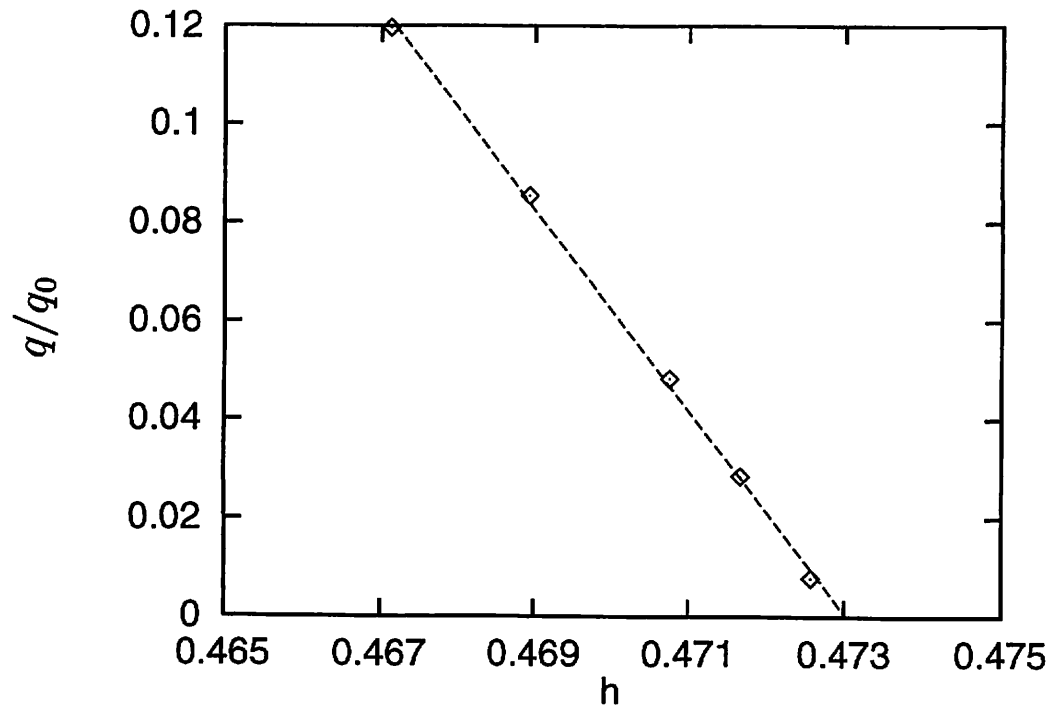

(b)

Figure 4.1: Normalized optimal wavenumber q/q_0 as a function of the reduced magnetic field $h = H/H_s$; q_0 is the optimal wavenumber $D/2J_0$ at $h = 0$. Part (b) shows the behavior near the transition to the commensurate structure.

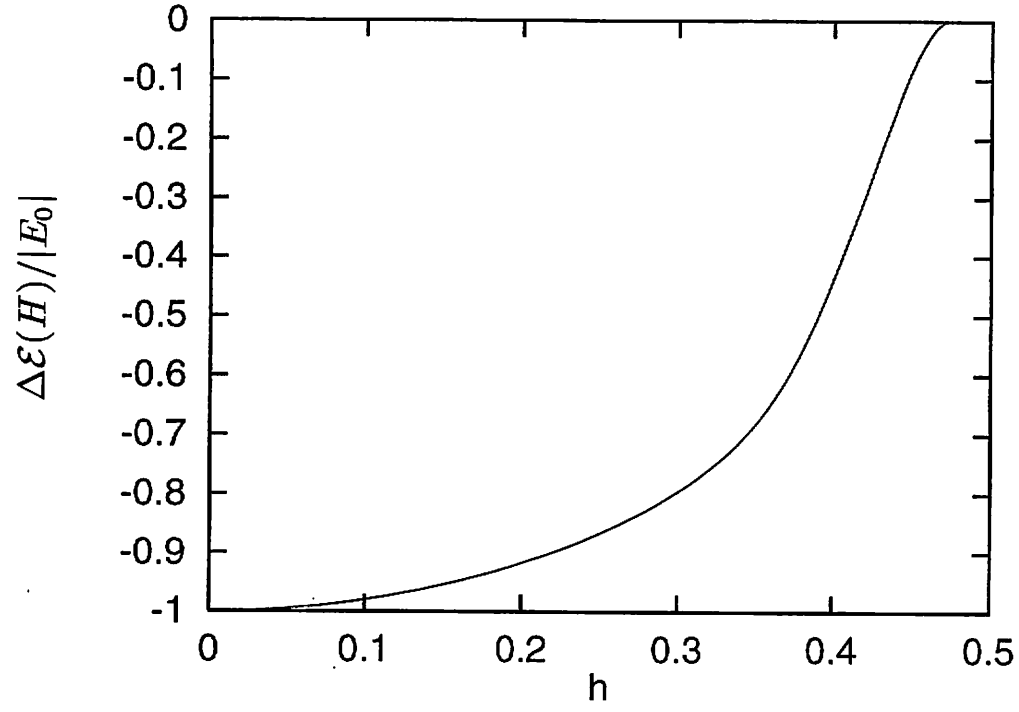

(a)

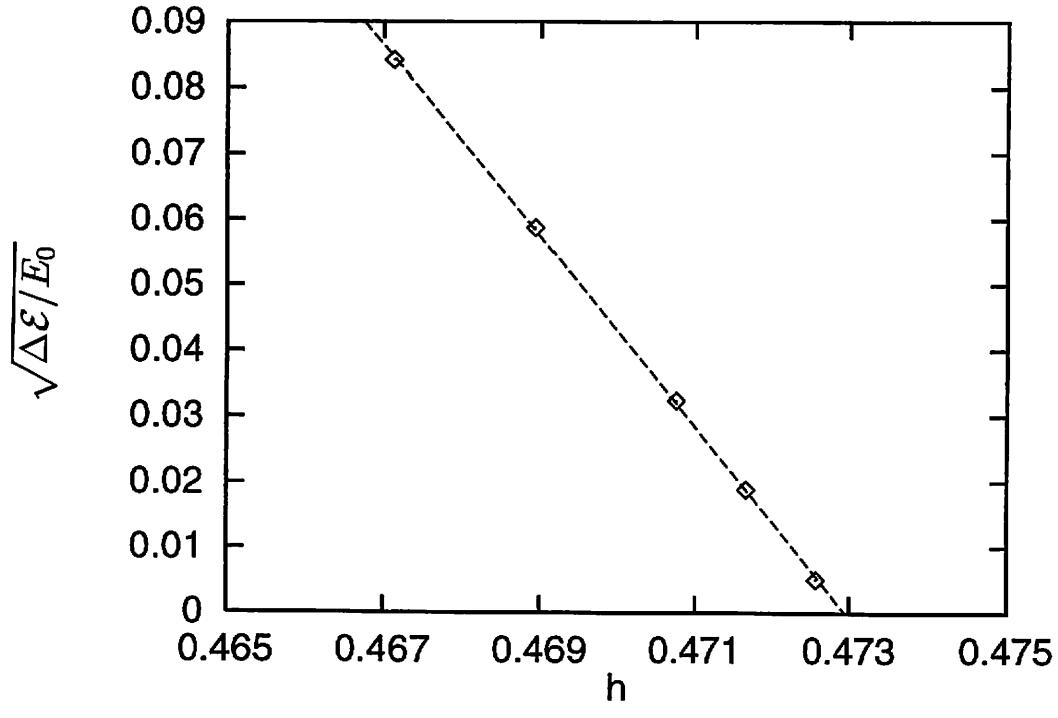

(b)

Figure 4.2: Normalized energy density optimized with respect to the wavenumber as a function of the reduced field $h = H/H_s$; the quantity plotted is $\Delta\mathcal{E}(H)/|E_0|$, where $E_0 = -D^2S^2/(4J_0)$. Part (b) shows the behavior of $\sqrt{\Delta\mathcal{E}/E_0}$ near the transition.

of $3z/Z$ in the range $0 \leq z \leq Z/3$. Outside this range, the phases are given by

$$\phi_1(z + Z/3) = \phi_3(z), \quad \phi_2(z + Z/3) = \phi_1(z), \quad \phi_3(z + Z/3) = \phi_2(z) + 2\pi, \quad (4.12)$$

etc. The origin is chosen so that $\phi_1(0) = 0$; the walls (which may not be well defined) are separated by $Z/3$ and located at $z = \pm Z/6$, *etc.* Figure 4.3(a) shows the solutions for $h = 0.3$. We see that the zero-field solution is only slightly modified by the magnetic field. Figure 4.3(b) shows the solutions for $h = 0.45$. A solitonic behavior is only moderately developed even though the field value is not far below the transition field $h_c \approx 0.473$. The nonmonotonic behavior of the phases seen in Figs. 4.3(b) and (c) is found for all $h > 1/3$. It is easily understood as a result of the nonmonotonic dependence of ϕ_1 and ϕ_2 on ϕ_3 for the commensurate state of a single layer for the same fields. Figure 4.3(c) shows the phases at a field $h \approx 0.4726$ (less than 0.1% below the transition); the structure is very different from what is typical in the conventional incommensurate systems, since there are no regions where the order parameters are even nearly constant. As discussed in Appendix B, the incommensurate states in conventional models are divided into well-defined wall regions and distinct commensurate regions. Between the walls, the order parameter is nearly constant, at a commensurately allowed value. However in the case of $CsCuCl_3$ there are infinitely many commensurately allowed states, due to the nontrivial degeneracy. Therefore the incommensurate state can gain simultaneously the driving energy (DM term) and the exchange energy by adopting a spatially varying structure. Therefore the transition to the commensurate state occurs in more gradual manner than in the usual cases. This is a reason why the behavior of the wavenumber q near the transition is different from the conventional models. At large fields, the commensurate relations Eq. (1.8) are well satisfied in the regions between the walls. The structure seen in Fig. 4.3(c) is just a sequence of planes each nearly in a commensurate state, plus a wall region. We note that the walls are not domain walls in the usual sense, since they do not separate distinct commensurate regions, but they are regions where one of the phases takes on commensurately forbidden values; the explicit expression is given by Eq. (1.10).

Figure 4.4 shows the magnetization curve. In the incommensurate state the magnetization is calculated from

$$M = \frac{M_0}{3Z} \int_0^Z dz(\cos\phi_1 + \cos\phi_2 + \cos\phi_3). \quad (4.13)$$

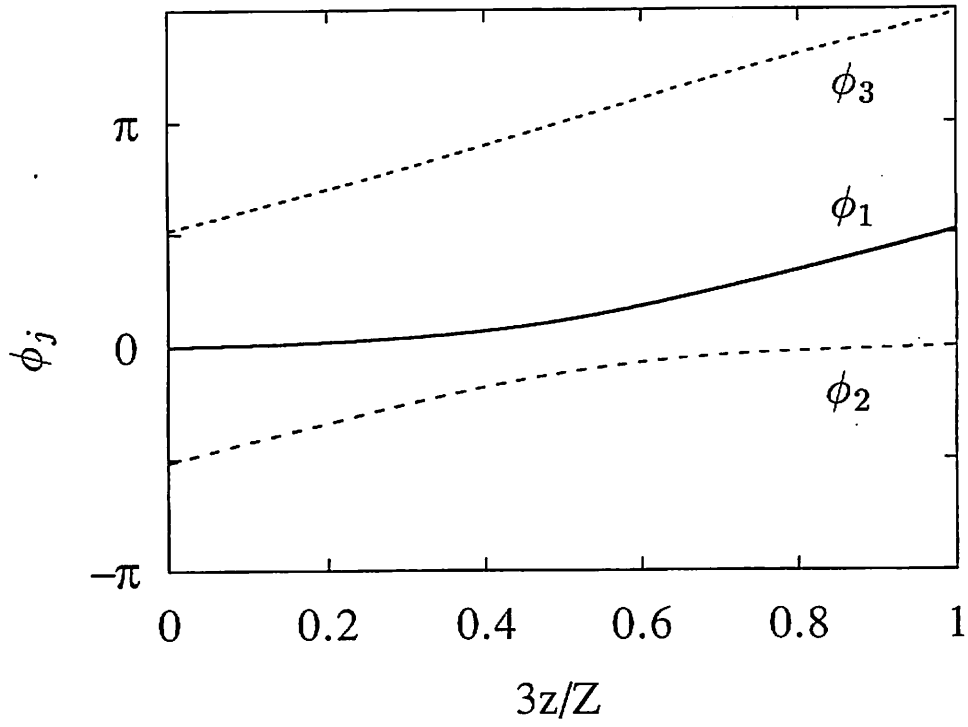

(a)

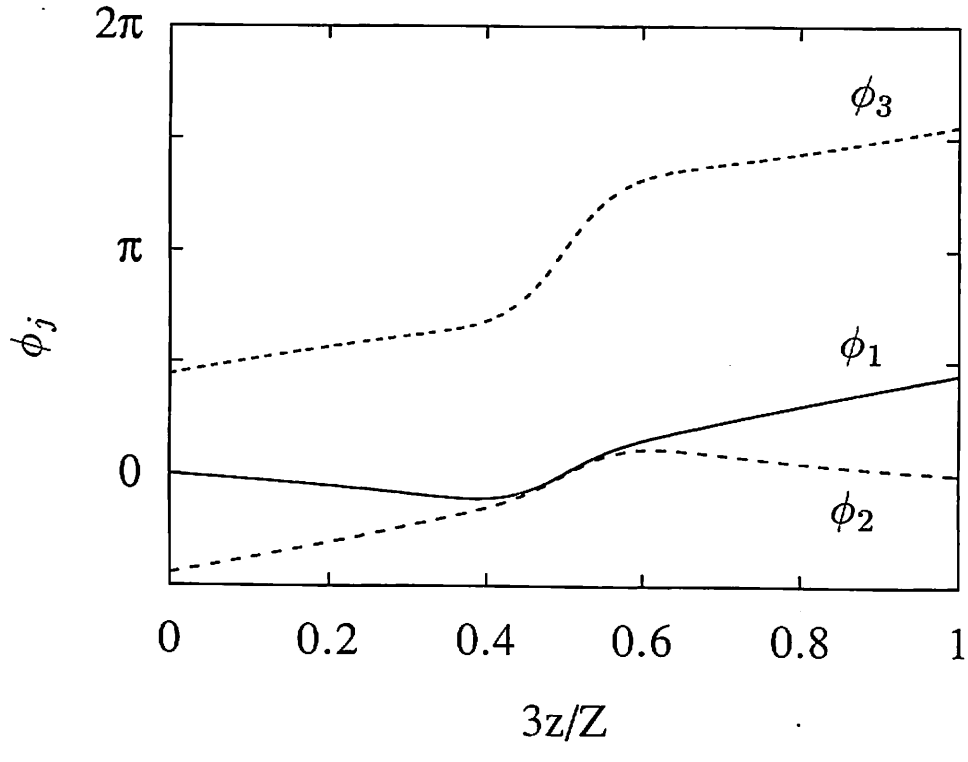

(b)

Figure 4.3: Phases ϕ_j as functions of $3z/Z$ at reduced field (a) $h = H/H_s = 0.3$, (b) 0.45, and (c) ≈ 0.4726(in the next page); the plots cover only 1/3 of the period Z of the structure.

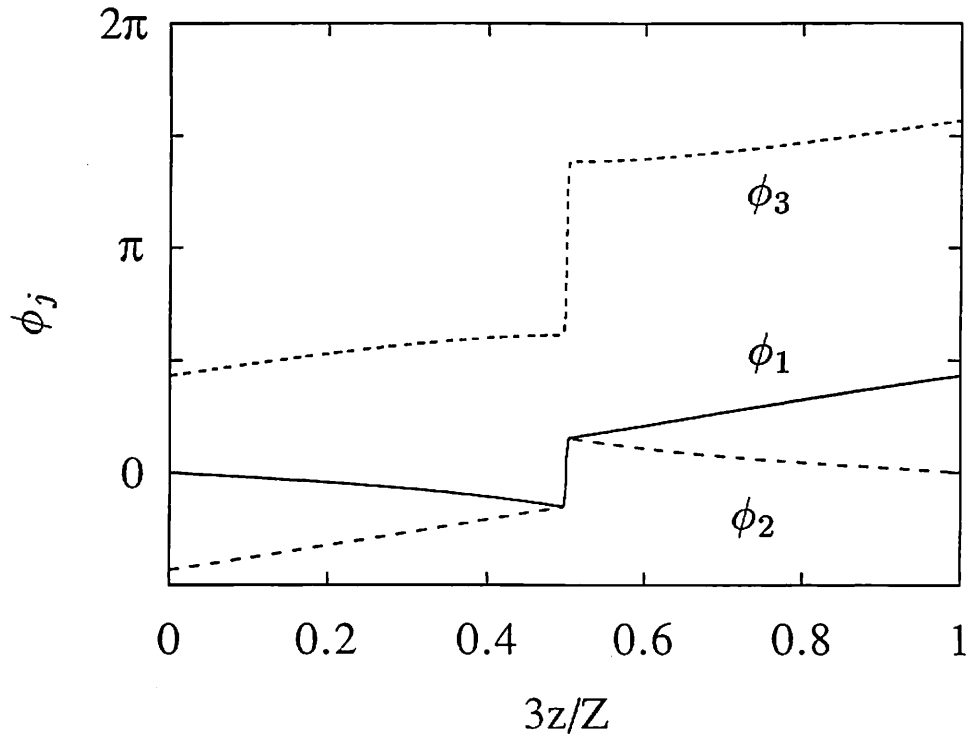

Fig. 4.3(c)

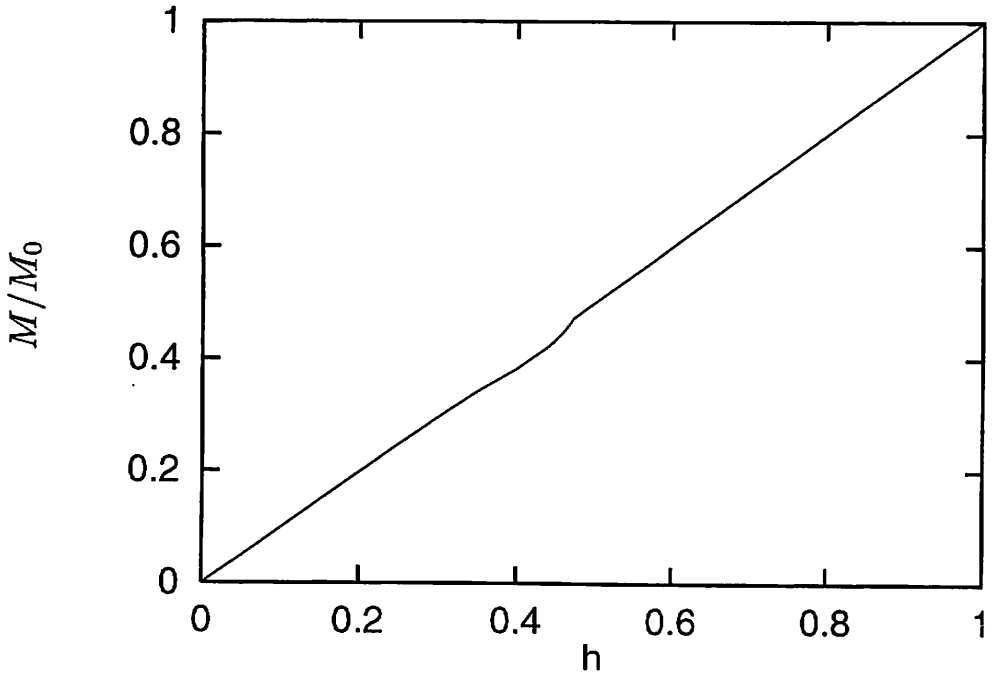

Figure 4.4: Normalized magnetization M/M_0 as a function of the reduced magnetic field $h = H/H_s$; M_0 is the saturation value $g\mu_B S$ of the magnetization.

In the commensurate state above H_c, the magnetization is given by $M = M_0 h$. The result for weak fields is consistent with (4.9). The suppression of the magnetization is relatively large near h_c because of the developing walls. Since the regions between walls are nearly in commensurate states and the walls are narrow, the magnetization in the incommensurate state is at most only a few percent below the commensurate value. Therefore the behavior observed experimentally [10,11] is likely due to quantum fluctuations neglected in the present treatment, as in the case of the field parallel to the c-axis [21]. This problem is discussed in the next section.

In summary, this section has applied the classical theory to study the nature of the incommensurate state of $CsCuCl_3$ in a transverse field. The classical ground state of $CsCuCl_3$ in transverse field has the following features:

(1) The wavenumber vanishes linearly at the transition to the commensurate state.
(2) The order parameter is neither constant nor nearly constant in the regions between the walls.
(3) The magnetization in the incommensurate state is at most only a few percent below the commensurate value.
(4) Many spin structures are degenerate for $h \geq h_c$.

In particular features (1) and (2) are unusual compared with other conventional incommensurate systems. They are easily understood to result from the existence of the nontrivial degeneracy in the commensurate state. In reality quantum fluctuations remove the nontrivial degeneracy. Therefore the classical incommensurate state does not seem to provide a the realistic description of $CsCuCl_3$, although it is very interesting from a theoretical point of view. We thus expect the classical incommensurate to be largely modified by quantum fluctuations.

In order to detect the phase transition to the commensurate state, Mino *et al.* measured the wavenumber q by neutron-scattering [24,25], examining the (1/3 1/3 δ) reflection; δ and q are connected through $q = 2\pi\delta/6$. Figure 4.5 shows the observed field dependence of δ. The results for low fields are consistent with Fig. 4.1 in that δ decreases with the increasing field. However, around 11T, δ stays nearly constant at about 0.045. These results are contrary to these of Fig. 4.1 which predicts that δ decreases monotonically and vanishes around 14T. This plateau region of q corresponds to the small plateau in the magnetization curve [10,11]. Since the

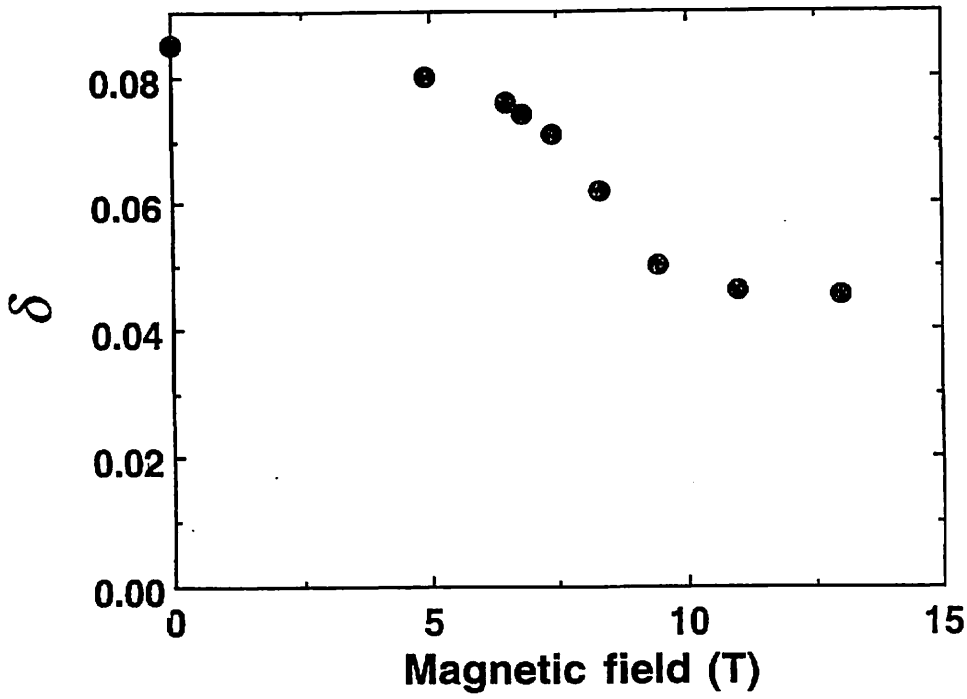

Figure 4.5: Observed helical pitch as a function of the magnetic field [24].

experimental results show that the incommensurate structure still exists in this region, one cannot interpret the magnetization plateau as what has been predicted for the standard triangular antiferromagnet [3]. To explain this unexpected behavior, we take into account the effect of quantum fluctuations on the incommensurate state in the next section.

4.3 Effect of Quantum Fluctuations

In this section we examine the effect of quantum fluctuations. Our goal is to include the quantum fluctuations in the theory of the incommensurate state and to explain the plateau in the wavenumber as observed by Mino *et al.* [24,25]. First we discuss the effect of quantum fluctuations in the commensurate state [42]. In the classical theory, many commensurate states are continuously degenerate. Quantum fluctuations remove this nontrivial degeneracy. This effect can be examined by the spin-wave theory, as we have done for $H||c$ in section 2.2. When we apply the spin-wave theory to the commensurate state, the antisymmetric DM term does not appear in any results. Therefore quantum selection occurs in the same way as in the stan-

dard triangular antiferromagnet [3]. The most stable commensurate configuration is shown in Fig. 2.1(b) for $h < 1/3$, and (c) for $h > 1/3$.

The extension of the spin-wave calculation to the incommensurate state is straightforward in principle. One could calculate the $1/S$ quantum correction to the classical energy as a function of the wavenumber q. The optimal wavenumber including the first quantum correction could be obtained by minimizing the energy to order $1/S$ with respect to q. However, as shown in Appendix C, the spin-wave theory does not work well for the incommensurate state. This is because the spin-wave theory does not take into account sufficiently the breaking of the classical degeneracy in determining the spin structures, but starts from the classical incommensurate state. As we have shown in the previous section, the classical incommensurate state is well described as the sequence of planes each nearly in a commensurate state. In reality such a spatially varying state should not be stable at large fields because quantum fluctuations remove the nontrivial degeneracy. The incommensurate state near the transition field is expected to consist of well-defined walls which separate distinct commensurate regions. Between the walls, the order parameter should be nearly constant at the commensurately stable value. This structure is very different from the classical incommensurate state, and thus difficult to be obtained by the perturbative approach such as the $1/S$ expansion. Therefore we apply a phenomenological approach to this problem in the following.

The most important effect of quantum fluctuations in this problem is the breaking of the classical nontrivial degeneracy. We take this effect into account by adding the following phenomenological term to the energy density $\mathcal{E}$:

$$\mathcal{E}_{\rm fluct} = \frac{1}{L}\int_0^L dz\{-J_2S^2[\cos^2(\phi_1-\phi_2)+\cos^2(\phi_2-\phi_3)+\cos^2(\phi_3-\phi_1)]\}, \quad (4.14)$$

where J_2 is assumed to be positive. Introduction of the phenomenological term $\mathcal{E}_{\rm fluct}$ is equivalent to introducing the biquadratic term

$$E_{\rm bq} = -\frac{J_2}{S^2}\sum_{<ij>n}(\boldsymbol{S}_{in}\cdot\boldsymbol{S}_{jn})^2, \quad (4.15)$$

in the classical Hamiltonian. One can easily see that the biquadratic term $E_{\rm bq}$ favors the collinear spin alignment. Since the biquadratic exchange interaction cannot be present in this $S = 1/2$ system, we must interpret this term as the energy function of the order parameters which originates from quantum fluctuations. (Of course

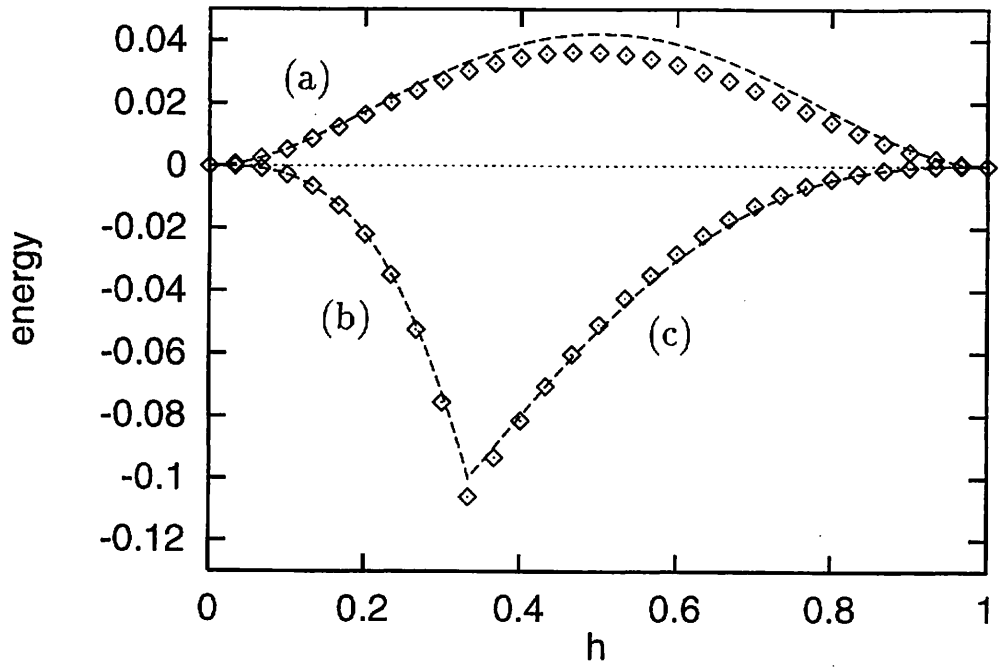

Figure 4.6: Comparison between the spin-wave calculation $\Delta E_{\rm SW}$ and the biquadratic function $E_{\rm bq}$. The broken lines express $E_{\rm bq}$ and the squares express $E_{\rm SW}$. Calculations were performed for the four spin configurations in Fig. 2.1. The values presented are measured relative to the coplanar structure in Fig. 2.1(d).

thermal fluctuations can also produce the biquadratic term in the expression of the free energy as explicitly shown in Eq. (1.18.)) In fact the biquadratic term $E_{\rm bq}$ well approximates the spin-configuration dependence of $\Delta E_{\rm SW}$. Figure 4.6 compares the $1/S$ quantum correction $E_{\rm SW}$ from the spin-wave theory and the biquadratic function $E_{\rm bq}$. The quantities have been calculated for the four spin configurations shown in Fig. 2.1. The energy is measured from the coplanar structure in Fig. 2.1(d), in both cases. As shown in the figure, good agreement between $E_{\rm bq}$ and $E_{\rm SW}$ is obtained for the parameters $J_0 = 28$K, $J_1 = 4.9$K, and $S = 1/2$, if we choose $J_2 = 0.2$K. Thus we expect that the phenomenological term $\mathcal{E}_{\rm fluct}$ captures well enough the effect of the breaking of the classical degeneracy by the quantum fluctuations.

The Euler-Lagrange equations for the angles $\phi_j(z)$, in the presence of $\mathcal{E}_{\rm fluct}$, are

$$-\frac{2J_0S^2}{3}\frac{d^2\phi_j}{dz^2} + 2J_1S^2[\sin(\phi_{j-1}-\phi_j)+\sin(\phi_{j+1}-\phi_j)]$$
$$-J_2S^2[\sin 2(\phi_{j-1}-\phi_j)+\sin 2(\phi_{j+1}-\phi_j)] + \frac{g\mu_{\rm B}HS}{3}\sin\phi_j = 0. \qquad (4.16)$$

First we look at the commensurate solutions. The nontrivial degeneracy in the ground state is removed by J_2 in the same way as by the quantum fluctuations. However the optimal spin configurations are not the same as in (1.19) and (1.20), but have to be obtained by minimizing the energy $\mathcal{E}$ (including $\mathcal{E}_{\rm fluct}$). The lowest spin configuration in the commensurate state is determined as follows.

[I] low-field structure

At low field the most stable structure is $\phi_1 = \pi, \phi_2 = -\phi_3 = \phi$. The angle ϕ is determined by minimizing the energy, which leads to the condition

$$6J_1(1-2\cos\phi) + 6J_2\cos\phi(1+2\cos 2\phi) + \frac{g\mu_{\rm B}H}{S} = 0. \tag{4.17}$$

The angle ϕ decreases monotonically with the magnetic field, and reaches 0 at $H_1 = (6J_1 - 3J_2)S/g\mu_{\rm B}$.

[II] intermediate collinear structure

The collinear alignment with $\phi_1 = \pi, \phi_2 = \phi_3 = 0$ is stable over a finite range of magnetic field $H_1 < H < H_2$, where $H_2 = 6(J_1 + J_2)S/g\mu_{\rm B}$. The magnetization in this region is one-third the saturation value.

[III] high-field structure

For $H_2 < H$, the most stable state is the one with $\phi_2 = \phi_3$. The phases ϕ_1 and ϕ_2 are determined by the following equations:

$$\begin{cases} -12J_1\sin(\phi_1-\phi_2) + 6J_2\sin 2(\phi_1-\phi_2) + \dfrac{g\mu_{\rm B}H}{S}\sin\phi_1 = 0, \\ -12J_1\sin(\phi_2-\phi_1) + 6J_2\sin 2(\phi_2-\phi_1) + \dfrac{g\mu_{\rm B}H}{S}\sin\phi_2 = 0. \end{cases} \tag{4.18}$$

All spins become parallel to the magnetic field ($\phi_1 = \phi_2 = \phi_3 = 0$) at the saturation field $H_{\rm s} = 18(J_1 - J_2)S/g\mu_{\rm B}$.

Let us now determine the incommensurate state by solving the Euler-Lagrange equation (4.16). For zero field, the incommensurate state is a simple helical structure as in Eq. (4.5), with the optimal wavenumber $q_0 = D/2J_0$. $\mathcal{E}_{\rm fluct}$ does not change the zero-field spin configuration, as expected. On the other hand, at large fields $\mathcal{E}_{\rm fluct}$ makes large modifications to the incommensurate state, as shown below.

Figure 4.7 shows the optimal wavenumber q as a function of the magnetic field for various values of J_2. The result for weak fields is almost the same as in the

classical case. (Here and below in this chapter "classical" means $J_2 = 0$.) For each parameter value we see a remarkable difference from the classical result near $h = 1/3$. For $J_2 = 0.13$K, the wavenumber remains nearly constant at about half q_0. This result seems to be consistent with the experimental result shown in Fig. 4.5. After the plateau, the wavenumber decreases rapidly and vanishes at $h_c \approx 0.446$. For $J_2 = 0.17$K, the wavenumber shows a hollow, rather than a plateau; the transition to the commensurate state occurs at $h_c \approx 0.442$. This strange behavior of q near $h = 1/3$ can be easily understood as an effect of $\mathcal{E}_{\text{fluct}}$. Since this term strongly favors the collinear state, the commensurate state is relatively stable near $h = 1/3$, as shown in Fig 4.9. Therefore the wavenumber shows relatively rapid decrease in the vicinity of $h = 1/3$. A marked difference can be seen for $J_2 = 0.2$K, which best approximates the spin-wave calculation. The collinear state is too strongly favored by $\mathcal{E}_{\text{fluct}}$, so that there appears an intermediate commensurate phase over the finite field region $0.318 < h < 0.348$. The second transition to the commensurate state occurs at $h_c \approx 0.439$. It seems that the leading-order calculation in the $1/S$ expansion overestimates the effect of quantum fluctuations. In fact we saw in section 3.3 that the next-order correction acts oppositely to the leading-order term. We conclude that $J_2 = 0.13$K gives the best result for the incommensurate state of $CsCuCl_3$.

The transition field H_c to the commensurate state is smaller for larger J_2. This is due to the fact that $\mathcal{E}_{\text{fluct}}$ favors the unique commensurate state so that incommensurate state cannot gain the DM energy. Near the transition to the commensurate state, the wavenumber vanishes rapidly, in contrast to the classical case. Figure 4.8 shows the behavior of the wavenumber near the transition field h_c. We see that the wavenumber vanishes as the inverse of a logarithm:

$$q \sim -a/\ln(h_c - h), \tag{4.19}$$

where a is some constant. As shown in Appendix B, this logarithmic behavior is usual in conventional models of incommensurate-commensurate transitions.

Figure 4.9 shows the average energy density of the incommensurate state evaluated at the optimal wavenumber (relative to the incompletely aligned commensurate structure at the same field). At low fields, we see that $|\Delta\mathcal{E}|$ decreases with increasing field, as for the classical incommensurate state. The nonmonotonic behavior of the energy density is seen in the intermediate-field region near $h = 1/3$. This is because

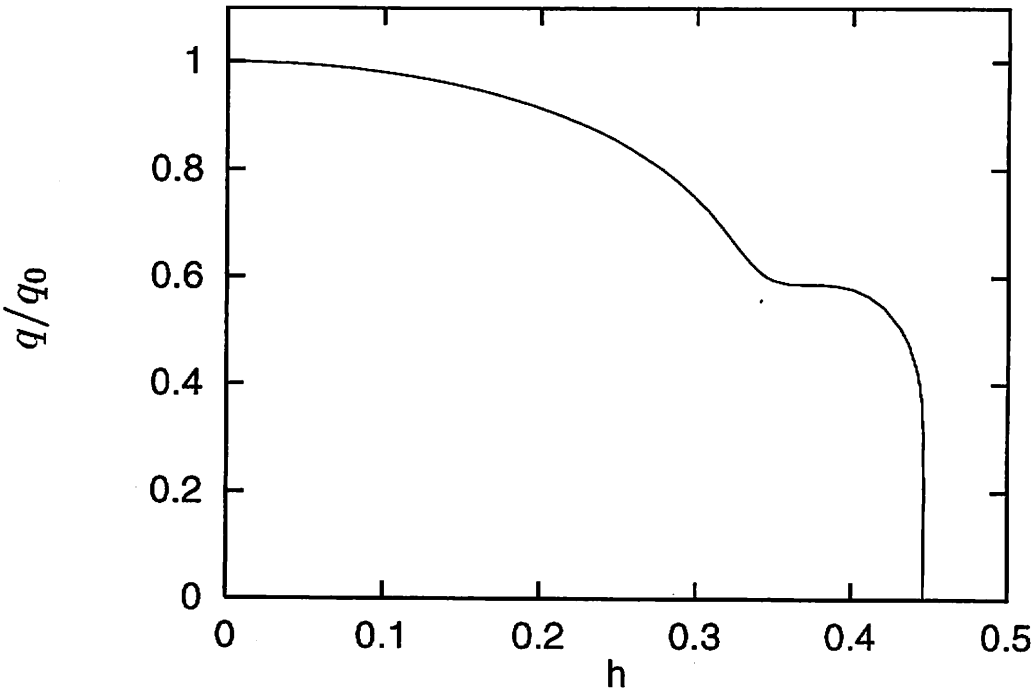

(a)

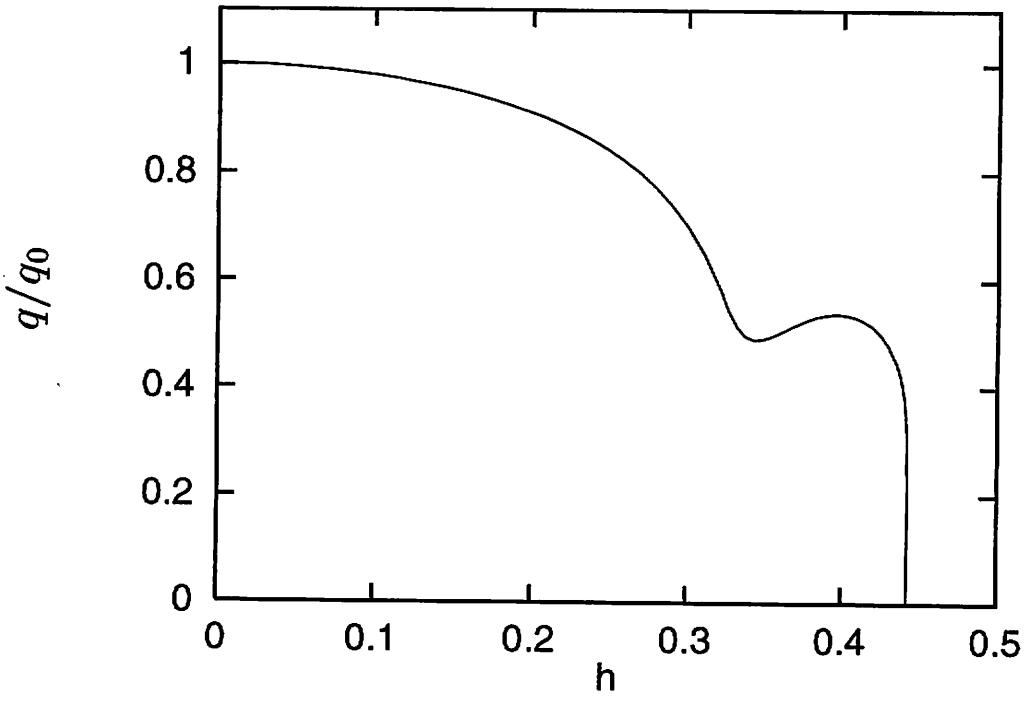

(b)

Figure 4.7: Normalized optimal wavenumber q/q_0 as a function of the reduced magnetic field $h = H/H_s$ with (a) $J_2 = 0.13$K, (b) 0.17K and (c) 0.2K(in the next page.)

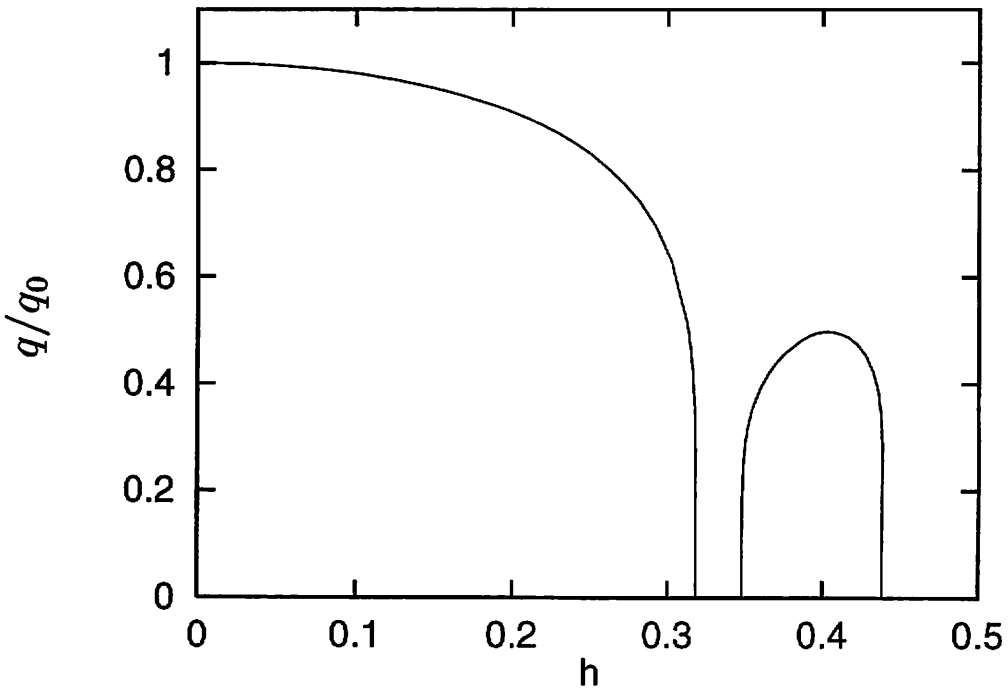

Fig. 4.7(c)

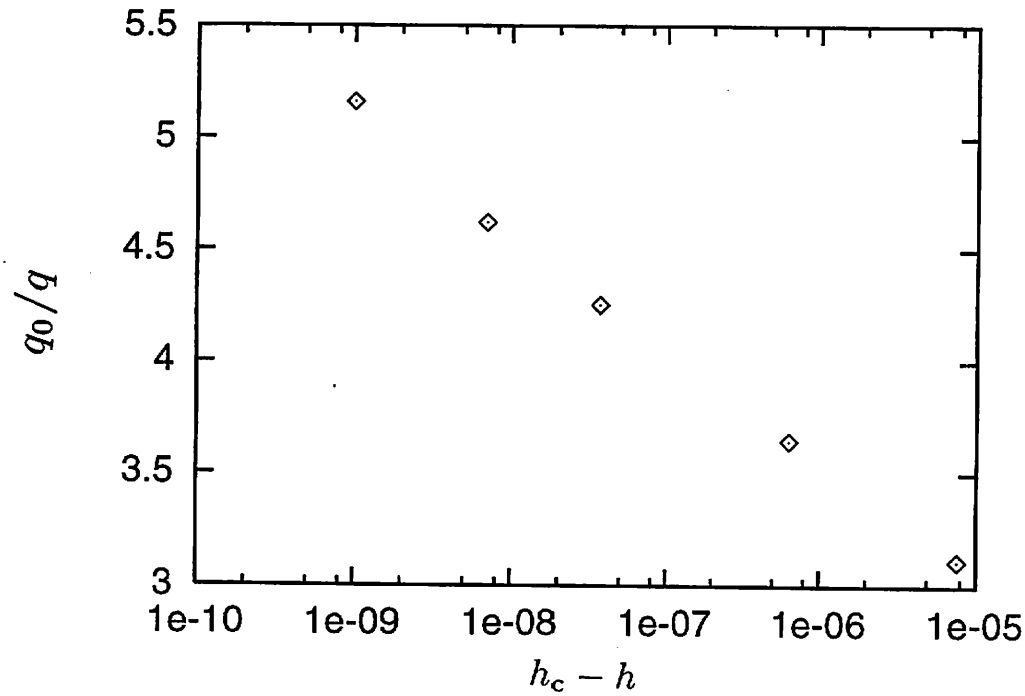

Figure 4.8: Inverse of the wavenumber q_0/q as a function of $h_c - h$ near the transition calculated for $J_2 = 0.13$K.

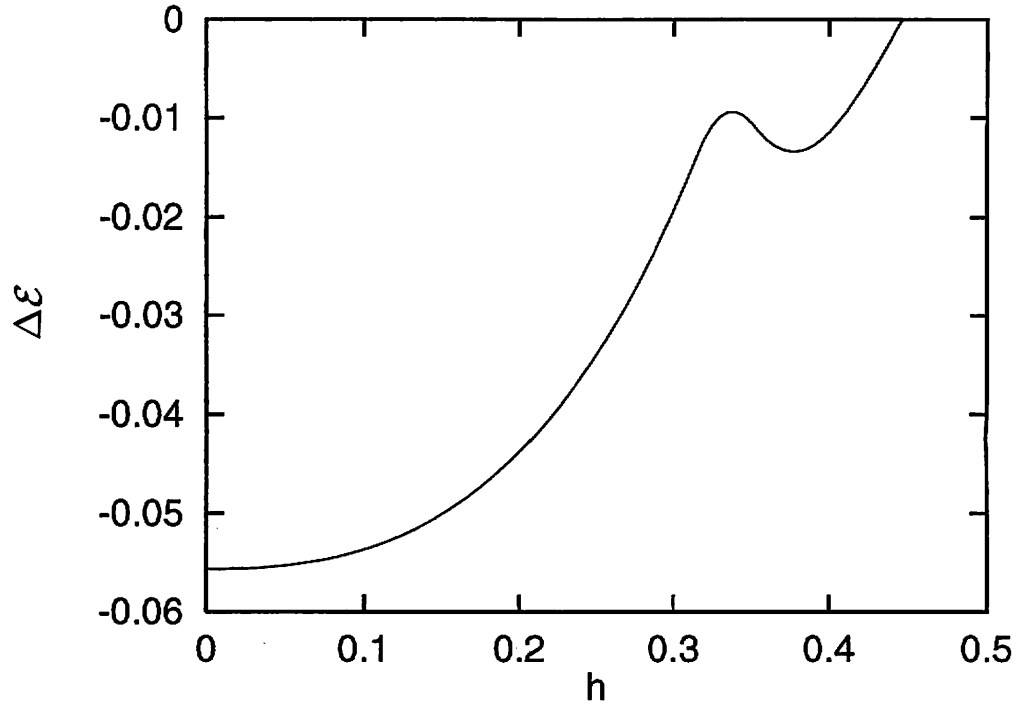

(a)

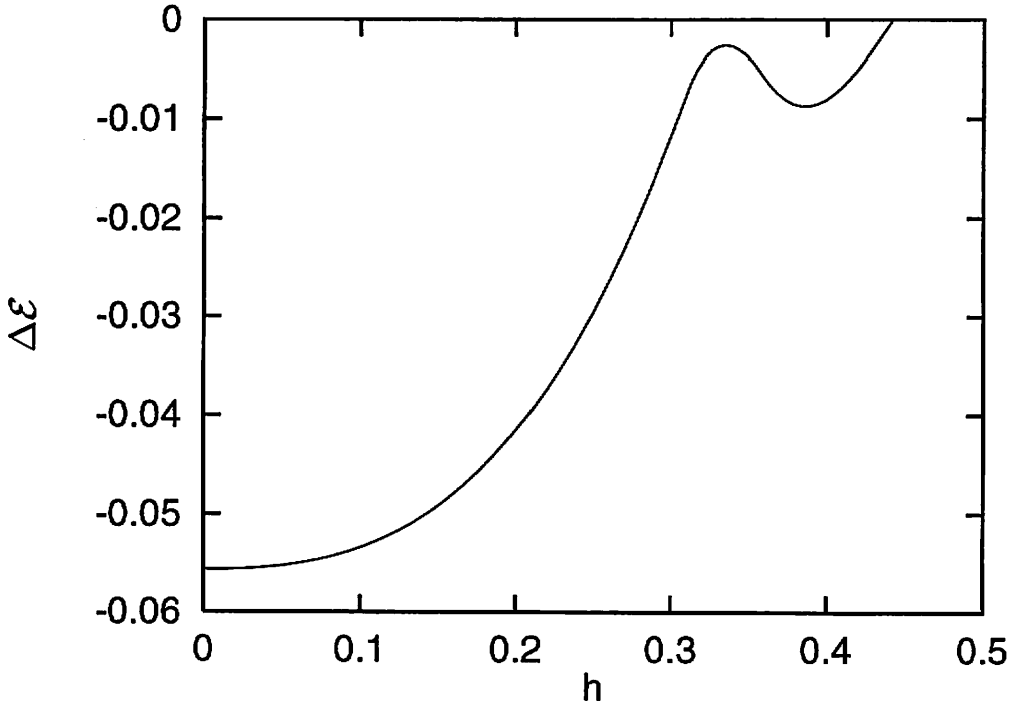

(b)

Figure 4.9: Energy density of the incommensurate state $\Delta\mathcal{E}$ as a function of the reduced field $h = H/H_s$ for (a) $J_2 = 0.13$K, (b) 0.17K and (c) 0.2K(in the next page.)

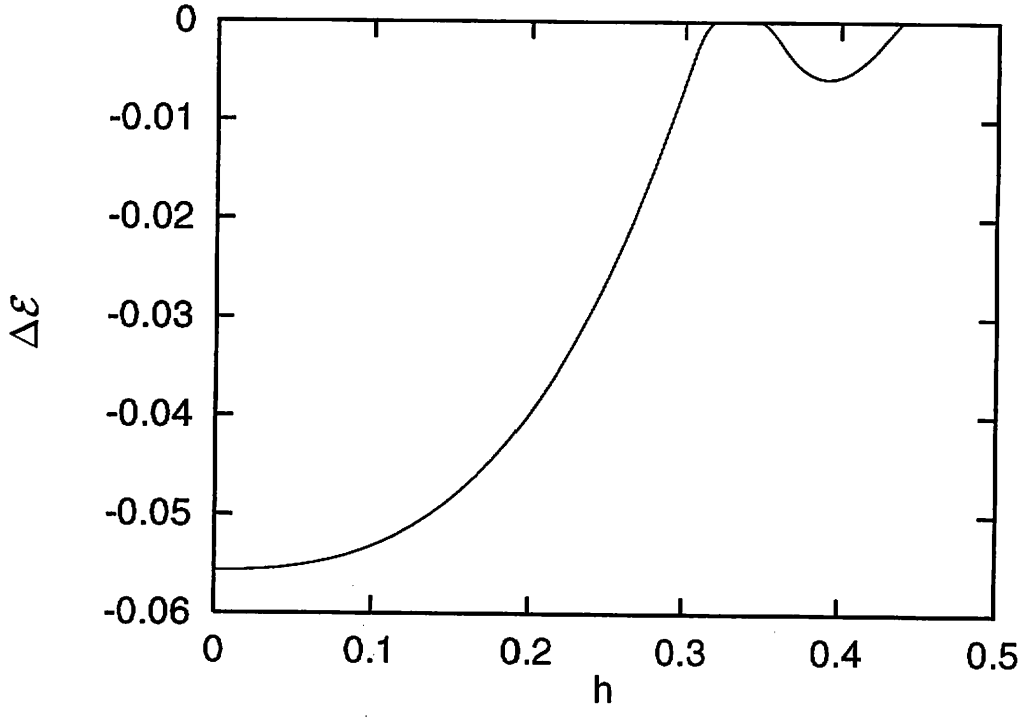

Fig. 4.9(c)

the term $\mathcal{E}_{\text{fluct}}$ strongly favors the commensurate, collinear configuration which is stable near $h = 1/3$. Corresponding to the field dependence of the energy density $\Delta\mathcal{E}$, the wavenumber q shows various behaviors as shown in Fig. 4.7.

Figure 4.10 shows the magnetization curve calculated for $J_2 = 0.13$K. A plateau-like behavior appears around $h = 1/3$. This plateau is due to the fact that, in the commensurate state, the collinear state with one third of the saturation magnetization is stable over the finite field region near $h = 1/3$. Near the transition to the commensurate state, the magnetization rapidly approaches the commensurate value M_{comm} as

$$M(h) \approx M_{\text{comm}}(h_c) - b/\ln(h_c - h), \tag{4.20}$$

where b is some constant. The logarithmic behavior of the magnetization is caused by the logarithmic behavior of the wavenumber; similar behavior is found for the case of ferromagnetic interchain interaction as shown in Appendix B. However this type of anomaly in the magnetization has not been observed experimentally [11]. We do not know whether the discrepancy is serious at this stage. Actually the experimental magnetization curve shows a discrepancy with theory even in low fields. As shown

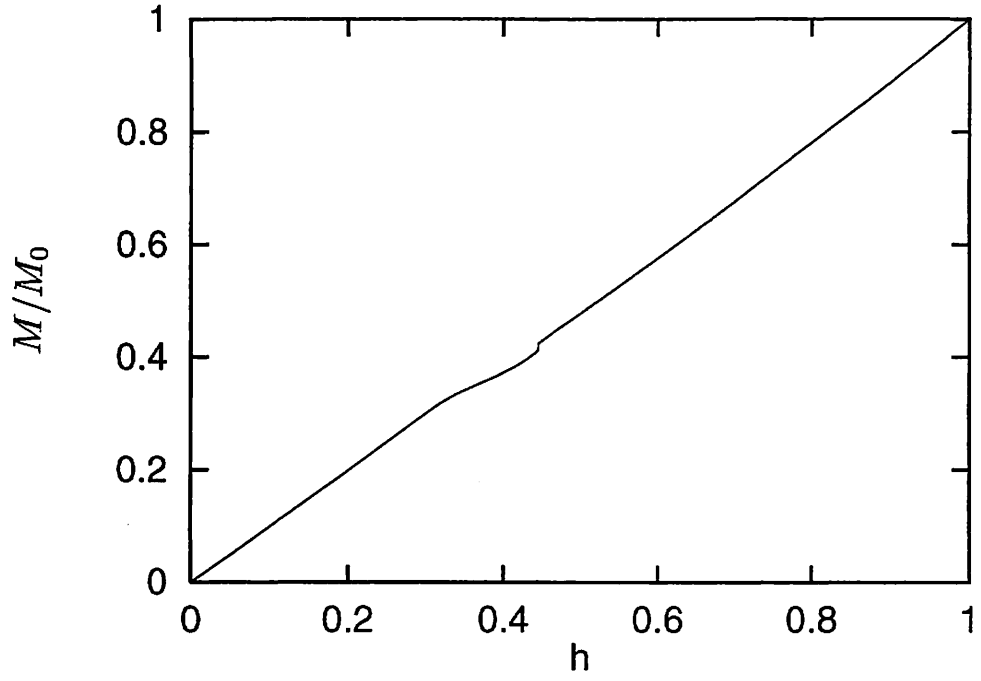

Figure 4.10: Normalized magnetization M/M_0 as a function of the reduced magnetic field $h = H/H_s$.

in Eq. (4.9), the magnetization of the incommensurate state in low fields should be lower than in the commensurate state. However the experimental result shows a relatively large initial slope of the magnetization. More careful experimental and theoretical analysis is needed on this problem.

Figure 4.11 shows the solutions of the Euler-Lagrange equation (4.16) at various fields, at the optimal wavenumber, calculated for $J_2 = 0.13$K. Figure 4.11(a) shows the solution at $h = 0.35$. Here the wavenumber q is in the plateau region. We see that one of the three spins is always oriented nearly parallel to the field, while other two spins rotate keeping an almost antiparallel configuration. Thus the magnetization is about one third of the saturation value. Figure 4.11(b) shows the phases at $h = 0.44$. A solitonic structure is developing; this is very different from the classical incommensurate state. This solitonic structure becomes more evident at higher fields near the transition to the commensurate state. Figure 4.11(c) shows the phases at a field just below the transition. This structure is very different from the classical incommensurate state shown in Fig. 4.3. There are well-defined wall regions; the order parameters between the walls are almost constant and equal to

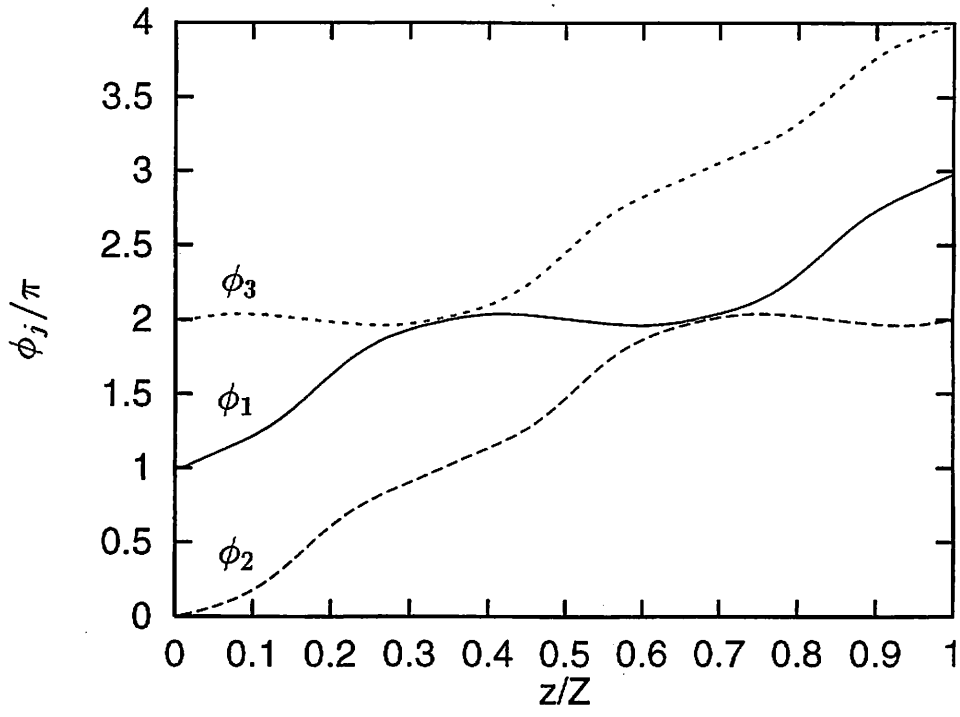

(a)

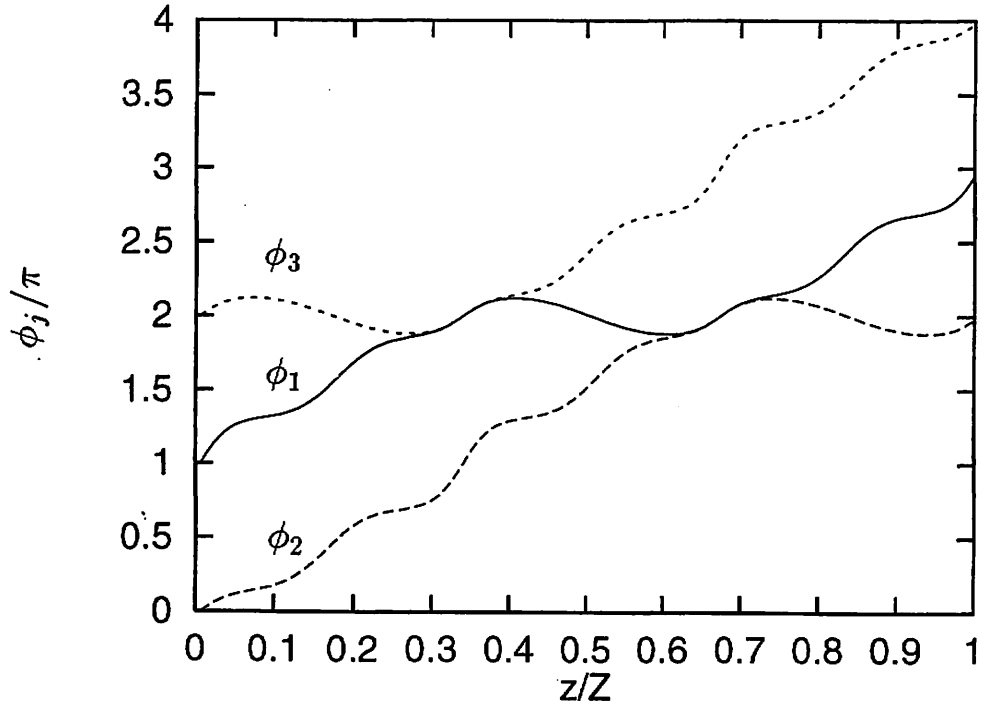

(b)

Figure 4.11: The phases ϕ_j as a function of z/Z at fields (a) $h = 0.35$, (b) 0.44, (c) ≈ 0.446(in the next page.)

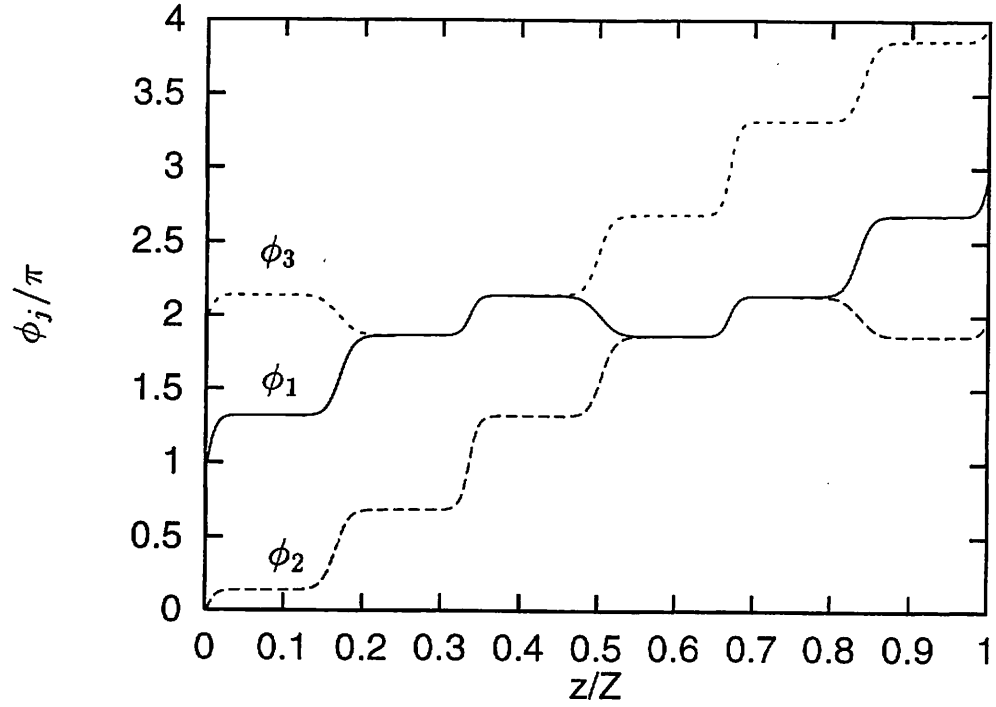

Fig. 4.11(c)

their commensurately stable values. Clearly this is due to the effect of $\mathcal{E}_{\text{fluct}}$ which breaks the continuous degeneracy in the commensurate state. Note that there are six domains within one period reflecting six-fold degeneracy in the commensurate structure. The three-fold degeneracy is associated with the interchange of the three spins, while the two-fold degeneracy is associated with the inversion $\phi_j \rightarrow -\phi_j$.

In summary, this section has applied a phenomenological theory to take into account the effect of quantum fluctuations to the incommensurate state of $CsCuCl_3$. The phenomenological term $\mathcal{E}_{\text{fluct}}$ makes remarkable modifications to the incommensurate state:

(1) The wavenumber shows a nonmonotonic dependence on the magnetic field. The behavior of the wave number is highly sensitive to the value of J_2.

(2) The wavenumber vanishes as the inverse of a logarithm at the transition to the commensurate state.

(3) At high fields, the incommensurate state has well-defined walls which separate distinct commensurate regions having nearly constant order parameters.

(4) The magnetization curve shows a plateau-like behavior around $h = 1/3$, and a rapid approach to the commensurate value near the transition to the commensurate state.

All these modifications are caused by two effects of $\mathcal{E}_{\rm fluct}$, the breaking of the nontrivial degeneracy and the favoring of the collinear state. These are nothing but the important effects of quantum fluctuations in the triangular antiferromagnet in the magnetic field.

4.4 Summary

This chapter has studied the magnetic structure of $CsCuCl_3$ in a transverse field applied perpendicular to the c-axis. First the classical theory was applied to determine the ground-state spin structure. It was shown that the transverse magnetic field deforms the helical structure and causes a transition to the commensurate state at $h = 0.473$. However the classical incommensurate state has unusual properties due to the existence of the nontrivial degeneracy. The field dependence of the wavenumber q disagrees with the neutron-scattering experiment [24,25].

We have therefore taken into account the effect of quantum fluctuations by using the phenomenological term $\mathcal{E}_{\rm fluct}$. We have seen that the incommensurate state at high fields is largely modified from the classical theory. This is because $\mathcal{E}_{\rm fluct}$ breaks the classical nontrivial degeneracy. In some sense the modified incommensurate state is similar to many other incommensurate systems. Another effect of $\mathcal{E}_{\rm fluct}$ is that it favors the collinear spin configuration. This effect induces the peculiar behavior of the field dependence of the wavenumber q. With an appropriate value for J_2, the wavenumber shows the plateau behavior which is consistent with the neutron-scattering experiment. After the plateau, the theory predicts a rapid decrease of the wave number. Therefore neutron-scattering experiments at higher fields are highly desired.

The spin-wave excitation spectrum in the incommensurate state is extremely interesting in connection with ESR experiments. Lüthi *et al.* performed ESR experiments up to 14T and found extra modes around 10T in addition to the three branches [47,48]. Ohta *et al.* also performed ESR experiments on $CsCuCl_3$ for $H \perp c$ and found similar absorptions around 10T [27,28]. But the correspondence between

their results and the results of Lüthi's group is not complete. More theoretical analysis is needed on ESR.

Chapter 5

Summary and Discussion

We have studied theoretically the effect of quantum fluctuations in hexagonal antiferromagnets in connection with the real material $CsCuCl_3$. We showed that quantum fluctuations are important for determining the ground-state spin structures in $CsCuCl_3$. $CsCuCl_3$ has antiferromagnetic c-layers with a triangular lattice; the layers are ferromagnetically coupled along the c-chain. If the system is truly isotropic, the classical ground state is nontrivially degenerate; this degeneracy should be removed by quantum fluctuations. In $CsCuCl_3$ there is a small easy-plane anisotropy and also a small DM interaction; these perturbations select a different type of ground state from that favored by quantum fluctuations. These competing effects produce intriguing behavior of $CsCuCl_3$ in magnetic fields. Various approaches were applied to investigate the role of quantum fluctuations.

In chapter 2, we presented a theoretical explanation for the small jump in the magnetization of $CsCuCl_3$, observed for $H||c$. First we applied the classical theory and showed that the easy-plane anisotropy favors the umbrella-type spin structure. Second we performed a spin-wave calculation to take into account quantum fluctuations. We showed that quantum fluctuations select the coplanar structure in the isotropic system. Comparing these two effects, we concluded that the coplanar structure is stable for $H > H_c$. The observed magnetization jump is interpreted as a quantum-fluctuation-induced spin-flop phase transition. Support for this interpretation is provided by neutron-scattering experiments. But the theory was carried out only to the lowest order in the anisotropy parameter Δ and in $1/S$. Therefore a better approach is desirable to confirm the validity of the theory, and also to solve this type of problem in the general case. From this reason we applied a complementary approach in the subsequent chapter.

In chapter 3, we concentrated on the strong-field region just below saturation. We mapped the spin-ordering problem near saturation onto the Bose-condensation problem in the low-density limit. The single-particle energy band has two minima, at $\pm\boldsymbol{Q}$, and the ground state in the low-density limit is described by a two-component Bose-condensation order parameter. The ground-state energy is expressed in terms of the order parameters, as for the Ginzburg-Landau free energy. The ground-state energy is minimized to determine the spin structure. From this study we showed that only three types of spin structures are allowed as the ground state near the saturation field; the minimum state is determined by the exchange parameters. Using reasonable parameters for $CsCuCl_3$, we showed that the coplanar structure is stable in the high-field region; this agrees with the previous result. This approach is suitable to solve problems of the $CsCuCl_3$ type, because we do not need to assume particular spin structures; instead, we can find the most stable state from the GL-theory-type argument. Moreover, this theory can give the correct qualitative result for arbitrary S, even for $S = 1/2$. However, this approach is useful only in a limited case, the high-field region near saturation. Therefore a more general treatment is needed to solve such problems in a weaker magnetic field.

In chapter 4, we studied the magnetic structure of $CsCuCl_3$ in a transverse field. First we applied the classical theory and determined the ground-state spin structure. The transverse field deforms the helical spin structure and produces a complicated incommensurate spin structure. The transition to the commensurate state was predicted to occur at a certain transition field H_c. The classical incommensurate state has unusual features which are due to the existence of the continuous nontrivial degeneracy in the commensurate state. Therefore the quantum fluctuations in the incommensurate state ware taken into account by introducing a phenomenological term which breaks the nontrivial degeneracy. The resulting incommensurate state is much modified from the classical state at high fields. In contrast to the prediction of the classical theory, the wavenumber showed a plateau in the intermediate-field region, consistent with the neutron-scattering result. From this study we showed that small quantum fluctuations can completely change the magnetic structure of $CsCuCl_3$ in a transverse field. Since the quantum effect has been included in a phenomenological manner, a refinement based the microscopic theory is desired in a future study.

It may be a little surprising that quantum fluctuations appear to be important in this quasi-one-dimensional *ferromagnet*, because it is generally believed that quantum fluctuations are very small for the ferromagnetic chain. In fact, the quantum lowering by the zero-point spin-wave fluctuations $\Delta E_{\rm SW}$ is very small in $CsCuCl_3$, as shown in Fig. 2.3. However in $CsCuCl_3$, quantum fluctuations should be compared not with the exchange coupling J_1, but rather with the small anisotropy or the DM interaction. For $H||c$, the classical ground state is determined by the easy-plane-type anisotropy Δ; this should be compared with quantum fluctuations. Since Δ is small, quantum fluctuations can dominate in determining the ground state for $H > H_c$. For $H \perp c$, the characteristic energy of the helical spin structure is $D^2/J_0 \sim 0.2J_1$, and thus quantum fluctuations can be important. Namely, the unexpected behavior of $CsCuCl_3$ in magnetic fields is likely to be a manifestation of quantum fluctuations in nearly degenerate ground states, which can be attributed to the nontrivial degeneracy in frustrated spin systems.

$RbFeCl_3$ is also a hexagonal antiferromagnet with ferromagnetic intrachain exchange so that it is another candidate to see experimentally the ground state selected by quantum fluctuations. In contrast to $CsCuCl_3$, in this material the Fe^{2+} ion has a large single-ion anisotropy of the easy-plane type. The system at low temperatures can be well described by an effective spin Hamiltonian with fictitious spin $S = 1$. In the phase diagram of $RbFeCl_3$ for a magnetic field applied perpendicular to the c-axis [49], there are two commensurate (3-sublattice) phases. By analogy with $CsCuCl_3$, we expect the effect of quantum fluctuations to appear also in $RbFeCl_3$. Since the crystal field is strong, the system is almost a singlet-ground-state system, for which the quantum effect becomes more important. The magnetic ordering in such a singlet-ground-state system with frustration is an interesting problem left for future study.

Appendix A

Excitation Spectrum in the High-Field Region

This appendix finds the spin-wave excitation spectrum in the high-field region near saturation, based on the hard-core-boson representation presented in chapter 3. The excitation energy $E_{\boldsymbol{k}}$ is determined by the pole of the one-particle Green function as

$$G(\boldsymbol{k}, E_{\boldsymbol{k}})^{-1} = 0. \tag{A.1}$$

In order to calculate the Green function, we have to introduce the following Green functions

$$G(\boldsymbol{k}, \boldsymbol{k}', \omega) = -i \int dt \mathrm{e}^{i\omega t} \langle T[a_{\boldsymbol{k}}(t) a^{\dagger}_{\boldsymbol{k}'}] \rangle, \tag{A.2}$$

where $\boldsymbol{k}' = \boldsymbol{k}, \boldsymbol{k}+\boldsymbol{Q}, \boldsymbol{k}-\boldsymbol{Q}$, and

$$F(\boldsymbol{k}, \boldsymbol{k}', \omega) = -i \int dt \mathrm{e}^{i\omega t} \langle T[a_{\boldsymbol{k}}(t) a_{\boldsymbol{k}'}] \rangle, \tag{A.3}$$

$$F^{\dagger}(\boldsymbol{k}, \boldsymbol{k}', \omega) = -i \int dt \mathrm{e}^{i\omega t} \langle T[a^{\dagger}_{\boldsymbol{k}}(t) a^{\dagger}_{\boldsymbol{k}'}] \rangle, \tag{A.4}$$

where $\boldsymbol{k}' = -\boldsymbol{k}, -\boldsymbol{k}+\boldsymbol{Q}, -\boldsymbol{k}-\boldsymbol{Q}$. The Green functions are calculated from the Dyson equations:

$$\begin{aligned} G(\boldsymbol{k}, \boldsymbol{k}', \omega) &= G^{(0)}(\boldsymbol{k}, \omega) \{ \delta_{\boldsymbol{k}, \boldsymbol{k}'} + \sum_{\boldsymbol{k}''} [\Sigma_{11}(\boldsymbol{k}, \boldsymbol{k}'', \omega) G(\boldsymbol{k}'', \boldsymbol{k}', \omega) + \Sigma_{12}(\boldsymbol{k}, \boldsymbol{k}'', \omega) F^{\dagger}(\boldsymbol{k}'', \boldsymbol{k}', \omega)] \}, \\ F^{\dagger}(\boldsymbol{k}, \boldsymbol{k}', \omega) &= G^{(0)}(\boldsymbol{k}, -\omega) \sum_{\boldsymbol{k}''} [\Sigma_{21}(\boldsymbol{k}, \boldsymbol{k}'', \omega) G(\boldsymbol{k}'', \boldsymbol{k}', \omega) + \Sigma_{11}(\boldsymbol{k}'', \boldsymbol{k}, -\omega) F^{\dagger}(\boldsymbol{k}'', \boldsymbol{k}', \omega)]. \end{aligned} \tag{A.5}$$

Figures A.1 and A.2 show the diagrams for the self energy in the low-density limit.

Although the calculation is straightforward, it is not easy to write the solution in an explicit form. We show only the results for the low-energy excitations. There

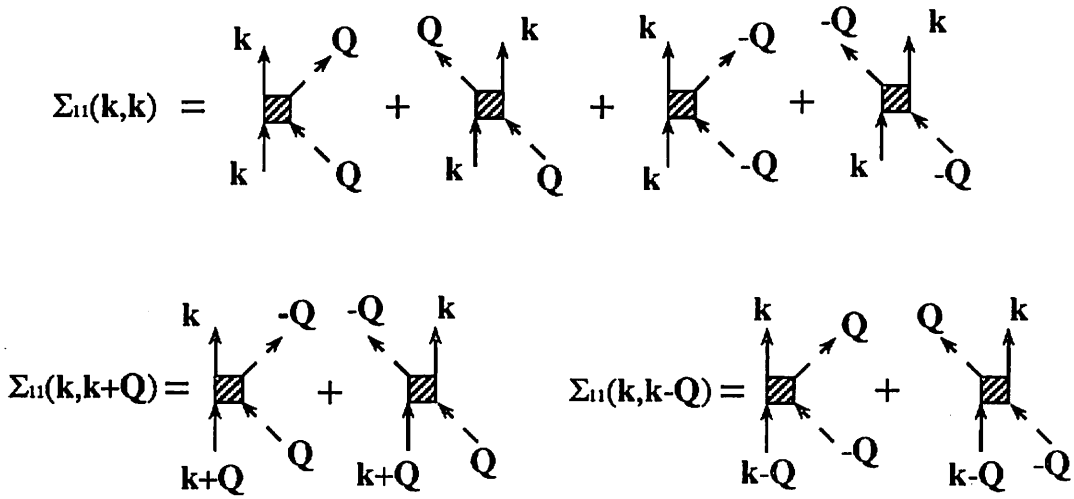

Figure A.1: Diagrams for the self energy Σ_{11}. Each vertex has internal frequency ω.

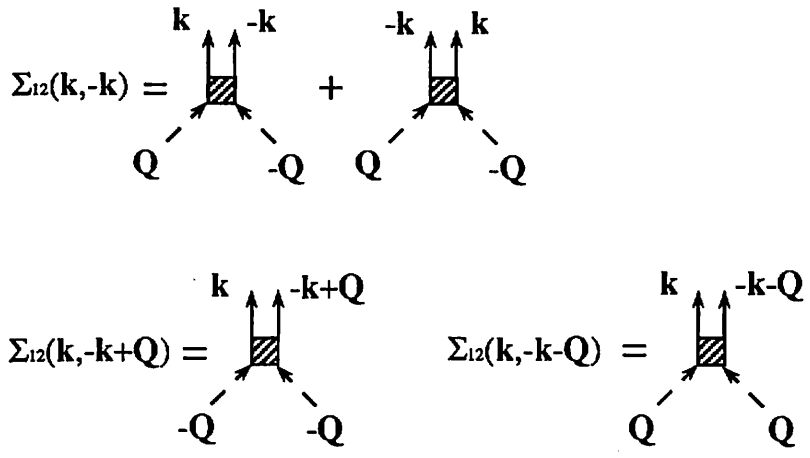

Figure A.2: Diagrams for the self energy Σ_{12}. The internal frequency for each vertex is 0.

are two low-energy branches near $\boldsymbol{k} = \pm\boldsymbol{Q}$ corresponding to the minima of the bare spectrum. One remains gapless; the expression near the minimum is same for the three spin-structure in Fig. 3.3, namely

$$E_{\boldsymbol{k}} \simeq \sqrt{(H_c - H)[2J_0^{\perp}k_z^2 + 3J_1^{\perp}(k_x^2 + k_y^2)]}. \tag{A.6}$$

The spectrum is linear at small k as is usual in antiferromagnets. The other branch has an energy gap. For the umbrella-type structure, the energy gap is given by

$$\Delta E = (H_c - H)\left(\frac{\Gamma_2}{\Gamma_1} - 1\right). \tag{A.7}$$

Note that $\Delta E < 0$ for $\Gamma_1 > \Gamma_2$, reflecting the instability of this state. The energy gap for the coplanar structures vanishes in the lowest-order approximation in $H_c - H$.

Appendix B

Incommensurate State for $J_1 < 0$

This appendix discusses the incommensurate state in the case of a ferromagnetic interchain interaction. If the interchain coupling is ferromagnetic ($J_1 < 0$), spins should be completely aligned ferromagnetically in the c-plane and thus the spin structure is expressed by only one order parameter ϕ. In this case a transition from the helical state to the completely aligned ferromagnetic state is expected to occur. The energy density measured from the commensurate state (ferromagnetic state) is

$$\Delta\mathcal{E} = \frac{1}{L}\int_0^L dz\Big[J_0 S^2\left(\frac{d\phi_j}{dz}\right)^2 - DS^2\frac{d\phi_j}{dz} + HS(1-\cos\phi)\Big], \tag{B.1}$$

where $g\mu_B$ is taken to be 1 for simplicity. The above model is equivalent to the Frank-Van der Merwe model [46] which appears in many problems of incommensurate-commensurate transitions [50]. The Euler-Lagrange equation for the phase ϕ is

$$-2J_0 S^2\frac{d^2\phi}{dz^2} + HS\sin\phi = 0. \tag{B.2}$$

This particular equation is called the sine-Gordon equation; it is the equation of motion of a pendulum under gravity, apart from some changes in notation. For zero field, Eq. (B.2) immediately gives a simple helical structure $\phi(z) = qz$ with optimal wavenumber $q_0 = D/2J_0$. For nonzero field, we obtain analytical solutions of Eq. (B.2) as follows. Multiplying Eq. (B.2) by $d\phi/dz$ and performing the integration over z, one finds

$$-J_0 S^2\left(\frac{d\phi}{dz}\right)^2 - HS\cos\phi = C, \tag{B.3}$$

where C is the constant of integration. The solutions of the Euler-Lagrange equation can be obtained by integrating Eq. (B.3).

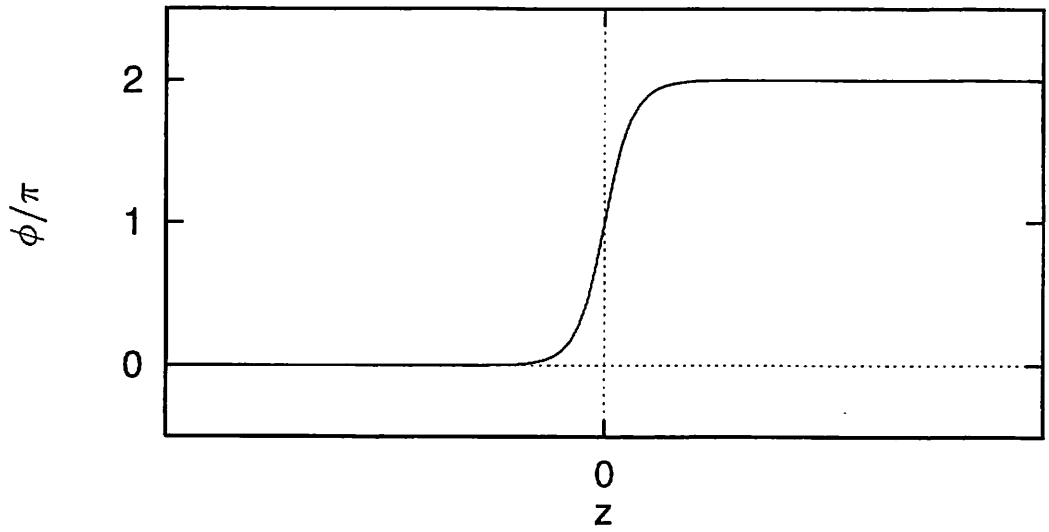

Figure B.1: Phase ϕ as a function of z for the single-soliton solution (B.5). The center of the wall is located at z=0.

(1) single-soliton solution (figure B.1)

The solution for a single soliton connects two commensurate states, one at $z = -\infty$ and other at $z = \infty$. We choose $\phi = 0$ at $z = -\infty$ and $\phi = 2\pi$ at $z = \infty$. This boundary condition gives $\mathcal{C} = -HS$. Then we obtain the following equation for ϕ:

$$\frac{d\phi}{dz} = \sqrt{\frac{2H}{J_0 S}} \sin\frac{\phi}{2}. \tag{B.4}$$

An easy integration gives

$$\phi = 4\tan^{-1}\exp[\kappa(z - z_0)], \tag{B.5}$$

where z_0 is a constant of integration and $\kappa = \sqrt{H/2J_0S}$. The wall energy E_{wall} is defined as the energy difference between the single-soliton state and the commensurate state:

$$\begin{aligned} E_{\text{wall}} &= \int_{-\infty}^{\infty} dz \left[J_0 S^2 \left(\frac{d\phi_j}{dz}\right)^2 - DS^2 \frac{d\phi_j}{dz} + g\mu_{\text{B}} HS(1 - \cos\phi) \right] \\ &= 16 J_0 S^2 \sqrt{\frac{H}{2J_0 S}} - 2\pi DS^2. \end{aligned} \tag{B.6}$$

When the wall energy is positive, the commensurate state has lower energy than the state with a single soliton. Therefore the critical field of the incommensurate-commensurate transition is defined by $E_{\text{wall}} = 0$ which leads to

$$H_{\text{c}} = \frac{\pi^2 D^2 S}{32 J_0}. \tag{B.7}$$

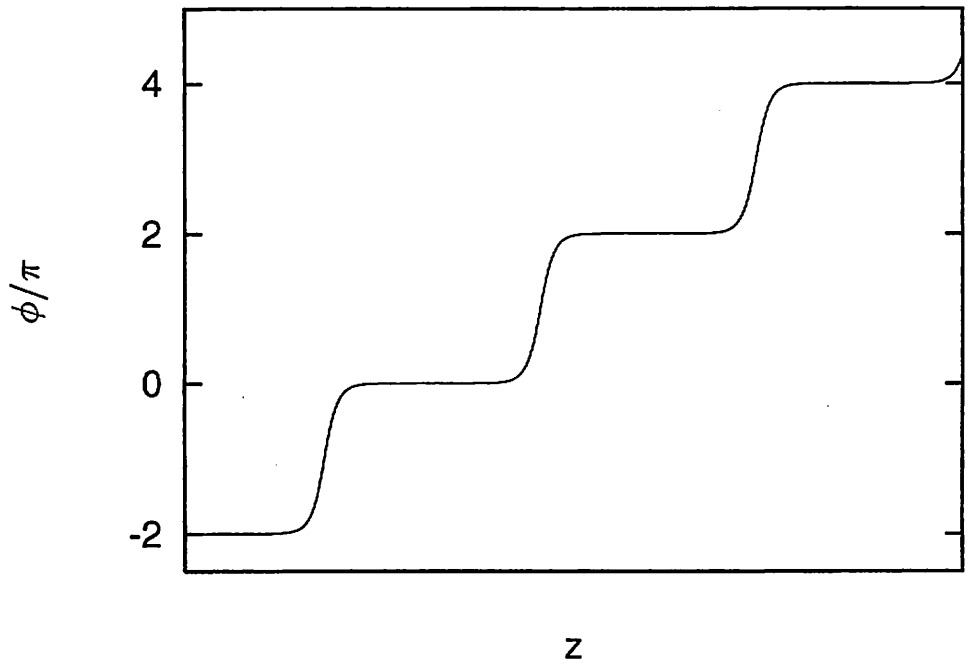

Figure B.2: Phase ϕ as a function of z for the multiple-solution solution (B.8).

For $H < H_c$, the incommensurate state with many walls (the multiple-soliton solution) is stable.

(2) multiple-soliton solution (figure B.2)

The Euler-Lagrange equation (B.2) also has solutions corresponding to a periodic array of walls. These solutions are expressed in terms of Jacobi elliptic functions:

$$\phi = \pi + 2\ \mathrm{am}\left[\frac{k}{\kappa}(z - z_0)\right], \tag{B.8}$$

where the function $\mathrm{am}(u)$ is defined by

$$u = \int_0^{\phi} \frac{d\theta}{\sqrt{1 - k^2 \sin^2\theta}},\ \phi = \mathrm{am}(u) = \mathrm{am}(u, k). \tag{B.9}$$

The period Z and the wavenumber q are connected to k by the following relation:

$$q = \frac{2\pi}{Z} = \frac{\pi\kappa}{2k\mathrm{K}(k)},\ \mathrm{K}(k) = \int_0^{\pi/2} \frac{d\theta}{\sqrt{1 - k^2 \sin^2\theta}}. \tag{B.10}$$

The energy density is expressed by the following formula

$$\Delta\mathcal{E} = -DS^2 q + 2HS\left(1 - \frac{1}{k^2}\right) + \frac{8}{Zk}\sqrt{\frac{H}{2J_0 S}}\mathrm{E}(k) 2J_0 S^2, \tag{B.11}$$

where the function $\mathrm{E}(k)$ is defined by

$$\mathrm{E}(k) = \frac{1}{2}\int_{-\pi/2}^{\pi/2} \sqrt{1 - k^2 \sin^2\theta}\, d\theta. \tag{B.12}$$

Figure B.3 shows the optimal wavenumber q as a function of the magnetic field. The incommensurate-commensurate transition $q = 0$ corresponds to $k = 1$. When k is very close to 1, the functions $\mathrm{K}(k)$ and $\mathrm{E}(k)$ behave as

$$\mathrm{K}(k) \simeq \left(\frac{1}{2} + \frac{1-k^2}{8}\right) \ln\frac{16}{1-k^2} - \frac{1-k^2}{4}, \tag{B.13}$$

$$\mathrm{E}(k) \simeq 1 - \frac{1-k^2}{4}\left(1 - \ln\frac{16}{1-k^2}\right). \tag{B.14}$$

Using the above expressions, one can write the energy density near the transition as

$$\Delta\mathcal{E} \simeq -\frac{8S}{\pi^2}(H_c - H)\left(\frac{q}{q_0}\right) + \frac{64 H_c S}{\pi^2}\left(\frac{q}{q_0}\right)\exp\left(-\frac{\pi^2 q_0}{2q}\right). \tag{B.15}$$

The first term can also be written as E_{wall}/Z; this is the single-soliton energy multiplied by the soliton density. The second term comes from the repulsive interaction between the walls. The wavenumber q varies rapidly near the transition, where it vanishes as the reciprocal of a logarithm:

$$\frac{q}{q_0} = -\frac{\pi^2}{2\ln(H_c - H)}. \tag{B.16}$$

Figure B.4 shows the magnetization (evaluated at the optimal wavenumber):

$$\frac{M}{M_0} = \frac{1}{Z}\int_0^Z \cos\phi = \frac{2}{k^2} - 1 - \frac{4}{k\kappa Z}E(k). \tag{B.17}$$

Near the transition, the magnetization logarithmically approaches the saturation value:

$$\frac{M}{M_0} = 1 + \frac{4}{\ln(H_c - H)}. \tag{B.18}$$

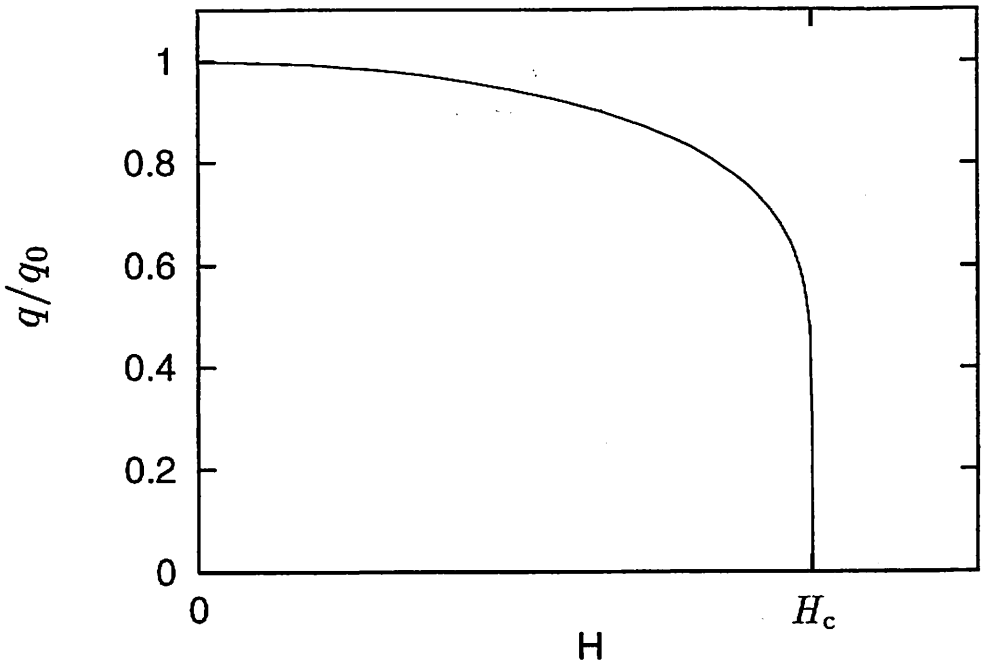

Figure B.3: Normalized optimal wavenumber q/q_0 as a function of the magnetic field H; $q_0 = D/2J_0$ is the optimal wavenumber at $H = 0$.

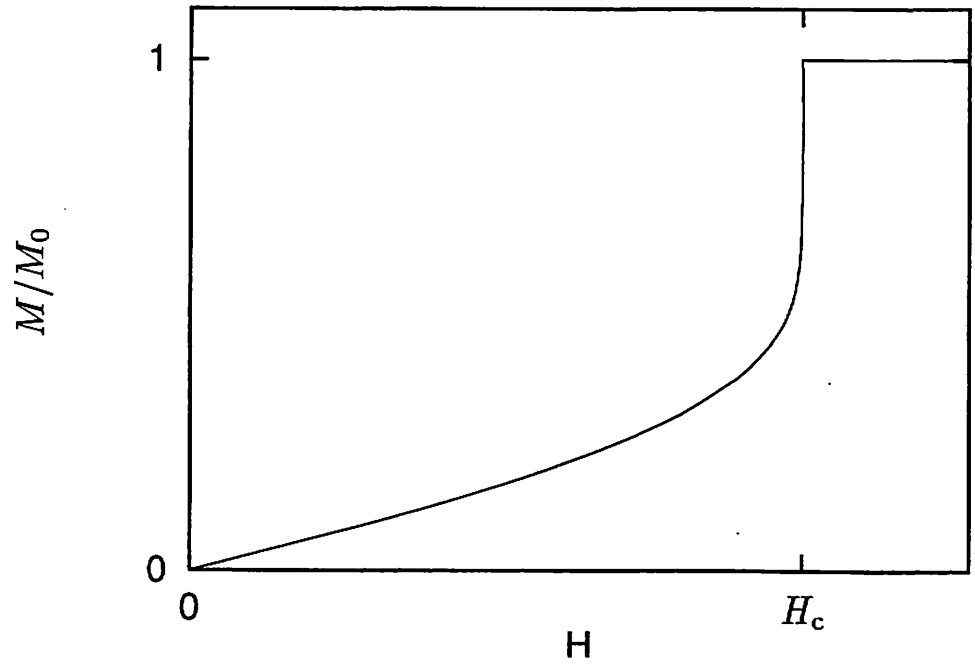

Figure B.4: Normalized magnetization M/M_0 as a function of the magnetic field H; M_0 is the saturation value of the magnetization.

Appendix C

Spin-Wave Theory of the Incommensurate State

This appendix presents the spin-wave theory of the incommensurate state. Here we treat the incommensurate state as a long-period commensurate state; the period in the c-direction is L_c. In the simplest approximation, L_c would be approximately 70 layers at $H = 0$ and about 130 layers at the plateau. (In a more accurate treatment, one could take L_c near an integer multiple of 70 for $H = 0$ and corresponding values on the plateau.) As a first step, we determine the classical values of the phases ϕ_j for specified period L_c and field H. Here we should not use the continuum approximation (4.4), but rather solve the equivalent discrete problem. Actually the solutions of the discrete problem agree with the results for the continuous case within reasonable accuracy. The spin-wave Hamiltonian is then derived by using the Holstein-Primakoff transformation, just as in section 2.2. The equivalent of equation (2.42) is

$$\begin{aligned}\mathcal{H}_{\rm SW} = E_{\rm cl} - \frac{S}{2}\sum_{\boldsymbol{k}}\sum_{jl} C_{jl} + \frac{S}{2}\sum_{\boldsymbol{k}}\sum_{jl}\sum_{j'l'}\{&\mathcal{A}_{jl,j'l'}(\boldsymbol{k})[a^\dagger_{jl}(\boldsymbol{k})a_{j'l'}(\boldsymbol{k}) + a_{jl}(-\boldsymbol{k})a^\dagger_{j'l'}(-\boldsymbol{k})] \\ &+\mathcal{B}_{jl,j'l'}[a^\dagger_{jl}(\boldsymbol{k})a^\dagger_{j'l'}(-\boldsymbol{k}) + a_{jl}(-\boldsymbol{k})a_{j'l'}(\boldsymbol{k})]\}. \qquad \text{(C.1)}\end{aligned}$$

Here $j = 1, 2, 3$ is the sublattice index and $l = 1, \cdots, L_c$ is the layer index; $E_{\rm cl}$ is the classical energy for specified period L_c and field H. The matrices $\mathcal{A}$ and $\mathcal{B}$ are defined by

$$\begin{aligned}\mathcal{A}_{jl,j'l'}(\boldsymbol{k}) = {}& C_{jl}\delta_{j'j}\delta_{l'l} + B_{j,l+1,l}e^{ik_z}\delta_{j'j}\delta_{l'l+1} + B_{j,l,l-1}e^{-ik_z}\delta_{j'j}\delta_{l'l-1} \\ &+E_{j+1,j,l}\nu_{\boldsymbol{k}}\delta_{j'j+1}\delta_{l'l} + E_{j-1,j,l}\nu_{-\boldsymbol{k}}\delta_{j'j-1}\delta_{l'l}, \qquad \text{(C.2)}\end{aligned}$$

$$\begin{aligned}\mathcal{B}_{jl,j'l'}(\boldsymbol{k}) = {}& A_{j,l+1,l}e^{ik_z}\delta_{j'j}\delta_{l'l+1} + A_{j,l,l-1}e^{-ik_z}\delta_{j'j}\delta_{l'l-1} \\ &+D_{j+1,j,l}\nu_{\boldsymbol{k}}\delta_{j'j+1}\delta_{l'l} + D_{j-1,j,l}\nu_{-\boldsymbol{k}}\delta_{j'j-1}\delta_{l'l}, \qquad \text{(C.3)}\end{aligned}$$

where the definitions of the constants A, B, C, D and E are

$$A_{j,l+1,l} = -J_0[\cos(\phi_{jl+1} - \phi_{jl}) - 1] - \frac{1}{2}D\sin(\phi_{jl+1} - \phi_{jl})], \tag{C.4}$$

$$B_{j,l+1,l} = -J_0[\cos(\phi_{jl+1} - \phi_{jl}) + 1] - \frac{1}{2}D\sin(\phi_{jl+1} - \phi_{jl})], \tag{C.5}$$

$$\begin{aligned} C_{jl} = {} & 2J_0[\cos(\phi_{jl+1} - \phi_{jl}) + \cos(\phi_{jl} - \phi_{jl-1})] \\ & + D[\sin(\phi_{jl+1} - \phi_{jl}) + \sin(\phi_{jl} - \phi_{jl-1})] \\ & + 18J_1 h\cos\phi_{jl} - 6J_1[\cos(\phi_{j+1l} - \phi_{jl}) + \cos(\phi_{j-1l} - \phi_{jl})], \end{aligned} \tag{C.6}$$

$$D_{j+s,j,l} = 3J_1[\cos(\phi_{j+sl} - \phi_{jl}) - 1], \tag{C.7}$$

$$E_{j+s,j,l} = 3J_1[\cos(\phi_{j+sl} - \phi_{jl}) + 1]. \tag{C.8}$$

The next step is to find the spin-wave Hamiltonian $\mathcal{H}_{\rm SW}$ in diagonal form:

$$\mathcal{H}_{\rm SW} = E_{\rm cl} - \frac{S}{2}\sum_{\boldsymbol{k}}\sum_{jl} C_{jl} + \frac{S}{2}\sum_{\boldsymbol{k}}\sum_{jl}\omega_{jl}(\boldsymbol{k})[\alpha^\dagger_{jl}(\boldsymbol{k})\alpha_{jl}(\boldsymbol{k}) + \alpha_{jl}(-\boldsymbol{k})\alpha^\dagger_{jl}(-\boldsymbol{k})], \tag{C.9}$$

where $a_{jl}(\boldsymbol{k})$ and $\alpha_{jl}(\boldsymbol{k})$ are related though the following Bogoliubov transformation:

$$\begin{cases} a_{jl}(\boldsymbol{k}) = \sum_{j'l'}[u^{(j'l')}_{jl}(\boldsymbol{k})\alpha_{j'l'}(\boldsymbol{k}) + v^{(j'l')}_{jl}(\boldsymbol{k})\alpha^\dagger_{j'l'}(-\boldsymbol{k})], \\ a^\dagger_{jl}(-\boldsymbol{k}) = \sum_{j'l'}[u^{(j'l')}_{jl}(\boldsymbol{k})\alpha^\dagger_{j'l'}(-\boldsymbol{k}) + v^{(j'l')}_{jl}(\boldsymbol{k})\alpha_{j'l'}(-\boldsymbol{k})]. \end{cases} \tag{C.10}$$

The Bogoliubov equations for u and v are

$$\begin{cases} (\mathcal{A} + \mathcal{B})(u^{(jl)} + v^{(jl)}) = \omega_{jl}(u^{(jl)} - v^{(jl)}), \\ (\mathcal{A} - \mathcal{B})(u^{(jl)} - v^{(jl)}) = \omega_{jl}(u^{(jl)} + v^{(jl)}), \end{cases} \tag{C.11}$$

where $\boldsymbol{u}$ and $\boldsymbol{v}$ are $3L_c$-component vectors defined by an equation similar to Eq. (2.49). The spin-wave energy $\omega_{jl}(\boldsymbol{k})$ is given by the solution of

$$\det[(\mathcal{A} - \mathcal{B})(\mathcal{A} + \mathcal{B}) - \omega^2] = 0. \tag{C.12}$$

Then we find the energy to order $1/S$ as

$$E = E_{\rm cl} - \frac{S}{2}\sum_{\boldsymbol{k}}\sum_{jl} C_{jl} + \frac{S}{2}\sum_{\boldsymbol{k}}\sum_{jl}\omega_{jl}(\boldsymbol{k}). \tag{C.13}$$

We minimize the energy with respect to the period, and find the optimal wavenumber $q = 2\pi/L_c$.

Figure C.1 shows the energy of the incommensurate state to order $1/S$ (evaluated at the optimal wavenumber q shown in Fig. C.2), which is measured from the classical energy of the commensurate state. The broken lines show the energy of the commensurate states in Fig. 2.1(b), (c) and (d). We find that the energy of the incommensurate state becomes higher than that of the commensurate state for $h > 0.3$. As shown in Fig. C.2, the optimal wavenumber q is still finite at $h = 0.3$, and only slightly below the classical value. However, we cannot conclude that a first-order transition to the commensurate state occurs at $h \approx 0.3$. As we have shown in section 4.2, the classical incommensurate state has no regions where the order parameters are nearly constant. Therefore the classical incommensurate state in the infinite L_c limit does not approach to a specific commensurate state. (Actually we cannot specify the commensurate state because of the nontrivial degeneracy.) Consequently the energy of the incommensurate state to order $1/S$ does not approach that of the lowest commensurate state in the limit $L_c \to \infty$. For this reason the transition to the commensurate state cannot be discussed by the spin-wave theory. The crossing of the energy in Fig. C.1 signifies that the spin-wave theory does not work well in the theory of the incommensurate state.

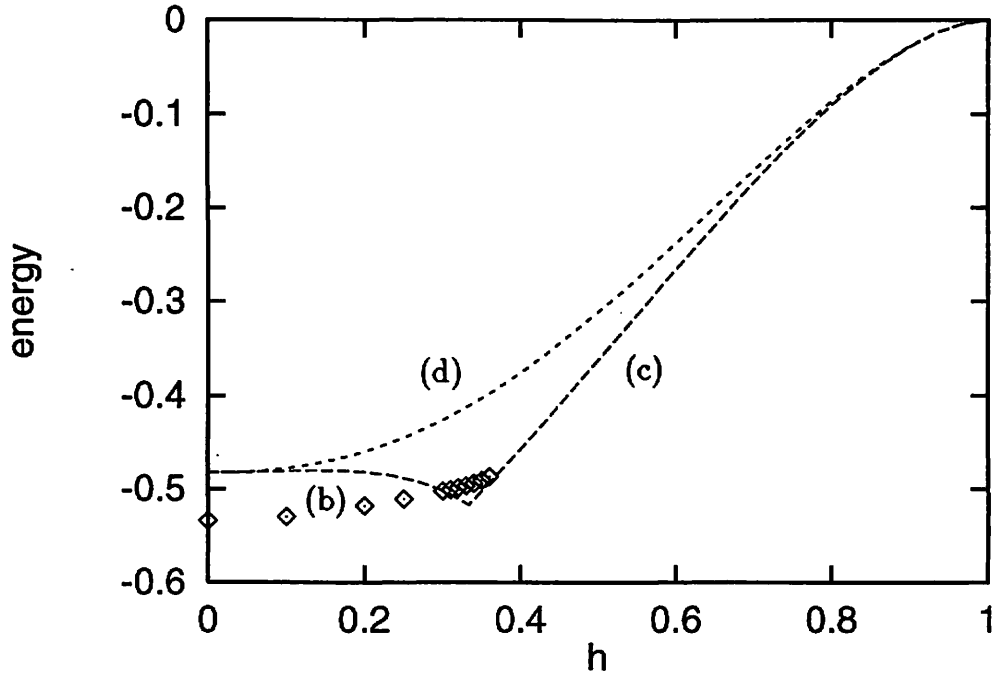

Figure C.1: The energy of the incommensurate state to order $1/S$ optimized with respect to the wavenumber q (open diamond). The energy is measured from that of the classical commensurate state at the same field. The broken lines are the energies calculated for the commensurate states in Fig. 2.1(b),(c) and (d).

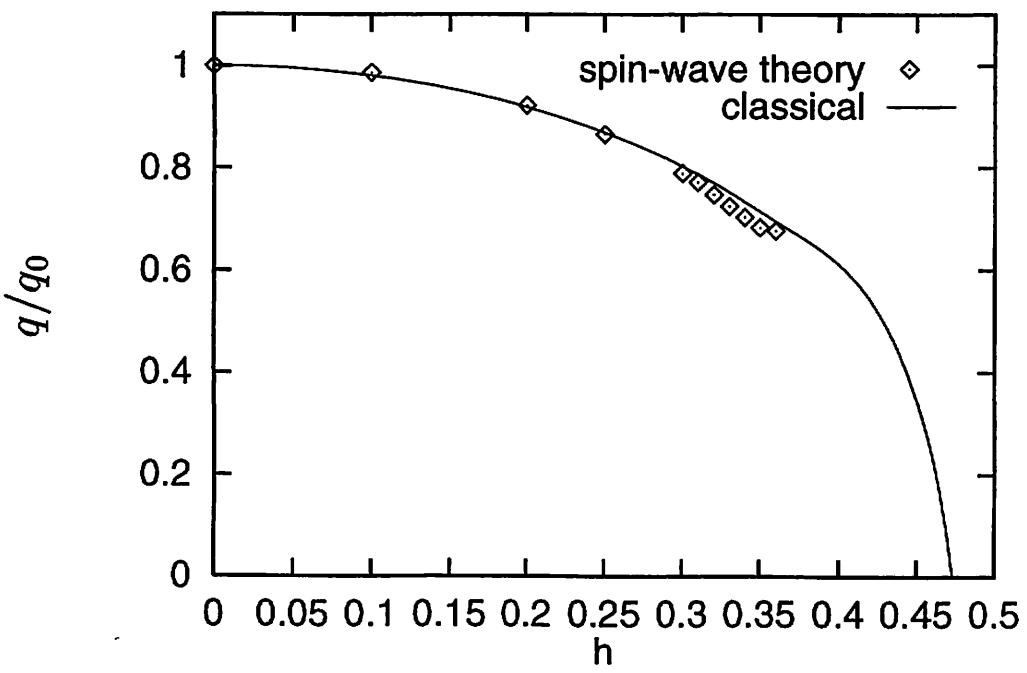

Figure C.2: Normalized optimal wavenumber q as a function of the reduced magnetic field $h = H/H_s$ (open diamond). The solid line shows the classical result (same as Fig. 4.1).

References

[1] H. Kawamura: J.Phys.Soc.Jpn. **53** (1984) 2452.

[2] H. Kawamura and S. Miyashita: J. Phys. Soc. Jpn. **54** (1985) 4530.

[3] A. V. Chubukov and D. I. Golosov: J. Phys. C**3** (1991) 69.

[4] T. Oguchi, H. Nishimori and Y. Taguchi: J. Phys. Soc. Jpn. **54** (1985) 4492.

[5] C. L. Henley: Phys. Rev. Lett. **62** (1989) 2056.

[6] K. Kubo and T. Kishi: J. Phys. Soc. Jpn. **60** (1991) 567.

[7] S. Miyashita and H. Kawamura: J. Phys. Soc. Jpn. **54** (1985) 3385.

[8] B. Kleine , E. Müller-Hartmann, K. Frahm, and P. Fazekas: Z. Phys. B**87** (1992) 103.

[9] Q. Sheng and C. L. Henley: J. Phys. C**4** (1992) 2937.

[10] M. Motokawa: abstract of the talk at the Annual Meeting of the Physical Society of Japan (1978) and private communication.

[11] H. Nojiri, Y. Tokunaga and M. Motokawa: *Proc. Int. Conf. Magnetism, Paris*, 1988, J. Phys. (Paris) **49** (1988) Suppl. C8 p.1459.

[12] E. Rastelli and A. Tassi: Z. Phys. B**94**, (1994) 139.

[13] H. Nishimori and S. Miyashita: J. Phys. Soc. Jpn. **55** (1986) 4448.

[14] E. Rastelli, A. Tassi, A. Pimpinelli and S. Sedazzari: Phys. Rev. B **45** (1992) 7936.

[15] E. Rastelli, A. Tassi: Phys. Rev. B **49** (1994) 9679.

[16] S. Hirotsu: J. Phys. C10 (1977) 967.

[17] Y. Tazuke, H. Tanaka, K. Iio and K. Nagata: J. Phys. Soc. Jpn. **50** (1981) 3919.

[18] H. Hyodo, K. Iio and K. Nagata: J. Phys. Soc. Jpn. **50** (1981) 1545.

[19] K. Adachi, N. Achiwa and M. Mekata: J. Phys. Soc. Jpn. **49** (1980) 545.

[20] N. V. Fedoseeva, R. S. Gekht, T. A. Velikanova and A. D. Balaev: JETP Lett. **41** (1985) 408.

[21] T. Nikuni and H. Shiba: J. Phys. Soc. Jpn. **62** (1993) 3268.; H. Shiba and T. Nikuni: *Recent Advances in Magnetism of Transition Metal Compounds*, ed. A. Kotani and N. Suzuki (World Scientific, Singapore, 1993) p.372.

[22] H. Tanaka, U. Schotte and K. Schotte: J. Phys. Soc. Jpn. **61** (1992) 1344.

[23] W. Palme, F. Mertens, O. Born, B. Lüthi and U. Schotte: Solid State Commun. **76** (1990) 873.

[24] M. Mino, K. Ubukata, T. Bokui, M. Arai, H. Tanaka and M. Motokawa: Physica B **201** (1994) 213.

[25] M. Motokawa, M. Arai, H. Ohta, M. Mino H. Tanaka and K. Ubukata: Physica B **211** (1995) 199.

[26] U. Schotte, N. Stüsser, K. D. Schotte, H, Weinfureter, H. M. Mayer and M. Winkelmann: J. Phys.:Condens. Matter **6** (1994) 10105.

[27] H. Ohta, S. Imagawa, M. Motokawa and H. Tanaka: J. Phys. Soc. Jpn. **62** (1993) 3011.

[28] H. Ohta, S. Imagawa, M. Motokawa and H. Tanaka: Physica B **201** (1994) 208.

[29] M. Chiba, K. Ohara, Y. Ajiro and T. Morimoto: J. Phys. Soc. Jpn. **62** (1993) 4186.

[30] M. Chiba, Y. Ajiro and T. Morimoto: Physica B **201** (1994) 200.

[31] R. S. Gekht, N. V. Fedoseeva, V. A. Dolina and A. D. Balaev: Phys. stat. sol. (b) **155** (1989) 639.

[32] H. Shiba and N. Suzuki: J. Phys. Soc. Jpn. **51** (1982) 3488.

[33] T. Nikuni and H. Shiba: J. Phys. Soc. Jpn. **64** (1995) 3471.

[34] T. Matsubara and H. Matsuda: Prog. Theor. Phys. **16** (1956) 569.

[35] V. Kalmeyer and R. B. Laughlin: Phys. Rev. Lett. **59** (1987) 2095.

[36] E. G. Batuev and L. S. Braginski: Zh. Eksp. Teor. Fiz. **87** (1984) 1361 [Sov. Phys. JETP **60** (1984) 781].

[37] S. Gluzman: Phys. Rev. B **49** (1994) 11962.

[38] S. Gluzman: Phys. Rev. B **50** (1994) 6264.

[39] S. T. Beliaev: Zh. Eksp. Theor. Fiz. **34** (1958) 417; **34** (1958) 433 [Sov.Phys.–JETP **34** (1958) 289; **34** (1958) 299].

[40] N. M. Hugenholtz and D. Pines: Phys. Rev. **116** (1959) 489.

[41] A. L. Fetter and J. D. Walecka: *Quantum Theory of Many Particle Systems* (McGraw-Hill, New York, 1971) Chap. 6.

[42] A. E. Jacobs, T. Nikuni and H. Shiba: J. Phys. Soc. Jpn. **62** (1993) 4066.

[43] T. Ohyama and A. E. Jacobs: Phys. Rev. B **52** (1995) 4389.

[44] T. Nagamiya, K. Nagata and Y. Kitano: Prog. Theor. Phys. **27** (1962) 1253.

[45] T. Moriya and T. Miyadai: Solid State Commun. **42** (1982) 209.

[46] F. C. Frank and J. H. van der Merwe: Proc. Roy. Soc. (London). **198** (1949) 205, 216. The discrete version of the model is due to Y. I. Frenkel and T. Kontorowa: Zh. Exsp. Teor. Fiz. **8** (1938) 1340.

[47] W. Palme, H. Kriegelstein, G. Gojkovic and B. Lüthi: Int. J. Mod. Phys. B **7** (1993) 1013.

[48] G. Gojkovic: Diplomarbeit (Universität Frankfurt, 1993).

[49] N. Wada, K. Sumiyoshi, T. Watanabe and K. Amaya: J. Phys. Soc. Jpn. **52** (1983) 1893.

[50] P. Bak: Rep. Prog. Phys. 45 (1982) 587.